# ONE-EQUATION LES MODELING OF ROTATING TURBULENCE

by

Hao Lu

A dissertation submitted in partial fulfillment of

the requirements for the degree of

Doctor of Philosophy

(Mechanical Engineering)

at the

UNIVERSITY OF WISCONSIN - MADISON

2007

# ONE-EQUATION LES MODELING OF ROTATING TURBULENCE

Hao Lu

Under the Supervision of Professor Christopher J. Rutland

and Professor Leslie M. Smith

at the University of Wisconsin - Madison

Rotating turbulence provides a simple configuration to study characteristic features and turbulent model performance in anisotropic turbulence. It has been observed in experiments and Direct Numerical Simulation (DNS) that rotating turbulence has many distinctive qualities, such as reduced kinetic energy dissipation, reverse kinetic energy transfer from small scales to large scales, quasi 2D flow at large scales, and cyclone/anti-cyclone asymmetry. A successful subgrid scale (SGS) model should be able to capture these features, and the challenge is to simultaneously reflect the anisotropic 3D nature of small scales and the primarily 2D nature of larger scales. *A-priori* tests and *a-posteriori* tests were carried out to examine model performance.

*A-priori* tests of models were performed using DNS results for forced isotropic and rotating turbulence. A range of models were tested varying from algebraic, gradient, and scale similarity, to one-equation viscosity and non-viscosity dynamic structure models. Anisotropy and Material Frame Indifference (MFI) requirements for models in rotating systems were reviewed and used to help construct new models based on the dynamic structure approach. The models were evaluated primarily using correlation and regression coefficients of individual components of the SGS tensor, components of the divergence of the SGS stresses, and the SGS energy production

term. For all measures examined, the MFI-consistent dynamic structure models perform significantly better, especially for rotating turbulence.

At the *a-posteriori* test level, we evaluated models using two flow configurations: (i) homogeneous decaying turbulence; and (ii) rotating turbulence forced at large or intermediate scales. Testing was done for the first configuration through a systematic comparison between DNS results and large eddy simulation results at lower resolutions. The results were then analyzed in terms of several representative characteristics, including resolved kinetic energy, SGS energy production, molecular dissipation, and kinetic energy spectrum. The new models showed more accurate results than traditional models for almost all of these characteristics. The second configuration concerns the characteristic features of rotating turbulence. Again, compared to traditional models, the new models were better able to capture essential features of rotating turbulence.

# ACKNOWLEDGMENTS

I would like to express my sincere gratitude to my advisors, Professor Christopher J. Rutland and Professor Leslie M. Smith, for their guidance, technical assistance, encouragement and freedom provided to me during the past five years.

Thank Dr. Yun-Liang Wang for useful discussions, Joshua Leach for providing computing resources and great assistance at the Engine Research Center, and Yvonne Nagel for providing computing resources at the Department of Mathematics.

On a personal note, I would like to thank my parents, for their love and support.

This work was supported by the U.S. Army Research Office (ARO), the National Science Foundation (NSF), and the NSF Scientific Computing Research Environments in the Mathematical Sciences (SCREMS).

DISCARD THIS PAGE

# TABLE OF CONTENTS

DISCARD THIS PAGE

# LIST OF TABLES

**Table**

DISCARD THIS PAGE

# LIST OF FIGURES

**Figure**

DISCARD THIS PAGE

# NOMENCLATURE

## Acronyms

| | | |
|---|---|---|
| **CFD** | : | Computational Fluid Dynamics |
| **CFL** | : | Courant-Friedrichs-Lewy |
| **DNS** | : | Direct Numerical Simulation |
| **DSM** | : | Dynamic Structure Model |
| **DynSM** | : | Dynamic Smagorinsky Model |
| **EDQNM** | : | Eddy Damped Quasi-Normal Markovian |
| **GCDSM** | : | Gradient type Consistent DSM |
| **KEM** | : | subgrid Kinetic Energy Model |
| **LES** | : | Large Eddy Simulation |
| **MFI** | : | Material Frame Indifference |
| **MixGCDSM** | : | Mixed Gradient type Consistent DSM |
| **MixGM** | : | Mixed Gradient Model |
| **MixSCDSM** | : | Mixed Similarity type Consistent DSM |
| **MixSSM** | : | Mixed Scale Similarity Model |
| **ODE** | : | Ordinary Differential Equation |
| **PDE** | : | Partial Differential Equation |
| **PDF** | : | Probability Density Function |
| **PIV** | : | Particle Image Velocimetry |
| **RANS** | : | Reynolds-Averaged Navier-Stokes |
| **RMS** | : | Root-Mean-Square |
| **SCDSM** | : | Similarity type Consistent DSM |
| **SGS** | : | Sub-Grid Scale |
| **SM** | : | Smagorinsky Model |
| **SSM** | : | Scale Similarity Model |

| | | |
|---|---|---|
| **TNS** | : | Truncated Navier-Stokes |

## Auxiliary Symbols ($f$ represents a generic variable)

| | | |
|---|---|---|
| $\overline{f}$ | : | LES base filtering operation |
| $\widetilde{f}$ | : | LES test filtering operation |
| $f'$ | : | LES fluctuating component |
| $\widehat{f}$ | : | $f$ in Fourier space |
| $< f >$ | : | arithmetic mean of $f$ |

## Greek Symbols

| | | |
|---|---|---|
| $\beta$ | : | regression coefficient |
| $\delta_{ij}$ | : | Kronecker delta |
| $\Delta$ | : | filter length at "grid" level |
| $\widetilde{\Delta}$ | : | filter length at "test" level |
| $\epsilon_{ijk}$ | : | Levi-Civita symbol |
| $\varepsilon$ | : | kinetic energy dissipation rate |
| $\eta$ | : | Kolmogorov length scale |
| $\lambda$ | : | Taylor micro-scale |
| $\nu$ | : | kinematic viscosity |
| $\nu_t$ | : | eddy viscosity |
| $\nu_k$ | : | SGS eddy viscosity |
| $\rho$ | : | correlation coefficient |
| $\tau_{ij}$ | : | SGS stress tensor |
| $\tau_{ij}^{model}$ | : | modeled SGS stress tensor |
| $\omega$ | : | vorticity |
| $\Omega$ | : | rotation rate |

## Roman Symbols

| | | |
|---|---|---|
| $C_D$ | : | dynamic coefficient |
| $C_k$ | : | dynamic coefficient for the KEM |

| | | |
|---|---|---|
| $C_L$ | : | similarity coefficient |
| $C_{ij}^M$ | : | modified cross term |
| $C_s$ | : | Smagorinsky coefficient |
| $G_{ij}$ | : | gradient term |
| $k_c$ | : | cutoff wavenumber |
| $k_f$ | : | forced wavenumber |
| $k_{sgs}$ | : | SGS kinetic energy |
| $L_{ij}^M$ | : | modified Leonard term |
| $Re$ | : | Reynolds number |
| $R_{ij}^M$ | : | modified SGS Reynolds stress term |
| $Ro$ | : | Rossby number |
| $p$ | : | pressure |
| $P$ | : | SGS energy production |
| $P_{ij}$ | : | classical solenoidal projector |
| $S_{ij}$ | : | strain tensor |

# Chapter 1

# Introduction

## 1.1 Background

> According to an apocryphal story, Werner Karl Heisenberg (1901-1976) was asked what he would ask God, given the opportunity. His reply was, "When I meet God, I am going to ask Him two questions: Why relativity? And why turbulence? I really believe He will have an answer for the first."

Turbulence occurs frequently in nature. It is a state of fluid motion that is characterized by apparently random and chaotic three-dimensional vorticity. It usually dominates all other flow phenomena and results in increased kinetic energy dissipation, mixing, heat transfer, and drag. Leonardo da Vinci (1452-1519) probably is the first know person to attempt a scientific study of turbulence. Around 1510, he drew a series pictures of vortices (Fig. 1.1) and left his observation (in Piomelli's translation, [89]): "Observe the motion of the water surface, which resembles that of hair, that has two motions: one due to the weight of the shaft, the other to the shape of the curls; thus, water has eddying motions, one part of which is due to the principal current, the other to the random and reverse motion ... The small eddies are almost numberless, and large things are rotated only by large eddies and not by

small ones, and small things are turned by both small eddies and large ...” These notes were not accompanied by a mathematical analysis, but the observation might be seen as a precursor to Reynolds averaging of velocity.

Figure 1.1: Sketches from Leonardo da Vinci's notebooks.

Leonardo was followed in the late seventeenth century by Sir Isaac Newton (1643-1727). His contributions to fluid mechanics include four important findings: his second law, $\vec{F} = m \cdot \vec{a}$; the concept of Newtonian viscosity in which stress and strain rate vary linearly; the reciprocity principle, which states that the force applied on a stationary object by a moving fluid is equal to the change in momentum of the fluid as it deflects around the front of the object; and the relationship between the speed of waves at a liquid surface and their wavelength. In the eighteenth and nineteenth centuries, more significant work was done to mathematically describe the motion of fluids. Daniel Bernoulli (1700-1782) derived the famous Bernoulli equation, and Leonhard Euler (1707-1783) proposed the Euler equations, which describe both the conservation of momentum for an inviscid fluid and the conservation of

mass. Euler also proposed the velocity potential theory. Two other very important contributors to the field of fluid flow emerged at this time. Claude-Louis Navier (1785-1836) and Sir George Gabriel Stokes (1819-1903), both of whom introduced viscous transport into the Euler equations. These efforts resulted in the now famous Navier-Stokes equations. The differential mathematical equations that these two researchers proposed nearly 200 years ago are the basis of the modern Computational Fluid Dynamics (CFD) industry. They include expressions for the conservation of mass and momentum.

The anecdote cited at the beginning of this chapter is probably untrue, while it bears an uncanny resemblance to a comment in 1932 by the British physicist Sir Horace Lamb (1849-1934), who, in an address to the British Association for the Advancement of Science. He reportedly said, "I am an old man now, and when I die and go to heaven there are two matters on which I hope for enlightenment. One is quantum electrodynamics, and the other is the turbulent motion of fluids. And about the former I am rather optimistic."

Why then is the problem of turbulence so difficult? One reason is that these nonlinear partial differential equations, the Navier-Stokes equations, appear to be insoluble. There are only partial proofs for the existence, uniqueness and regularity of solutions. What is more, these proofs correspond to simplified cases. It is not clear whether the equations themselves have some hidden randomness, or just the solutions. And if the latter, is it a consequence of the equations, or a consequence of the initial conditions?

With increased computing power over the last three decades, researchers can numerically solve the Navier-Stokes equations to obtain a complete description of a

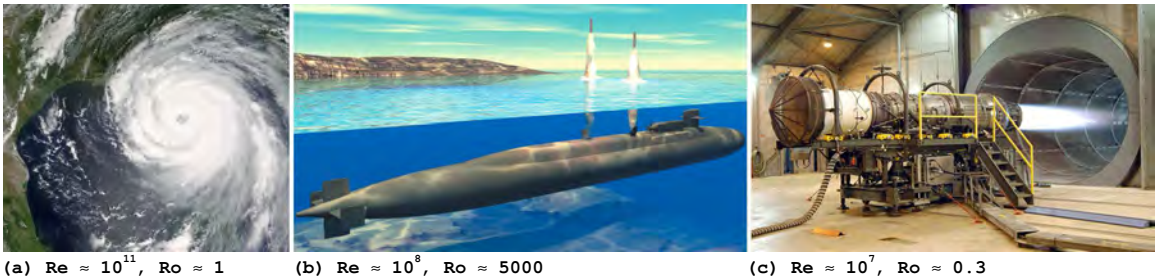

(a) Re ≈ $10^{11}$, Ro ≈ 1 (b) Re ≈ $10^{8}$, Ro ≈ 5000 (c) Re ≈ $10^{7}$, Ro ≈ 0.3

Figure 1.2: Some examples of Reynolds numbers and Rossby numbers: (a) Hurricane Katrina on August 28, 2005; (b) artist's conception of an Ohio class submarine launching Tomahawk cruise missiles; (c) test of a Pratt & Whitney F100 turbofan engine.

turbulent flow, where the flow variable (e.g., velocity, pressure, and so on) is expressed as a function of space and time. The Direct Numerical Simulation (DNS) of turbulence is the most straightforward approach to the solution of turbulent flows (Moin & Mahesh [73]).

However, we will not be able to perform DNS for real engineering problems until a few hundred generations of computers have come and gone (Gad-el-Hak [34]). There are two requirements that a DNS must meet if it is to represent a turbulent flow. First, all scales of motion need to be captured, in the deterministic sense, by the size of the grid, which must be no larger than the smallest length scale, called the Kolmogorov scale, $\eta$. In particular, the Reynolds number, $Re$, should be small enough to allow the mesh to capture the viscous dissipation scales. Second, all the significant fluid motions allowed by the Navier-Stokes equations have to be captured. The domain of the calculation must be at least as large as either the physical domain or the largest turbulent eddy. A useful measure of this scale is the integral scale ($L$)

of the turbulence which is the distance over which the fluctuating velocity remains correlated. At lease one integral scale is needed in the calculation domain, typically three integral scales are needed. DNS has faced essential difficulties. Highly accurate, high-order schemes (spectral methods, for example) tend to have little flexibility in the handling of complex geometries and of general boundary conditions. Also, to resolve all scales of motion requires that the number of grid points be proportional to the 9/4 power of $Re$, as a result, the cost of computation scales increases as does $Re^3$. For these reasons, DNS has been limited to simple geometries and to low Reynolds number cases. Until now, the highest computer power has allowed for solutions of turbulent flow up to $Re \sim 10^4$ (based on integral scale) with a grid resolution of $\sim 4096^3$ (Kaneda & Ishihara [52]). Many physical phenomena (Fig. 1.2), however, have much higher Reynolds numbers: for instance, the Reynolds number of a typical internal combustion engine is $\sim 10^6$, the Reynolds number of a typical gas turbine engine flow is $\sim 10^7$, the Reynolds number of a typical ocean liner is $\sim 10^8$, and the Reynolds number of a typical hurricane is $\sim 10^{11}$. Turbulence modeling techniques are obviously needed to solve many practical problems.

Based on the Reynolds averaging method (the long-time average of a quantity or ensemble average, proposed by Osborne Reynolds, 1842-1912), Reynolds-averaged Navier-Stokes (RANS) approaches have been the most prevalent until now. The effect of turbulent fluctuations appears in a Reynolds-stress term that must be modeled if the system is to be closed. Reynolds-stress models are successful (whereas turbulent viscosity models are not) in calculations that concern flows with significant mean streamline curvature, flows with strong swirls or mean-rotating phases, secondary flows in ducts, and flows with rapid variations in the mean flow. However,

Reynolds-stress models are not very reliable for flows in which large scale unsteadiness is significant, such as the transitional flow and the flow over bluff bodies, which involves unsteady separation and vortex shedding. As Pomraning [85] observed, neither the ensemble-averaged experimental data nor the RANS simulations agree with any single instantaneous Particle Image Velocimetry (PIV) snapshot of the cylinder flow. In complex flows, for instance in the flow inside internal combustion engines, the Reynolds-averaging tends to smear out important structures and therefore may be inappropriate.

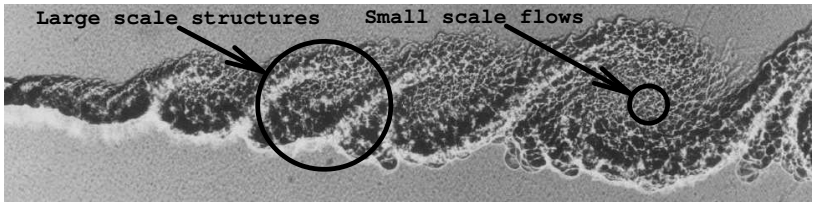


Figure 1.3: Visualization of the flow in a mixing flow (Brown & Roshko [13], reprinted with the permission of Cambridge University Press).

Large Eddy Simulation (LES) is a numerical technique for simulating turbulent flows first introduced by Smagorinsky [94] in 1963. LES requires less computational power than DNS but more than RANS. Kolmogorov's (1941) theory of self similarity implies that large eddies of a flow are dependent on geometry, while smaller eddies are self similar and have a universal character (Fig. 1.3). Therefore, it becomes a practice to solve only for large eddies explicitly and to model the effect of the smaller and more universal eddies on the larger ones. In LES, the large scale motions of the flow are calculated, while the effects of the smaller universal scales (the so called subgrid scales) are modeled through the use of a subgrid scale (SGS) model.

The main advantage of LES over computationally cheaper RANS is the increased level of detail that LES can deliver. While RANS provides "averaged" results, LES can predict instantaneous flow characteristics and resolve turbulent flow structures. In engine research, this is particularly valuable in simulations involving chemical reactions (Jhavar & Rutland [51]). While the "averaged" concentration of chemical species may be too low to trigger a reaction, there can be localized areas of high concentration in which reactions will occur. LES is also significantly more accurate than RANS for flows involving flow separation or acoustic prediction (You & Moin [115], Andersson et al. [1]).

This study examines variety SGS models in the LES of rotating turbulence. Turbulence subjected to system rotation provides a simple configuration for studying the characteristic features of both anisotropic turbulent flows and model performances in anisotropic turbulent flows. Thus, this study is important not only because of its practical applications but also its contribution to fundamental turbulence modeling.

Rotating turbulence is of great importance in engineering (Fig. 1.2(c)) and geophysics (Fig. 1.2(a)). The most significant application in the first case is the development and the design of turbo-machinery. Here one has to take into account the detailed properties of the turbulent fluids, which pass through the device and are rotated (e.g., by the motion of the turbine blades). A detailed understanding of rotational effects on flow characteristics is essential for an advanced layout of these machines. Second, the whole field of geophysics is crucially determined by planetary rotation, which influences both atmospheric and oceanic flows and affects global climate as well as short-term weather forecasting. Understanding the fundamental

processes in these fluid layer forms the basis for a detailed analysis of complex phenomena such as the development of climate anomalies like El Niño, the formation of hurricanes and tidal waves, the spreading of pollutants, and the oceanic circulation of nutrients.

The Rossby number characterizes the importance of rotational effects. If the Rossby number is smaller than 1 (Figs. 1.2(a) and 1.2(c)), rotation strongly affects the dynamics and the structures of turbulent flows through the Coriolis force. Many features of low-Rossby number rotating turbulence are well known. The tendency toward two-dimensionality (Cambon et al. [16, 15], Smith et al. [97]), the cyclonic/anti-cyclonic asymmetry in favor of cyclones (Smith & Lee [96], Morize et al. [76]), and the influence of the background rotation on the kinetic energy transfer, including the reduced transfer from large to small scales and the reverse energy transfer from small to large scales (Bardina et al. [4], Jacquin et al. [49], Mansour et al. [70], Cambon et al. [15], Yeung & Zhou [113], Smith et al. [97], Morinishi et al. [74]), are among the most challenging issues.

Many SGS models have been used to simulate rotating turbulence (Deardorff [31], Piomelli & Liu [82], Zikanov et al. [118]). However, there still exists a need for a better understanding of SGS models, both because anisotropic characteristics may influence LES modeling, and because comparative studies of model performance in rotating turbulence are inadequate. At least two issues should be considered.

- Algebraic eddy viscosity models predict global dissipation fairly accurately (Deardorff [31], Piomelli & Liu [82]). Through these models, small scales drain kinetic energy from large scales. However, kinetic energy transfer from small to large scales is known to occur, especially in anisotropic turbulence. In rotating

flows, although the rotation term (the Coriolis term) does not explicitly show up in the kinetic energy equation, rotation has an immediate effect on kinetic energy transfer and weakens the fundamental property of the energy cascade (Bardina et al. [4], Mansour et al. [70], Cambon et al. [15]). Eddy viscosity models may have difficulty capturing this process (Speziale [103], Domaradzki & Horiuti [32]).

- Most traditional SGS models are based on the assumption that the modeled small scale turbulence is nearly homogeneous and isotropic. In rotating turbulence, coherent structures (e.g., two-dimensionality, and cyclonic dominance) are affected by interactions between resonant velocity modes and between near-resonant modes (Smith et al. [97, 98, 96]). Our recent study found that the different micro-length scales occur in different directions and that this property can influence LES modeling (Lu et al. [66]).

## 1.2 Objective and approach

This study examines the performance of SGS models in order to develop models better suited to rotating turbulence. Two approaches, *a-priori* test and *a-posteriori* test, are used to achieve this goal.

At the *a-priori* test level, once a velocity profile is calculated by DNS or measured in experiment, the actual SGS stresses $\tau_{ij} = \overline{u_i u_j} - \overline{u}_i \overline{u}_j$ and the modeled SGS stresses can be generated and then be compared. The " $^-$ " represents spatial filtering at a scale $\Delta$. This comparison can identify the degree to which SGS models reproduce realistic properties of $\tau_{ij}$. Clark et al. [25], McMillan et al. [71], and Bardina et al. [2] are early examples of such studies. Piomelli et al. [83] used the name *a-priori*

test to point out that no actual LES is carried out. *A-priori* test using experimental data facilitates the study of high-Reynolds number flows. For example, using PIV data, Liu et al. [64, 65] observed the high correlation property of the Scale Similarity Model (SSM, Bardina et al. [2]) in isotropic turbulence. In 1996, Menon et al. [72] compared various SGS models at tensor, vector, and scalar levels using DNS data. A one-equation model named the subgrid Kinetic Energy Model (KEM, Deardorff [31]) consistently showed a higher correlation for a range of Reynolds numbers in comparison to other eddy viscosity models, such as the Smagorinsky Model (SM, Smagorinsky [94]), and the Dynamic Smagorinsky Model (DynSM, Germano et al. [39], Lilly [63]).

In our study, we use DNS data at moderate Reynolds and Rossby numbers to validate models. We consider the flow of an initially very low energy level isotropic random noise that then undergoes either large scale forcing or small scale forcing. Such problems have been studied extensively in the past in both experiments and numerical simulations (Lilly [62], Smith & Waleffe [97]).

In order to develop new models for rotating turbulence, we discuss rotation effects and examine whether or not the SGS models are consistent with the transformation properties of the SGS stress tensor in a non-inertial frame of reference undergoing rotation (Speziale [102, 103], Shimomura [93]). Kobayashi & Shimomura [54] and Horiuti [48] developed several models of rotating turbulence and obtained encouraging results. These models are consistent with the Material Frame Indifference (MFI) requirement for rotating flows. The consistent models are zero-equation models (e.g., algebraic closures) and not likely to satisfy the requirement that the trace of the SGS model equal twice the subgrid kinetic energy: $\tau_{ii}^{model} = 2k_{sgs}$. Hence,

we present two new one-equation approaches to LES for rotating turbulence. These new models are consistent with the constraints of MFI and also satisfy the trace requirement.

The primary tools that we use for the *a-priori* study are the regression and correlation coefficients. In 1979, Clark et al [25] introduced the correlation coefficient, $\rho$, to study whether modeled and actual terms are related. If $\tau_{ij}^{model}$ and $\tau_{ij}$ are totally unrelated, then $\rho(\tau_{ij}, \tau_{ij}^{model}) = 0$. If there is a linear relation, then $\rho(\tau_{ij}, \tau_{ij}^{model}) = 1$. The correlation coefficient describes the strength of an association between two variables, and is completely symmetrical. The correlation between $\tau_{ij}^{model}$ and $\tau_{ij}$ is the same as the correlation between $\tau_{ij}$ and $\tau_{ij}^{model}$.

In this study, we introduce the regression coefficient as another coefficient to examine the performance of models. The regression coefficient represents how much $\tau_{ij}^{model}$ changes with any given change of $\tau_{ij}$ and can be used to construct a regression line on a scatter plot of the two variables. For high-correlation models ($\rho > 0.6$ over a wide range of filter sizes), such as the SSM and the Gradient Model (GM, Clark et al. [25]), the regression coefficient is often more useful than the correlation coefficient. It gives a more complete description of the relationship between the two variables. A unit regression coefficient means that the modeled variable has the same magnitude as the variable obtained from the filtered DNS.

At the *a-posteriori* test level, we systematically investigate and compare the characteristic behaviors of SGS models in the actual LES of rotating turbulent flows. We test the following SGS models: the SM; the DynSM; the SSM and its mixed version, which is known as the Mixed Scale Similarity Model (MixSSM, Zang et al. [116], Vreman et al. [106]); the KEM; the Dynamic Structure Model (DSM, Pomraning &

Rutland [85, 86], Chumakov & Rutland [24]); and two new mixed one-equation models, Mixed Gradient type Consistent Dynamic Structure Model (MixGCDSM) and Mixed Similarity type Consistent Dynamic Structure Model (MixSCDSM). These models are important representatives of the available SGS models.

We work with two configurations of LES to assess these SGS models. We compare the LES results in the first configuration with filtered DNS results. To facilitate physical understanding and modeling, we isolate the rotation from other effects (such as forcing) and perform purely decaying turbulence. The Reynolds numbers in this configuration are low, which is necessary for the current computer capacity to perform an accurate DNS. The simulations in the second configuration are performed at a higher Reynolds number than in the first configuration. Flows are forced at both large scales and intermediate scales. We judge the LES results according to the anisotropic level of rotating turbulence including the cyclone structure, the kinetic energy transfer from small to large scales, and the quasi two-dimensional structure. The second configuration is a more rigorous assessment, because traditional models fail to capture those features of rotating turbulence.

## 1.3 Outline

The remainder of this thesis is divided into seven chapters. Chapter 2 reviews the literatures on the pseudo-spectral method and basic LES concepts, and discusses and criticizes common SGS models. Chapter 3 covers conceptual issues, identifies strengths of new models, and introduces new SGS models for simulating rotating turbulence. Chapter 4 reviews previous methods for the *a-priori* test, and introduces

the regression coefficient. Chapters 5 and 6 present *a-priori* and *a-posteriori* results of the SGS models. Chapter 7 summarizes our research.

# Chapter 2

# Literature review

In order to solve the Navier-Stokes equations and the LES equations in a rotating frame, a pseudo-spectral method has been adopted in this research. This chapter begins with a review of the literature on this approach, then summarizes representatives SGS models. We then review work on the Rossby number, anisotropic features of rotating turbulence, and previous LES studies of rotating turbulence.

## 2.1 Pseudo-spectral method and forcing schemes

Since the invention of the modern digital computer in the 1940s, different numerical approaches have been proposed to solve Ordinary Differential Equations (ODEs) and Partial Differential Equations (PDEs). Spectral methods are one of four important techniques used in applied mathematics and scientific computing to numerically solve PDEs, which came into their own roughly in successive decades

1950s : finite difference methods

1960s : finite element methods

1970s : finite volume methods, spectral methods

Naturally, the origins of each method can be traced further back. For spectral methods, some of the ideas are as old as interpolation and expansion, and algorithmic developments arrived with Lanczos as early as 1938 (Lanczos [58, 59]). The earliest

applications of the spectral method to PDEs addressed spatially periodic problems and stemmed from work by Kreiss & Oliger [57] (who called it the Fourier method) and Orszag & Patterson [78] (who termed it pseudo-spectral). Two landmarks of the early spectral method literature are the short book by Gottlieb & Orszag [42], and the monograph by Canuto et al. [17].

Spectral methods, which have strengths in exponential convergence behavior and reduced numerical damping and dispersion properties, are an increasingly popular tool for solving ODE- and PDE-related problems in fluid mechanics, quantum mechanics, vibrations, linear and nonlinear waves, and complex analysis. The most frequently used expansions are trigonometric polynomials, Chebyshev polynomials, and Legendre polynomials. For example, spectral methods write the solution as a Fourier series (Eqn. (2.1) - 1D Fourier & inverse Fourier transfer example in a discrete manner), substituting this series into the PDEs to get a system of ODEs in the time-dependent coefficients of the trigonometric terms in the series (written in complex exponential form), and using a time-stepping method, such as a Runge-Kutta method, to solve those ODEs.

$$\begin{cases} u(n) = \sum_{k=-N/2}^{N/2-1} \hat{u}(k)\, e^{\frac{2\pi i}{N} kn} & , \quad n = 0,...,N-1 \\ \hat{u}(k) = \frac{1}{N} \sum_{n=0}^{N-1} u(n)\, e^{\frac{-2\pi i}{N} kn} & , \quad k = -N/2,...,N/2-1. \end{cases} \tag{2.1}$$

As an example, in order to solve the incompressible Navier-Stokes equations

$$\frac{\partial u_i}{\partial x_i} = 0\ , \ \frac{\partial u_i}{\partial t} + u_j \frac{\partial u_i}{\partial x_j} = -\frac{\partial p}{\partial x_i} + \nu \frac{\partial^2 u_i}{\partial x_j \partial x_j} + f_i\ , \tag{2.2}$$

quantities need to be transferred into Fourier space

$$u_i \mapsto \hat{u}_i \ , \tag{2.3}$$

$$u_j \frac{\partial u_i}{\partial x_j} \mapsto \widehat{N.L._i} \quad \text{(nonlinear term)} \ , \tag{2.4}$$

$$p \mapsto \hat{p} \quad \text{(pressure term)} \ , \tag{2.5}$$

$$\frac{\partial^2 u_i}{\partial x_j \partial x_j} \mapsto -k^2 \hat{u}_i \quad \text{(diffusion term)} \ , \tag{2.6}$$

$$f_i \mapsto \hat{f}_i \quad \text{(forcing term)} \ , \tag{2.7}$$

where the wave number vector is $\vec{k} = (k_1, k_2, k_3)$, and the magnitude of the wave number is $k = \sqrt{k_1^2 + k_2^2 + k_3^3}$. We solve the pressure term using the incompressible constraint, and then remove it from the momentum conservation equations to give

$$\frac{\partial}{\partial t}\hat{u}_i = -\nu k^2 \hat{u}_i + P_{ij}\left(\hat{f}_j - \widehat{N.L._j}\right) \ , \tag{2.8}$$

where the tensor $P_{ij} = \delta_{ij} - k_i k_j / k^2$ is the classical solenoidal projector and represents projections onto the plane perpendicular to $\vec{k}$ in Fourier space. In pseudo-spectral methods, the nonlinear term ($\widehat{N.L._i}$) is not directly calculated in Fourier space, but computed by the Fourier transfer of $u_j \frac{\partial u_i}{\partial x_j}$, which is calculated by the multiplication of $u_i$ and $\frac{\partial u_i}{\partial x_j}$ in physical space. Inverse Fourier transfer of $\hat{u}_i$ yields $u_i$, and inverse Fourier transfer of $-\mathfrak{i}\ \hat{u}_i k_j$ (where $\mathfrak{i} = \sqrt{-1}$) yields $\frac{\partial u_i}{\partial x_j}$. The advantage of pseudo-spectral methods for the nonlinear term is in the reduced multiplications from $O(N^2)$ to $O(N \log_2 N)$, where $N$ is the number of total grid points (Canuto et al. [17]).

Orszag & Patterson [78] laid the foundations of the pseudo-spectral method for turbulent studies at the National Center for Atmospheric Research in 1972. They performed a $32^3$ computation of isotropic turbulence at a Reynolds number (on the basis of Taylor micro-scales) of 35. The next major step was taken by Rogallo [90],

who, in 1981, combined a transformation of the governing equations with an extension of the Orszag-Patterson algorithm to compute homogeneous turbulence subjected to mean strain. By comparing the results with both theoretical and experimental data, Rogallo evaluated several turbulence models that set the standard for the DNS of homogeneous turbulence.

In this research, the DNS of rotating flows is based on the conservation laws of incompressible, homogeneous flow in a rotating frame, which are described as

$$\frac{\partial u_i}{\partial x_i} = 0 \ , \ \frac{\partial u_i}{\partial t} + u_j \frac{\partial u_i}{\partial x_j} = -\frac{\partial p}{\partial x_i} - 2\epsilon_{ijk}\Omega_j u_k + \nu \frac{\partial^2 u_i}{\partial x_j \partial x_j} + f_i \ , \tag{2.9}$$

where $p$ is the effective pressure, $\nu$ is the kinematic viscosity, $f_i$ is a forcing term, and $\Omega_i$ is the (constant) rotation rate. Without loss of generality, we chose $\overrightarrow{\Omega} = (0, 0, \Omega)$. Thus the Coriolis force can be simplified as $-2\Omega\epsilon_{i3k}u_k$.

We simulated DNS validation cases using a pseudo-spectral code, in which Smith et al. [97, 98, 96]) used a linear eigen-mode algorithm based on helical decomposition studies (Waleffe [109, 110]). Because the inviscid ($\nu \to 0$), linear ($u_j \frac{\partial u_i}{\partial x_j} \to 0$) limit of equations (2.9) have wave solutions, called inertial waves (Greenspan [43], Smith & Waleffe [97]). It is particularly appropriate to represent the velocity field as a superposition of wave solutions with amplitude $b_s(\vec{k}, t)$,

$$\vec{u} = \sum_{\vec{k}} \sum_{s=\pm 1} b_s(\vec{k}, t)\vec{h}_s(\vec{k}) e^{\mathrm{i}(\vec{k}\cdot\vec{x} - \omega_s t)} \ , \tag{2.10}$$

where the wave frequency is $\omega_s(\vec{k}) = 2\Omega s\frac{k_3}{k}$, and $\vec{h}_s = \vec{k} \times \vec{\Psi} + \mathrm{i}s\vec{\Psi}$ with $s = \pm 1$, $\vec{\Psi} = (\vec{k} \times \vec{e}_z)/|\vec{k} \times \vec{e}_z|$ and $\vec{e}_z = (0, 0, 1)$. The wave with $s = +1$ is right-handed and propagates in the $\vec{k}$ direction, while the $s = -1$ wave is left-handed and propagates

in the $-\vec{k}$ direction. The Navier-Stokes equations (2.9) in a rotating frame then yield

$$\left(\frac{\partial}{\partial t}+\nu t^2\right) b_s(\vec{k},t) = \frac{1}{2}\sum C^{s_k s_p s_q}_{\vec{k}\ \vec{p}\ \vec{q}} b^*_s(\vec{p},t) b^*_s(\vec{q},t) e^{\mathrm{i}(\omega_{s_k}+\omega_{s_p}+\omega_{s_q})t} \ , \tag{2.11}$$

where $b_s(\vec{k},t) = b^*_s(-\vec{k},t)$, with $^*$ denoting a complex conjugate. The sum is over all $\vec{p}$, $\vec{q}$ such that $\vec{k}+\vec{p}+\vec{q}=0$ and over all $s_p$, $s_q$, with $C^{s_k s_p s_q}_{\vec{k}\ \vec{p}\ \vec{q}} = (s_q q - s_p p)\times \left(\vec{h}^*_s(\vec{p})\times\vec{h}^*_s(\vec{q})\right)\cdot\vec{h}^*_s(\vec{k})/2$ . Note that this code is similar to codes used in other studies (Yeung & Zhou [113], Morinishi et al. [74, 75]). In these codes, the linear viscosity (diffusion) and the Coriolis terms are included with an integrating factor, which helps increase numerical stability and decrease numerical diffusion. The time advance in wave number space was carried out through the use of an explicit third order Runge-Kutta scheme (see appendix A).

We consider flow under the influence of either large scale or small scale forcing. For large scale forced isotropic turbulent runs, we compared the results using both the Overholt-Pope forcing scheme [79] and the Gaussian white-noise forcing scheme (Smith et al. [95, 97, 98]). The Overholt-Pope forcing scheme defines the forcing in Fourier space as

$$\hat{f}_i = \frac{f_k(t)}{\tau}\hat{u}_i \ , \tag{2.12}$$

where $\tau$ is the forcing time scale, and the forcing coefficient $f_k(t)$ is a solution of the dynamic equation

$$\frac{df_k(t)}{dt} = \mathbb{P}\left(\frac{-1}{\tau}\ln\left(\frac{E(k)}{E_m(k)Z_f(k)}\right) - \alpha\alpha_c f_k(t)\right) = \mathbb{P}(S_k) \ , \tag{2.13}$$

where $E(k)$ is the kinetic energy spectrum, $\alpha$ is a nondimensional damping coefficient, $\alpha_c$ is the critical damping coefficient, $E_m(k)$ is the model spectrum, and $Z_f$ is a forcing

cut-off function to be defined. The operator $\mathbb{P}$ is defined as

$$\mathbb{P}(S_k) = \begin{cases} S_k, \text{ for} f_k > 0 \\ S_k, \text{ for} f_k = 0 \text{ and } S_k > 0 \\ 0, , \text{ for} f_k = 0 \text{ and } S_k \leqslant 0 \ . \end{cases} \tag{2.14}$$

The forcing cut-off function is defined as

$$Z_f(k; k_f, \zeta) = \tanh\left(\frac{k_f - k}{\zeta k_f} H(k_f - k)\right) \ , \tag{2.15}$$

where $H$ is the Heaviside function. The time scale coefficient is

$$T_f^* = \frac{\tau}{\tau_\eta} \ , \tag{2.16}$$

where $\tau_\eta = K/\varepsilon$ denotes the eddy turn-over time. $K$ is the total kinetic energy, and $\varepsilon$ is the dissipation rate of kinetic energy. The case of isotropic turbulence has been performed using the Overholt-Pope scheme with parameters $\zeta = 0.25$, $T_f^* = 0.4$, $\alpha_c = 2\sqrt{2}/\tau$ and $\alpha = 0.7$. The results for isotropic turbulence are insensitive to the forcing scheme, but the approach to the statistically steady state was faster when we used the Overholt-Pope forcing.

In rotating and other anisotropic turbulent flows, the Gaussian white-noise forcing allows for the study of the nonlinear interactions with minimal bias from the forcing. Thus for our rotating turbulent runs, we used white-noise forcing with a Gaussian spectrum

$$F(k) = \varepsilon_f \frac{exp(-0.5(k - k_f)^2/\sigma^2)}{(2\pi)^{1/2}\sigma} \ , \tag{2.17}$$

where the forcing peak wave number is $k_f$, the standard deviation is $\sigma = 1$ and the kinetic energy input rate is $\varepsilon_f = 1$.

In order to study flow behavior over a wide inertial range, the dissipation at small scales was modeled using hyper-viscosity $(-1)^{p_u+1}\nu_u(\nabla^2)^{p_u}\vec{u}$ with $p_u = 8$ (Borue & Orszag [10, 11]). In some cases, we added hypo-viscosity $(-1)^{p_i+1}\nu_i(\nabla^2)^{-p_i}\vec{u}$ with $p_i = 2$ to destroy box-size vortices. Drawing on both the work done by Chasnov [20] and dimensional analysis, we used

$$\nu_u = 2.5\left(\frac{E(k_{max},t)}{k_{max}}\right)^{1/2} k_{max}^{2-2p_u}\ ,\ \nu_i = \left(\frac{E(k_{min},t)}{k_{min}}\right)^{1/2} k_{min}^{2+2p_i}\ , \tag{2.18}$$

where $k_{max}$ is the highest available wave number, which is set according to the 2/3 de-aliasing rule (Canuto et al. [17]), and where $k_{min}$ is the smallest wave number ($k_{min} = 1$ on our isotropic grid).

## 2.2 LES and SGS models

This section gives a chronological review of Large Eddy Simulation (LES) formalism, along with various subgrid scale (SGS) models developed since 1963.

### 2.2.1 LES equations for rotating flow

In industrial and environmental applications, where Reynolds numbers are usually very high, direct numerical simulation of turbulence is generally impossible, because the very wide range that exists between the largest and the smallest dissipative scales cannot be explicitly simulated even on the largest and most powerful computers. Fortunately, of greater interest are the larger scales of turbulent flows: those that control turbulent diffusion of momentum or scalar (e.g., concentration of chemical species, and heat). In the LES approach, an implication of Kolmogorov's (1941) theory of self similarity is that the large eddies of the flow are dependent on geometry whereas the small scales are more universal. This feature enables one to explicitly

solve for the large scale motions, whereas the effect of the small scales is modeled according to a so-called SGS model (Rogallo & Moin [91]). The LES approach comprises the following major steps

1. Filtering separates the large scales from the small scales. The resolved component $\overline{f}(\vec{x})$ is derived via the convolution integral $\overline{f}(\vec{x}) = \int f(\vec{x}')G(\vec{x},\vec{x}';\Delta)\,d\vec{x}'$ with the filter function $G(\vec{x},\vec{x}';\Delta)$. A residual component is defined as, $f' = f - \overline{f}$. The resolved velocity field $\overline{u}_i$, which is three-dimensional and time-dependent, represents the motions of the large eddies. The residual velocity field represents the small scale motions. Our study has employed the following filters

$$\text{Gaussian:} \qquad G = K_1 \exp\left(-6\frac{|\vec{x}-\vec{x}'|^2}{\Delta^2}\right) \tag{2.19}$$

$$\text{cut-off:} \qquad G = K_2 \prod_{i=1\ldots3} \frac{sin(\pi(x_i - x_i')/\Delta)}{\pi(x_i - x_i')/\Delta} \tag{2.20}$$

$$\text{top hat:} \qquad G = \begin{cases} K_3 & \text{if } |x_i - x_i'| < \frac{1}{2}\Delta,\ i = 1\ldots3 \\ 0 & \text{otherwise} \end{cases} \tag{2.21}$$

$$\text{triangle:} \qquad G = \begin{cases} K_4(\Delta - 2|\vec{x}-\vec{x}'|) & \text{if } |x_i - x_i'| < \frac{1}{2}\Delta,\ i = 1\ldots3 \\ 0 & \text{otherwise} \end{cases} \tag{2.22}$$

The coefficient $K_i$ is a normalization factor, which ensures that the integral of the filter equals unity (in the discrete sense). Figure 2.1 demonstrates the easiest-to-understand scenario using the kinetic energy spectrum of a typical isotropic turbulence.

2. Applying grid filtering to the Navier-Stokes equations (2.9) gives the LES equations including the SGS stress tensor in the momentum equations

$$\frac{\partial \overline{u}_i}{\partial x_i} = 0\ ,\ \frac{\partial \overline{u}_i}{\partial t} + \overline{u}_j\frac{\partial \overline{u}_i}{\partial x_j} = -\frac{\partial \overline{p}}{\partial x_i} - 2\Omega\epsilon_{i3k}\overline{u}_k + \nu\frac{\partial^2 \overline{u}_i}{\partial x_j \partial x_j} + \overline{f}_i - \frac{\partial \tau_{ij}}{\partial x_j}\ , \tag{2.23}$$

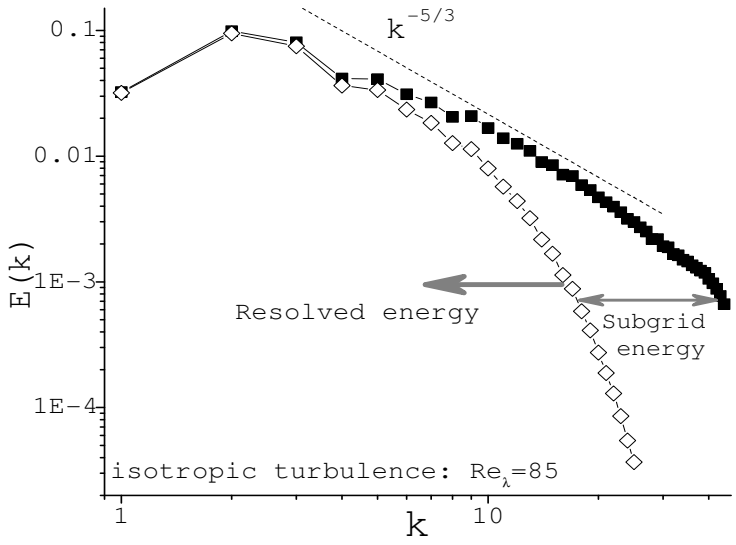


Figure 2.1: Three-dimensional kinetic energy spectrum $(-\blacksquare-)$ of a $128^3$ isotropic turbulence. We obtained the LES resolved kinetic energy spectrum $(-\diamondsuit-)$ by using Gaussian filtering.

where the SGS stress tensor is $\tau_{ij} = \overline{u_i u_j} - \overline{u}_i \overline{u}_j$. On purpose, we have not subtracted the trace.

3. Closure is obtained through modeling of the SGS stress tensor. The following section provides a brief overview of SGS models. On the basis of some mathematical and physical constraints, we developed new one-equation models for rotating turbulence (see chapter 3).

4. Finally, the LES equations are numerically solved for the resolved field, which provides an approximation of the large scale motions in one realization of the turbulent flow.

### 2.2.2 Overview of traditional SGS models

In the LES of incompressible turbulent flows, we require a SGS model for the SGS stress tensor. This term can be classically decomposed into three parts, the modified Leonard term $L_{ij}^M$, the modified cross term $C_{ij}^M$, and the modified SGS Reynolds stress term $R_{ij}^M$ (Germano [38], Pope [87])

$$\tau_{ij} = L_{ij}^M + C_{ij}^M + R_{ij}^M \ , \tag{2.24}$$

where $L_{ij}^M = \overline{\overline{u}_i \overline{u}_j} - \overline{\overline{u}}_i \overline{\overline{u}}_j$, $C_{ij}^M = \overline{\overline{u}_i u_j'} + \overline{u_i' \overline{u}_j} - \overline{\overline{u}}_i \overline{u_j'} - \overline{u_i'}\,\overline{\overline{u}}_j$, $R_{ij}^M = \overline{u_i' u_j'} - \overline{u_i'}\,\overline{u_j'}$.

In addition, consider the Gaussian filter, which is an isotropic filter ($G(\vec{x}, \vec{x}'; \Delta) = G(\vec{r} = \vec{x} - \vec{x}'; \Delta)$) and has the second moments

$$\int r_i r_j G(\vec{r}; \Delta)\, d\vec{r} = \frac{\Delta^2}{12} \delta_{ij} \ , \tag{2.25}$$

and finite higher moments. This filter is applied to a turbulent flow, with a filter width of $\Delta$. For a given $\vec{x}$, and for $\vec{r}$ on the order $\Delta$, the velocity $U(\vec{x} + \vec{r})$ can be expanded in the Taylor series

$$u_i(\vec{x} + \vec{r}) = u_i(\vec{x}) + \frac{\partial u_i}{\partial x_k} r_k + \frac{1}{2!} \frac{\partial^2 u_i}{\partial x_k \partial x_l} r_k r_l ... \ , \tag{2.26}$$

where the velocity gradients are evaluated at $\vec{x}$. Spatial filtering shows that the filtered velocity field is

$$\overline{u}_i(\vec{x}) = u_i(\vec{x}) + \frac{\Delta^2}{24} \frac{\partial^2 u_i}{\partial x_k \partial x_k} + O(\Delta^4) \ . \tag{2.27}$$

A similar procedure (Leonard [60], Clark et al. [25], Horiuti [45], Pope [87]) shows that the SGS stress tensor is (to leading order)

$$\tau_{ij} = \overline{u_i u_j} - \overline{u}_i \overline{u}_j = \frac{\Delta^2}{12} G_{ij} + O(\Delta^4) \ , \tag{2.28}$$

where the gradient term is defined as

$$G_{ij} = \frac{\partial \overline{u}_i}{\partial x_a} \frac{\partial \overline{u}_j}{\partial x_a} \ . \tag{2.29}$$

As will be explained, some SGS models make explicit use of the decomposition (2.24) or the Taylor expansion (2.28). The modified Leonard term, the modified cross term and the gradient term will surface frequently in subsequent discussions.

#### 2.2.2.1 Smagorinsky model

Based on the Boussinesq hypothesis [12], a common class of SGS models describes the trace-free part of the SGS tensor using the form

$$\tau_{ij} - \frac{\tau_{kk}}{3}\delta_{ij} \approx -2\nu_t \overline{S}_{ij} \ , \tag{2.30}$$

where the strain rate tensor is $\overline{S}_{ij} = \frac{1}{2}\left(\partial \overline{u}_i/\partial x_j + \partial \overline{u}_j/\partial x_i\right)$ and $\nu_t$ is the eddy viscosity. Several different models have been used for the eddy viscosity. Based on the equilibrium assumption of decaying isotropic turbulence that the entire dissipation is statistically equal to the kinetic energy that small scales receive from resolved scales, the first expression for the eddy viscosity $\nu_t$ was introduced in 1963 by the meteorologist Smagorinsky [94]. According to the Smagorinsky Model (SM), the eddy viscosity is determined as

$$\nu_t = C_s^2 \Delta^2 |\overline{S}| \ , \tag{2.31}$$

where $|\overline{S}| = (2\overline{S}_{mn}\overline{S}_{mn})^{1/2}$ and $C_s$ is a dimensionless coefficient. The value of $C_s$ can be determined from isotropic turbulence decay and analysis (Lilly [61], Pope [87]); if the cutoff, $k_c = \pi/\Delta$, lies within a $k^{-5/3}$ Kolmogorov cascade $E(k) = C_{\mathbb{K}}\varepsilon^{2/3}k^{-5/3}$ (where $C_{\mathbb{K}}$ is the Kolmogorov constant), one can adjust the constant $C_s$, which takes

values between 0.1 and 0.2, so that the ensemble averaged subgrid kinetic energy dissipation is identical to $\varepsilon$. A Kolmogorov constant of 1.4 obtained through measurements in the atmosphere (Champagne [19]) yields $C_s \sim 0.18$. In this research, we adopt $C_s = 0.18$ for high-Reynolds number (regarding LES resolutions) turbulence (Lilly [61]).

Smagorinsky was simulating a two-layer quasi-geostrophic model in order to represent large (synoptic) scale atmospheric motions. Limited by the computational power of the time, in 1970, Deardorff [30] was the first to implement the SM for the wall layer of a channel flow at a finite Reynolds number. The SM assumes that the principal axes of the strain rate tensor are aligned with those of the SGS stress tensor. However, at the *a-priori* test level, the SGS stress tensor correlates very poorly with the rate of strain tensor (Clark et al. [25], Liu et al. [64], Menon et al. [72]). Further, the SM is purely dissipative - kinetic energy transfers only from resolved scales to subgrid scales. For numerical stability, this is a desirable characteristic of the model. However, the actual SGS stress may also facilitate kinetic energy transfer from subgrid to resolved scales in a process referred to as "backscatter". Further, in anisotropic turbulence there can be a net transfer of kinetic energy from subgrid to resolved scales (Smith et al [97, 98]). Also, the SM has turned out to be too dissipative for many studies (Friedrich & Nieuwstadt [36], Vreman et al. [108]), including Smagorinsky's research in 1963 (Smagorinsky [94]), in which the use of hyper-viscosity like (high-order Laplacian) dissipative operators is preferred (Basdevant & Sadourny [8], Ferziger [35]). In addition, for complex flows, it may not be possible to find a universal coefficient that is appropriate for the entire domain at all times.

#### 2.2.2.2 Gradient model and scale similarity model

Since the 1970s, the Taylor expansion (2.28) of the SGS stress has been studied (Leonard [60], Clark et al. [25]). The Gradient Model (GM, sometimes referred to as a "nonlinear model" or "Clark model") takes the leading term of this Taylor expansion, by which the SGS stress is modeled as

$$\tau_{ij} \approx \frac{\Delta^2}{12} G_{ij} \ . \tag{2.32}$$

The GM has several advantages: it is computationally efficient because it is a zero-equation model and does not require a second filtering; it satisfies Galilean invariance (Speziale [102, 103]) and modeled stresses are consistent with the constraints of Material Frame Indifference (see section 3.1); at the *a-priori* test level, it successfully predicts the SGS stress tensor over a wide range of filter sizes ($\rho > 0.6$, Liu et al. [64]); and it allows for "backscatter." However, simulations with the pure GM appear to be unstable (Vreman et al. [107]).

The eddy viscosity closures (2.30) assume a one-to-one correlation between the SGS stress tensor and the strain rate tensor. The analysis of fields obtained from DNS has displayed very little correlation between the two tensors (Clark et al. [25], McMillan & Ferziger [71]). Liu et al. [64] confirmed this lack of correlation for a much higher Reynolds number flow using the experimental data taken in the far field of a turbulent round jet. This disadvantage led Bardina [2] to propose the original scale similarity model in 1980. This model is based on the assumption that the SGS stress is similar to the smallest resolved stress; thus, the SGS stress can be approximated from the resolved field. We have studied a modified version of the Scale Similarity

Model (SSM) which satisfies Galilean invariance (Speziale [102, 103])

$$\tau_{ij} \approx C_L L_{ij}^M \ , \tag{2.33}$$

where $C_L$ is a dimensionless coefficient - the so-called similarity coefficient, and we used $C_L = 1$ in this study.

In LES, the SSM and the GM perform similarly. At the *a-priori* test level, the modeled SGS stress deduced from (2.33) exhibits a good correlation ($\rho > 0.6$) with the SGS stress over a wide range of filter sizes. The SSM also allows for "backscatter." When implemented in LES, however, the SSM hardly dissipates kinetic energy and appears to be unstable (Bardina [2, 3]). In contrast with the GM, the implementation of the SSM requires a second filtering operation on the resolved field, and the SSM is not MFI-consistent at the tensor level.

#### 2.2.2.3 Dynamic Smagorinsky model

The limitations of the SM have led to the formulation of SGS models that are more general. In the early 1990s, Germano et al. [39] and Lilly [63] proposed the dynamic procedure to compute the model coefficient; this model is called the Dynamic Smagorinsky Model (DynSM). In this model, the trace-free SGS stress is modeled as

$$\tau_{ij} - \frac{\tau_{kk}}{3}\delta_{ij} \approx -2C_D(\Delta)^2|\overline{S}|\overline{S}_{ij} \ . \tag{2.34}$$

The Germano [39] identity defines a test filter whose width $\widetilde{\Delta}$ is larger than the grid filter-width $\Delta$ (typically $\widetilde{\Delta} = 2\Delta$). The subtest scale stress $T_{ij} = \widetilde{\overline{u_i u_j}} - \widetilde{\overline{u}}_i \widetilde{\overline{u}}_j$ is similarly approximated according to

$$T_{ij} - \frac{T_{kk}}{3}\delta_{ij} \approx -2C_D\widetilde{\Delta}^2|\widetilde{\overline{S}}|\widetilde{\overline{S}}_{ij} \ . \tag{2.35}$$

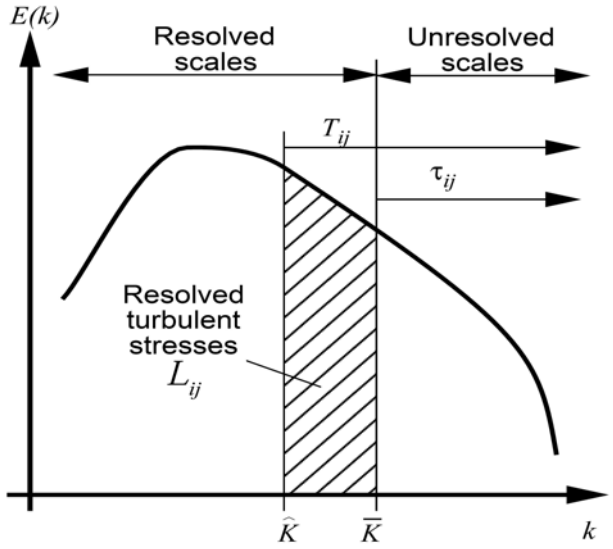


Figure 2.2: Schematic illustration of grid- and test-filtering for the dynamic model employing a cut-off filter.

Subtracting the test scale filtering of (2.34) from (2.35) gives

$$L_{ij} - \frac{L_{kk}}{3}\delta_{ij} \approx C_D M_{ij} \ , \tag{2.36}$$

where $L_{ij} = \widetilde{\overline{u}_i\overline{u}_j} - \widetilde{\overline{u}}_i\widetilde{\overline{u}}_j$ and $M_{ij} = 2\left(\Delta^2\widetilde{|\overline{S}|\overline{S}_{ij}} - \widetilde{\Delta}^2|\widetilde{\overline{S}}|\widetilde{\overline{S}}_{ij}\right)$. The error is $e_{ij} = L_{ij} - \frac{L_{kk}}{3}\delta_{ij} - C_D M_{ij}$. When using the least-square-error approach, $\partial(e_{ij}e_{ij})/\partial C_D = 0$, the dynamic coefficient $C_D$ is found to be

$$C_D = \left(\frac{L_{ij}M_{ij}}{M_{kl}M_{kl}}\right) \ . \tag{2.37}$$

The DynSM has been applied to many flows with good results, including channel flow (Piomelli [81]), rotating channel flow (Piomelli & Liu [82]), and mixing layer (Ghosal & Rogers [41], Vreman et al. [108]). Unfortunately, analysis of DNS data (Lund et al. [69]) and experimental data (Liu et al. [64, 65]) has shown that the

$C_D$ predicted by (2.37) varies strongly in space and contains a significant fraction of negative values. Allowing negative values for $C_D$ is an advantage of the model because it implies kinetic energy transfers from subgrid to resolved scales in physical space. However, very large negative values of the eddy viscosity constitute a destabilizing process in a numerical simulation, and a nonphysical growth of the resolved scale kinetic energy has often been observed (Lund et al. [69]). Thus, the procedure of averaging $C_D$ over directions of statistical homogeneity has been introduced, and this procedure has yielded good agreement with both experimental and DNS results (Piomelli et al. [81, 82], Vreman et al. [108]).

#### 2.2.2.4 Mixed SGS model

It has been noted by Bardina et al. [3] that the SSM alone is not dissipative enough. Thus, a linear combination of the SSM and an eddy viscosity model has been introduced. In 1993, Zang et al. [116] proposed a dynamic mixed approach based on the Germano [39] identity to calculate the model coefficient. In 1994, Vreman et al. [106] introduced an improved version removing some mathematical inconsistencies. The Mixed Scale Similarity Model (MixSSM) is expressed as

$$\tau_{ij} \approx C_L L_{ij}^M - 2C_D^{SSM}\Delta^2|\overline{S}|\overline{S}_{ij} \ . \tag{2.38}$$

The dynamic model coefficient $C_D^{SSM}$ is obtained by integrating this model into the Germano [39] identity

$$C_D^{SSM} = \left( \frac{(L_{ij} - H_{ij}^{SSM})M_{ij}}{M_{kl}M_{kl}} \right) \ , \tag{2.39}$$

where the tensor $H_{ij}^{SSM}$ is defined as

$$H_{ij}^{SSM} = \widetilde{\overline{\overline{u}_i\overline{u}_j}} - \overline{\overline{u}}_i\overline{\overline{u}}_j - (\widetilde{\overline{u_iu_j}} - \widetilde{\overline{\overline{u}}_i\overline{\overline{u}}_j}) \ . \tag{2.40}$$

The Mixed Gradient Model (MixGM) is formulated as

$$\tau_{ij} \approx \frac{\Delta^2}{12} G_{ij} - 2C_D^{GM}\Delta^2|\overline{S}|\overline{S}_{ij} \ . \tag{2.41}$$

The dynamic model coefficient $C_D^{DM}$ is obtained through

$$C_D^{GM} = \left( \frac{(L_{ij} - H_{ij}^{GM})M_{ij}}{M_{kl}M_{kl}} \right) \ , \tag{2.42}$$

where the tensor $H_{ij}^{GM}$ is defined as

$$H_{ij}^{GM} = \frac{\widetilde{\Delta}^2}{12}\frac{\partial\widetilde{\overline{u}}_i}{\partial x_a}\frac{\partial\widetilde{\overline{u}}_j}{\partial x_a} - \frac{\Delta^2}{12}\widetilde{\frac{\partial\overline{u}_i}{\partial x_a}\frac{\partial\overline{u}_j}{\partial x_a}} \ . \tag{2.43}$$

Mixed models combine the strengths of similarity (or gradient) models and eddy viscosity models. This approach has been proven a great success in many applications, such as the flows of a lid-driven cavity (Zang et al. [116]), a mixing layer (Vreman et al. [108]), and rotating turbulence (Kobayashi & Shimomura [54]). It must be noted that the viscosity term does not degrade the *a-priori* results (Liu et al. [65]), because typically the magnitude of the first term in the models is significantly higher than that of the viscosity term ($\gtrapprox$ 50 times when measured in the $L_2$-norm).

#### 2.2.2.5 Subgrid kinetic energy model

The SM and its dynamic version (DynSM) use strain rate, $|\overline{S}|$, to represent the amount of subgrid kinetic energy in their SGS model formulas (2.31) & (2.34). They do not explicitly contain any information regarding the subgrid kinetic energy. Thus, a one-equation eddy viscosity model, the subgrid Kinetic Energy Model (KEM), was proposed for LES of turbulent flows (Carati et al. [18], Ghosal et al. [40]). It must be noted that since 1973, Deardorff [31] has used the KEM to study an atmospheric boundary layer turbulence. However, it was not until the 1990s that detailed studies

on its performance were achieved. The KEM has been evaluated at both the *a-priori* level and the *a-posteriori* level (Carati et al. [18], Ghosal et al. [40], Kim & Menon [53], Menon et al. [72]), and it has been widely used in industrial applications (Davidson et al. [27, 28, 29], Krajnović et al. [55, 56], Sohankar et al. [99, 100]). The full SGS stress is modeled as

$$\tau_{ij} \approx \frac{2}{3} k_{sgs} \delta_{ij} - 2\nu_k \overline{S}_{ij} \ , \tag{2.44}$$

where $k_{sgs} = \frac{1}{2}\left(\overline{u_k u_k} - \overline{u}_k \overline{u}_k\right) = \tau_{kk}/2$ is the SGS kinetic energy, and the SGS eddy viscosity is $\nu_k = C_k \sqrt{k_{sgs}} \Delta$. Note that using the Cauchy-Schwarz inequality, $|\mathbf{a} \cdot \mathbf{b}| \leqslant ||\mathbf{a}|| \cdot ||\mathbf{b}||$, and the definition of the SGS kinetic energy, it can be shown that the SGS kinetic energy is always positive for a non-negative filter, such as the Gaussian filter, the top hat filter, and the triangle filter (Ghosal et al. [40]).

To implement the model, there must be a method for determining $k_{sgs}$. The exact SGS kinetic energy equation is expressed as

$$\begin{aligned} \frac{\partial k_{sgs}}{\partial t} + \overline{u}_j \frac{\partial k_{sgs}}{\partial x_j} &= -\tau_{ij} \overline{S}_{ij} - \varepsilon + \nu \frac{\partial^2 k_{sgs}}{\partial x_j \partial x_j} \\ &- \left( \overline{u_i \frac{\partial P}{\partial x_i}} - \overline{u}_i \frac{\partial \overline{P}}{\partial x_i} \right) - \frac{\partial}{\partial x_j} \left( \frac{1}{2} \tau_{u_i u_i u_j} - \overline{u}_i \tau_{ij} \right) \end{aligned} \tag{2.45}$$

where $\varepsilon = \nu \left( \overline{\frac{\partial u_i}{\partial x_j} \frac{\partial u_i}{\partial x_j}} - \frac{\partial \overline{u}_i}{\partial x_j} \frac{\partial \overline{u}_i}{\partial x_j} \right)$, and $\tau_{u_i u_i u_j} = \overline{u_i u_i u_j} - \overline{u_i u_i}\ \overline{u}_j$. Appendix B gives a derivation of equation (2.45). An approximation for the SGS kinetic energy is obtained by solving the transport equation

$$\frac{\partial k_{sgs}}{\partial t} + \overline{u}_j \frac{\partial k_{sgs}}{\partial x_j} = -\tau_{ij} \frac{\partial \overline{u}_i}{\partial x_j} - C_c \frac{k_{sgs}^{3/2}}{\Delta} + \frac{\partial}{\partial x_j} \left[ \left( \frac{\nu_k}{\sigma_k} + \nu \right) \frac{\partial k_{sgs}}{\partial x_j} \right] \ . \tag{2.46}$$

Here, the three terms on the right-hand side represent, respectively, the production $(-\tau_{ij}(\partial \overline{u}_i/\partial x_j) = -\tau_{ij}\overline{S}_{ij})$, the dissipation $(\varepsilon)$, and the diffusion of the SGS kinetic

energy. The typical values for the constants are $C_k = 0.05$, $C_c = 1.0$ and $\sigma_k = 1.0$ (Yoshizawa & Horiuti [114]).

An important feature of this model is that it does not make the assumption of local balance between the subgrid scale kinetic energy production and dissipation rate. In addition, it improves the accuracy of SGS stress modeling in comparison to other eddy viscosity models (Menon et al. [72]). Also, the use of a transport equation for the subgrid scale kinetic energy may allow for coarser grids than can be used for a comparable problem with a zero-equation eddy viscosity model (Menon et al. [72]). However, the KEM does not improve the accuracy of off-diagonal components of SGS stress, $\tau_{ij,(i\neq j)}$; the correlations of off-diagonal components are generally less than 0.3 (Lu et al. [66]). In addition, although numerical stability is improved using the positive viscosity ($\nu_k \geqslant 0$), which results in the kinetic energy transfers from resolved to subgrid scales, this model is an eddy-viscosity model and cannot predict reverse kinetic energy transfers without requiring that $C_k$ be a function of time and space.

#### 2.2.2.6 Dynamic structure model

Ideally, a model is expected to accomplish three main objectives: (i) it can represent the SGS stress closely, so that it can give high correlations between the modeled stress and the actual SGS stress; (ii) it yields proper dissipation of kinetic energy from resolved scales and allow for "backscatter"; and (iii) it does not require *a-priori* knowledge to set model constants. In 2000, to address some of the mathematical and conceptual difficulties in SGS models, Pomraning & Rutland [85, 86] introduced a dynamic one-equation non-viscosity model, the Dynamic Structure Model (DSM). The DSM uses a tensor form of the SGS stresses: $\tau_{ij} = C_{ij} k_{sgs}$. Note that $C_{ij}$ must satisfy

$C_{ii} = 2$. Assuming the same form at the test filtering level, $T_{ij} = \widetilde{\overline{u_i}\overline{u_j}} - \widetilde{\overline{u}}_i\widetilde{\overline{u}}_j = C_{ij}K$, and integrating into the Germano [39] identity, one finds

$$T_{ij} - \widetilde{\tau}_{ij} = \widetilde{\overline{u}_i\overline{u}_j} - \widetilde{\overline{u}}_i\widetilde{\overline{u}}_j = C_{ij}K - \widetilde{C_{ij}k_{sgs}} \approx C_{ij}\left(K - \widetilde{k_{sgs}}\right) \ . \tag{2.47}$$

For this model, the structure of the SGS stress tensor is extracted from the Leonard term, and SGS kinetic energy helps predict the magnitude of SGS stress. For equal test and grid filter sizes, the DSM reduces to an algebraic model for the SGS stress tensor of the form

$$\tau_{ij} \approx \left(\frac{L_{ij}^M}{L_{mm}^M}\right) 2k_{sgs} \ . \tag{2.48}$$

The model is a one-equation model that needs a modeled SGS kinetic energy equation (2.46) to complete it.

The DSM has the advantages of both one-equation model and scale similarity model. The DSM does not assume the local balance between the subgrid scale kinetic energy production and the dissipation rate. This assumption is used to obtain the model coefficient for the SM. The model expression (2.48) does not include any coefficient. Therefore, the model does not require *a-priori* knowledge. Similar to the KEM, in a physical system, if all the kinetic energy available in the subgrid scales is removed, the modeled SGS stress will reach zero, thus quenching the effects of subgrid scales including reverse kinetic energy transfers. As expected, the DSM improves the accuracy of the SGS stress modeling by giving generally high correlations ($\rho > 0.6$). The DSM uses the Leonard term to model the structure of the SGS stress, so the model expression naturally satisfies the Galilean invariance. However, it is not MFI-consistent with the SGS stress. In chapter 3, we will discuss this problem in detail.

Many researchers have attempted to develop MFI-consistent models to overcome this problem (Shimomura [93], Kovayashi & Shimomura [54], Horiuti [48], Lu et al. [66]).

## 2.3 Rotating turbulence

In rotating turbulence, rotational effects enter through the Coriolis term in the Navier-Stokes equations (2.9). Many studies have noted both the development of anisotropy and the possible transition toward a quasi two-dimensional state. This section will review some well-known related facts.

### 2.3.1 Rossby numbers

Rotation rate is an external parameter. In order to study the importance of rotational effects and to compare the inertial force with the Coriolis force, researchers study the Rossby number, which characterizes the dimensionless ratio of the rotation time scale (the inverse of the Coriolis parameter $2\Omega$) to a nonlinear time scale. Several different Rossby numbers can be defined, depending on how one chooses to estimate the nonlinear time scale. With a nonlinear time scale based on the parameters of the Gaussian forcing (2.17), one Rossby number is defined as

$$Ro^G = \frac{(\varepsilon_f k_f^2)^{1/3}}{2\Omega} \ . \tag{2.49}$$

In addition, a macro-scale Rossby number $Ro^L$ and a micro-scale Rossby number $Ro^{\omega_3}$ are defined as

$$Ro^L = u'/(2\Omega L) \ , \ Ro^{\omega_3} = \omega_3'/(2\Omega) \ . \tag{2.50}$$

In these expressions, $u'$ is the root-mean-square (RMS) velocity fluctuation, $\omega_3'$ is the RMS vorticity in the z-direction, and $L = u'K/\varepsilon$ denotes a typical length scale, where

$K$ is the total kinetic energy, and $\varepsilon$ is the dissipation rate of the total kinetic energy $K$. When the Rossby number is large (either because $\Omega$ is small; or because $L$ is small, i.e., for small scale motions such as flow in a bathtub; or for large speeds), the effects of rotation can be neglected. A small Rossby number indicates that the effects of rotation are comparably large.

We use the Rossby number as a criterion for considering the rotational effects on the modeling of the SGS stress. The Rossby number under ordinary conditions (walking speed $u' = 5\ [MPH]$, $L = 1\ [m]$, planetary rotation) is about $15,000$. Lumley [67] stated that "the rotational effects on Reynolds stress can be disregarded and the principle of MFI is quite justified under ordinary conditions." Many physical phenomena (Figs. 1.2(a) and 1.2(c)), however, do not have a large Rossby number, for instance, the Rossby number of a typical hurricane is $\sim 1$, and the Rossby number of a typical gas turbine engine flow is $\sim 0.3$. In our study, rotating flows are performed at small micro-scale Rossby numbers $\sim 0.1$, which is an approximate Rossby number for flows in the Gulf Stream, and for synoptic scale flows at mid-latitudes (Pedlosky [80], Smith & Lee [96]). Speziale [103] has shown that when $\Omega \to \infty$ ($Ro \to 0$), eddy-viscosity models, which are MFI-inconsistent with the SGS stress, have difficulties predicting kinetic energy transfers between resolved and subgrid scales.

There are several challenges in the LES of rapidly rotating flow with Rossby numbers less than unity. Accurate computations will reproduce at least three important features (some more prominent in forced flow as compared to decaying turbulence): (i) significant net transfer of kinetic energy from small to large scales; (ii) the generation of large scale vortical columns, with the asymmetry of cyclones over anti-cyclones; and (iii) a tendency toward two-dimensional and two-component flow,

with much lower levels of kinetic energy in the velocity component parallel to the rotation axis. Furthermore, studies have suggested that numerical simulations are restricted by resolution constraints to moderately small Rossby numbers (Cambon et al. [15], Smith & Lee [96]). With guidance from previous studies, we have performed simulations over a range of Rossby numbers $0.1 < Ro^{\omega_3} < 0.4$ (Bartello et al. [7]), $Ro^L < 1$ (Cambon et al. [15]) and $Ro^G \approx 0.1$ (Smith & Lee [96]).

### 2.3.2 Anisotropy of rotating turbulence

Turbulent flow subject to solid-body rotation is of interest because it has a wide range of applications in engineering science, geophysics and astrophysics. Many studies have been done trying to explain the behavior of rotating turbulence, including experiments (Hopfinger et al. [44], Jacquin et al. [49], Baroud et al. [5, 6], Morize et al. [77, 76]), theoretical analysis (Yanase et al. [111], Cambon et al. [16, 15], and Smith et al. [97, 96] ), and numerical simulations (Squires et al. [104], Bartello et al. [7], Cambon et al. [14], Piomelli & Liu [82], Yeung & Zhou [113], Horiuti [47], Morinishi et al. [74], Kobayashi & Shimomura [54], Yang & Domaradzki [112]). Compared with isotropic turbulence, rotating turbulence has various special features in terms of kinetic energy transfer, energy spectra, and spatial structure.

#### Inhibition of the energy cascade

It is well known that rotation suppresses the turbulent kinetic energy transport to smaller scales (Bardina et al. [4], Jacquin et al. [49], Mansour et al. [70], Cambon et al. [15], Yeung & Zhou [113], Morinishi et al. [74]), and this suppression corresponds to a reduction of the dissipation rate (Cambon et al. [15], Morinishi et al. [74], Domaradzki & Yang [33, 112]). Varying $\Omega$, figure 2.3 shows the time-evolution of

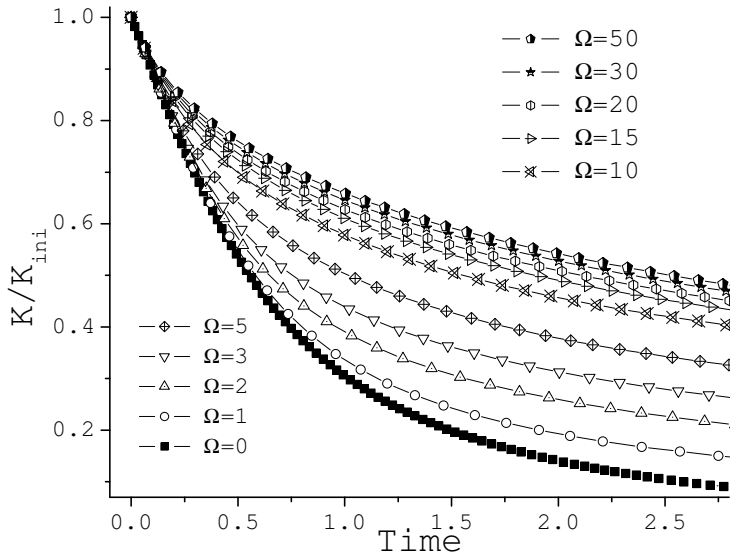


Figure 2.3: Evolutions of kinetic energy of flows under different rotation rates $[rad/s]$. Started from the same initial state - isotropic turbulence with $Re_\lambda = 85$ (see section 6.1.1). For the decaying rotating case with $\Omega = 20\,[rad/s]$, initially $Ro^{\omega_3} = 0.17$.

kinetic energy in decaying turbulent flows subject to rotation. Note that we have normalized time using initial eddy turn-over time ($K/\varepsilon$) for decaying turbulence. Starting from a high initial Rossby number, $Ro^{\omega_3} = 3.4$ (case with $\Omega = 1$ $[rad/s]$)), the inhibition effect is small and the kinetic energy decay is almost the same as for the non-rotating case. As initial $Ro^{\omega_3}$ decreases to 0.34 (case with $\Omega = 10$ $[rad/s]$), the effect becomes stronger and the kinetic energy decays slower. If initial $Ro^{\omega_3} = 0.34$ ($\Omega > 10$ $[rad/s]$) or less, there is little difference in the kinetic energy decay. Domaradzki & Yang [33, 112] presented findings consistent with these results.

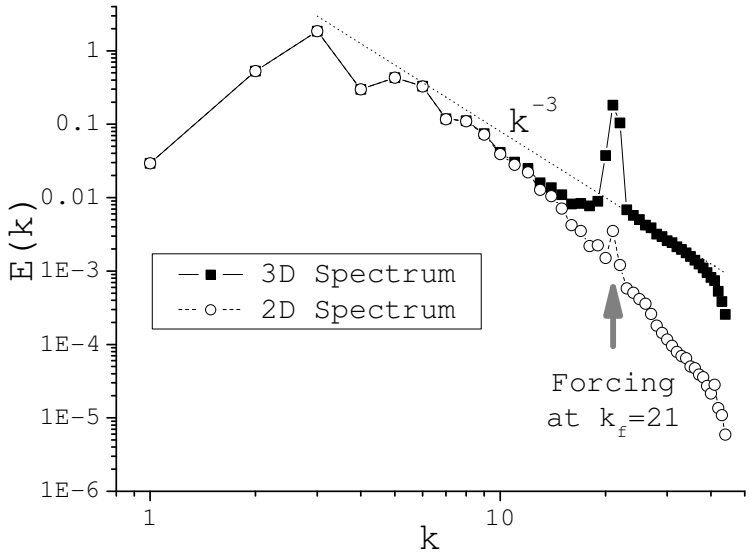


Figure 2.4: Kinetic energy spectrum of statistically steady state of rotating turbulent case B5.

### Spectral property

In studies of high-Reynolds number rotating turbulence, it has been observed that the inertial range energy spectrum is steeper than the Kolmogorov spectrum $E(k) \propto k^{-5/3}$ for isotropic turbulence; spectral exponent values between $-2$ and $-3$ have been reported in several studies (Zhou [117], Yeung & Zhou [113], Baroud et al. [5], Smith et al. [97, 96]). Recently, Bellet et al. [9] have shown that using a wave turbulence statistical model derived from a generalized Eddy Damped Quasi-Normal Markovian (EDQNM) theory, a $k^{-3}$ spectrum can be derived in the asymptotic limit of a quasi-infinite Reynolds number and a quasi-zero Rossby number. Figure 5.4 shows that, with forcing at small scales, kinetic energy transfers from small to large scales, and the scaling of the large scale spectrum of rotating turbulence is in a steeper

energy spectrum $E(k) \approx E(k_h, k_3 = 0) \propto k_h^{-3},\ k_h = \sqrt{k_1^2 + k_2^2}$ (Smith & Lee [96]). It also shows the collapse of the 2D and 3D spectra at large scales, indicating a two-dimensionalization of the velocity field. This case will be described in detail in section 5.1.

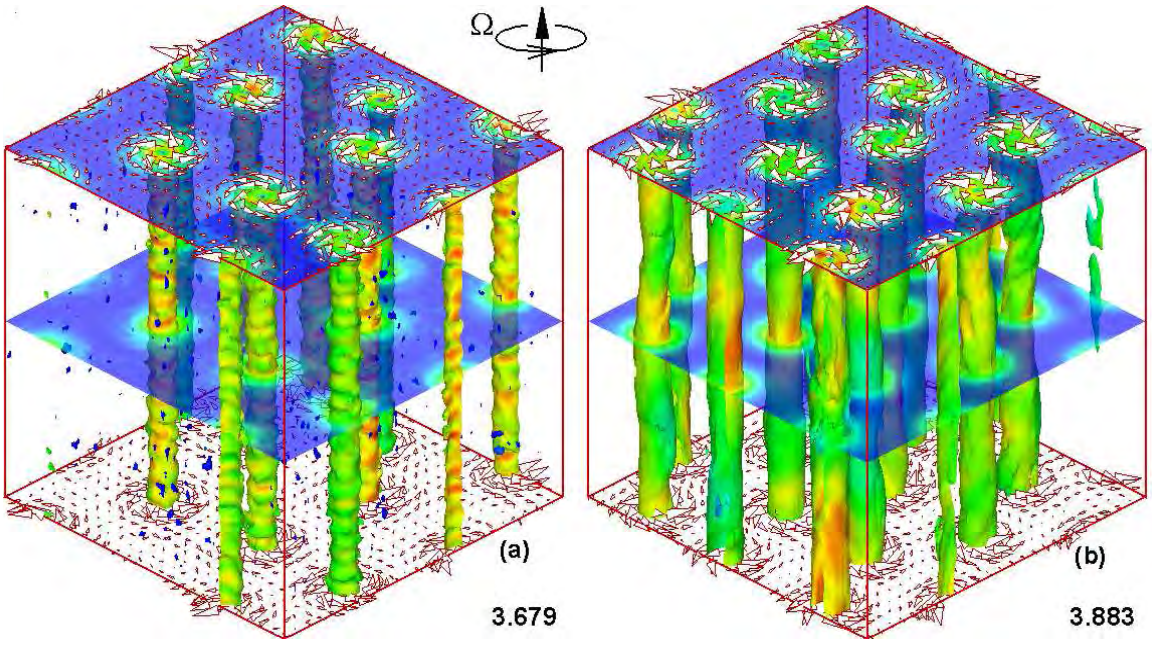


Figure 2.5: Cyclonic two-dimensional coherent structures appearing in rotating turbulence as indicated by iso-surfaces of vorticity, planar contours of kinetic energy and velocity vectors: (a) statistically steady state (at $time = 3.68$) of small scale forced rotating case B5. (b) statistically steady state (at $time = 3.88$) of large scale forced rotating case C3 (see section 5.1).

### Spatial structure and dimensionality

It has been noted that rotating turbulence with a moderate Rossby number below an $O(1)$ critical value accompanies asymmetry in favor of large scale cyclonic vortical columns (Smith et al. [97, 96]). This cyclone/anti-cyclone asymmetry is

widely observable in atmospheric science. Figure 1.2(a) shows that the direction of rotation of large scale wind flow (e.g., hurricanes & typhoons) is counterclockwise in the northern hemispheres (clockwise in the south). It is interesting to note that small scale rotating turbulent flows in the atmosphere, in which the direct influence of planetary Coriolis effect is inconsequential, are usually triggered by large scale cyclonical storms, and approximately more than 90% of tornadoes rotate in a cyclonic direction. Figure 2.5 shows that rotating turbulence captures this asymmetry, and a quasi two-dimensional flow - in other words, reduced variations along the rotation axis (Cambon et al. [16, 15], Smith & Lee [96]).

These features are related to each other. However, the Taylor-Proudman theorem [1] says nothing about the kinetic energy level in the velocity component parallel to the rotation axis as compared to the kinetic energy level in the velocity component perpendicular to the rotation axis. Thus, the theorem does not predict the observed tendency toward two-dimensional and two-component flow, with much lower levels of kinetic energy in the parallel velocity component ($u_3 \ll u_1,\ u_3 \ll u_2$, Cambon et al. [15], Smith & Waleffe [97]). A recent study has explored the assertion that resonant triads ($\omega_s(\vec{k}) + \omega_s(\vec{p}) + \omega_s(\vec{q}) = 0$) and near-resonant triads ($\left[\omega_s(\vec{k}) + \omega_s(\vec{p}) + \omega_s(\vec{q})\right]/(2\Omega) = O(Ro)$) are responsible for increased kinetic energy transfer to large scales resulting in steeper large scale kinetic energy spectra $E(k) \approx E(k_h, k_3 = 0) \propto k_h^{-3}$, as well as strong asymmetry in favor of cyclones (Smith & Lee [96]).

[1] If $Ro \lll 1$, the Taylor-Proudman theorem concludes that, $(\vec{\Omega} \cdot \nabla)\vec{u} = 0$. Assuming $\Omega_1 = 0$, $\Omega_2 = 0$, and $\Omega_3 = \Omega$, we have $\partial\vec{u}/\partial z = 0$.

Length scale properties of rotating turbulence can be considered as a consequence of its spatial structure and dimensionality. In previous studies, integral length scales were used to investigate nonlinear interactions modified by rotation (Cambon et al. [16, 15]). They are defined as

$$L_{ij}^{k} = \int_0^\infty \frac{< u_i(\vec{x}) u_j(\vec{x} + r\vec{n}^k) >}{< u_i(\vec{x}) u_j(\vec{x}) >} \, dr \ , \tag{2.51}$$

where $\vec{n}^k$ is the unit vector along the direction axis $x_k$, and $< \cdot >$ represents the arithmetic mean.

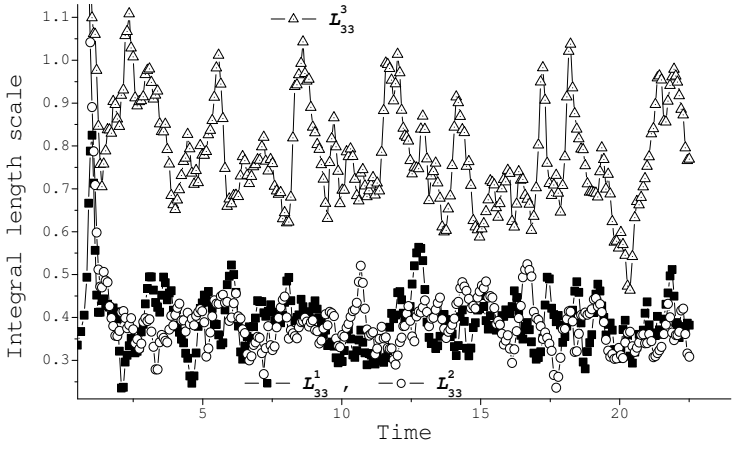


Figure 2.6: Evolutions of integral length scale, in isotropic turbulent case A (see section 5.1). Statistically, $L_{ii}^{i} = 2L_{jj}^{k}$, $(j \neq k)$ is illustrated.

For isotropic turbulence, as shown in figure 2.6, we can statistically obtain

$$L_{ii}^{i} = L_{jj}^{j} \ , \ L_{ii}^{j} = L_{ll}^{m} \ , \ L_{ii}^{i} = 2L_{ll}^{m} \ , \ (i \neq j \ , \ l \neq m \ , \text{ no summation}) \ . \tag{2.52}$$

Figure 2.7 shows that, for rotating turbulence, the two-dimensional process makes it

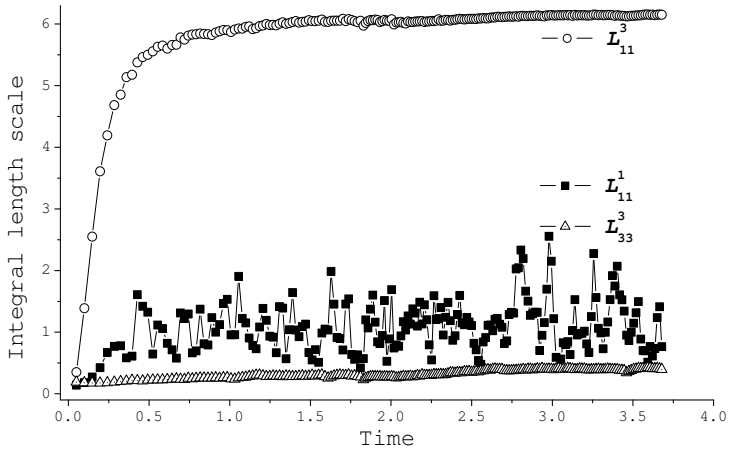


Figure 2.7: Evolutions of integral length scale, in small scale forced rotating turbulent case B5.

possible to obtain inequalities of integral length scales in terms of

$$L_{11}^3 > L_{11}^2 \quad ; \quad L_{11}^3 > \frac{1}{2} L_{11}^1 \text{ (even } L_{11}^3 > L_{11}^1 \text{ for some cases)} \tag{2.53}$$

$$L_{22}^3 > L_{22}^1 \quad ; \quad L_{22}^3 > \frac{1}{2} L_{22}^2 \text{ (even } L_{22}^3 > L_{22}^2 \text{ for some cases)} \tag{2.54}$$

$$L_{33}^3 > 2L_{33}^1 \quad ; \quad L_{33}^3 > 2L_{33}^2 \ . \tag{2.55}$$

Also, it is observed that

$$L_{11}^1 > L_{33}^3; \ L_{22}^2 > L_{33}^3 \ . \tag{2.56}$$

These findings are consistent with the results of previous studies (Cambon et al. [16, 15]).

In LES modeling, however, we focus on Taylor micro-scales because it is expected that these scales are affected more by the SGS model performance. Introduced in 1935, Taylor micro-scales come from correlation concepts and are fundamental to the description of the length scales of turbulence, even if the flow is anisotropic (Taylor

[105]). Taylor micro-scales are expressed as

correction: should be
sqrt(2<u_i * u_j>/<du_i/dx_k * du_j/dx_k>)

$$\lambda_{ij}^{k} = \sqrt{2 < u_i >< u_j > / \left( \langle \partial u_i / \partial x_k \rangle \langle \partial u_j / \partial x_k \rangle \right)} \ . \tag{2.57}$$

There are two sets of Taylor micro-scales. Longitudinal micro-scales are defined as $\lambda_{f,i} = \lambda_{ii}^{i}$ (no summation), and transverse micro-scales are defined as $\lambda_{g,ik} = \lambda_{ii}^{k}$ (no summation). As an example, $\lambda_{g,12}$ describes how quickly the x-component velocity changes with a change of distance in the y-direction.

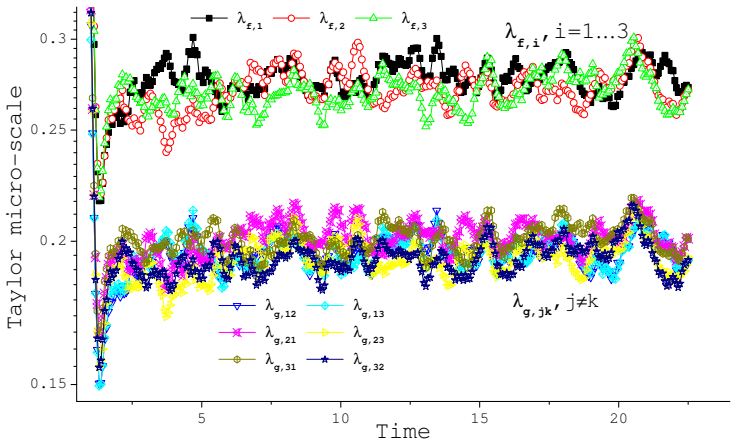


Figure 2.8: Evolutions of Taylor micro-scale, in isotropic turbulent case A. Statistically, $\lambda_{f,i}/\lambda_{g,jk} = \sqrt{2},\ (j \neq k)$ is illustrated.

Isotropic turbulence has identical longitudinal and transverse micro-scales, and it can be obtained analytically that

$$\lambda_{f,i}/\lambda_{g,jk} = \sqrt{2},\ (j \neq k) \ . \tag{2.58}$$

Figure 2.8 shows the length scale evolution in forced isotropic turbulent case A.

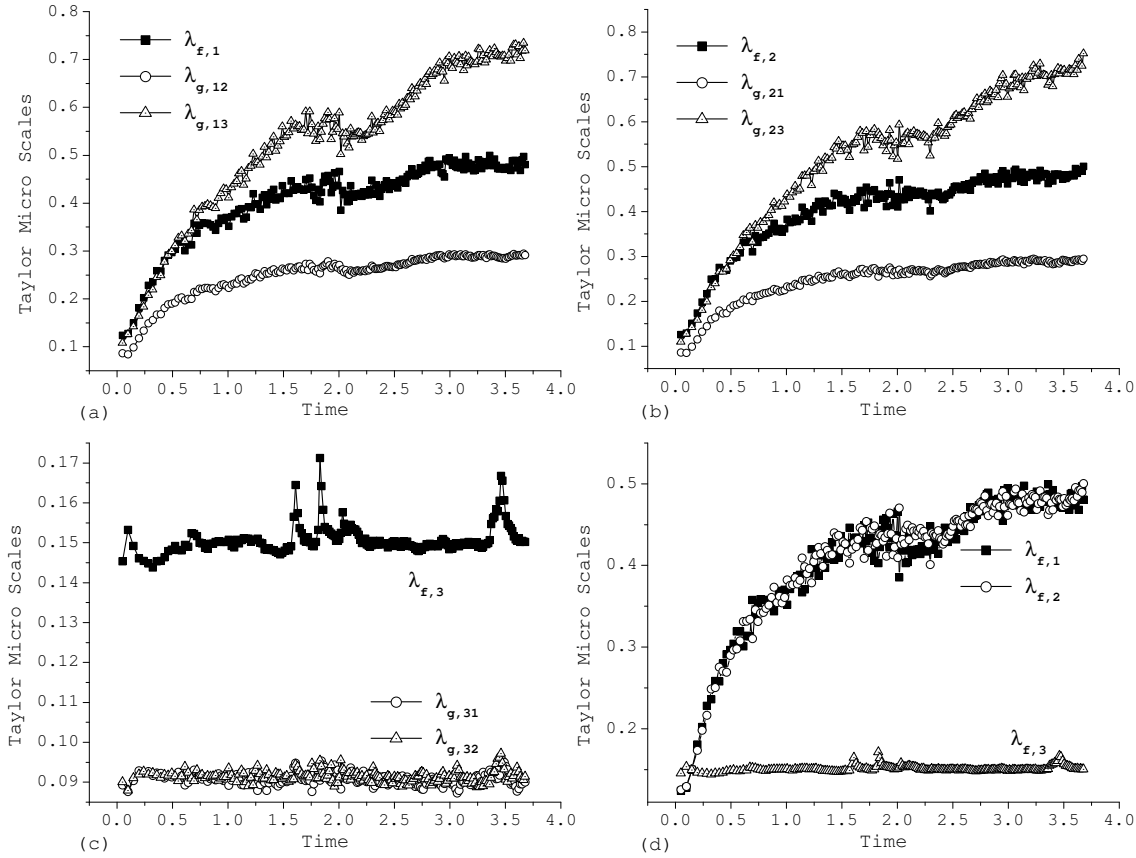


Figure 2.9: Evolutions of Taylor micro-scale, in small scale forced rotating turbulent case B5.

Figure 2.9 shows that, for rotating turbulence, the two-dimensionalization process makes that for a same velocity component, the Taylor micro-scales in the z-direction larger than the Taylor micro-scales in other directions, in terms of

$$\lambda_{g,13} > \lambda_{g,12} \quad ; \quad \lambda_{g,13} > \frac{1}{\sqrt{2}}\lambda_{f,1} \text{ (even } \lambda_{g,13} > \lambda_{f,1} \text{ for some cases)} \tag{2.59}$$

$$\lambda_{g,23} > \lambda_{g,21} \quad ; \quad \lambda_{g,23} > \frac{1}{\sqrt{2}}\lambda_{f,2} \text{ (even } \lambda_{g,23} > \lambda_{f,2} \text{ for some cases)} \tag{2.60}$$

$$\lambda_{f,3} > \sqrt{2}\lambda_{g,31} \quad ; \quad \lambda_{f,3} > \sqrt{2}\lambda_{g,32} \ . \tag{2.61}$$

However, for different velocity components, as shown in figure 2.9(d), the longitudinal micro-scale in the z-direction of a typical rotating turbulence is smaller than the scales in other directions

$$\lambda_{f,1} > \lambda_{f,3};\ \lambda_{f,2} > \lambda_{f,3}\ . \tag{2.62}$$

These relations are true for all cases of rotating turbulence in this study, and in section 5.3.2, we will use these relations to explain the effect of anisotropy on LES modeling.

## 2.4 LES of rotating turbulence

LES enables simulation of high-Reynolds number turbulent flows, and provides more details of flow structure than RANS. Very high Reynolds numbers ($\gtrsim 10^{11}$, Fig. 1.2(a)) generally accompany most geophysical flows, in which the rotational effects have significant implications due to their small Rossby numbers. Thus, Deardorff [31] introduced the KEM, and applied it to study 3D atmospheric turbulence in 1973. He obtained improved results concerning the flow motions and the heat flux near and above the top of a convective planetary boundary layer. That is the earliest example of the LES of rotating turbulence. After the DynSM was developed in 1995, Piomelli & Liu [82] applied it to a channel flow involving rotation. They identified large scale longitudinal vortices, and these findings were consistent with experimental observations and DNS results. Considering some fundamental drawbacks of traditional SGS models, Domaradzki et al. [32, 33, 112] introduced their Truncated Navier-Stokes (TNS) equation approach for estimating subgrid scales. Because energy spectrum is used to determine viscosities, the TNS approach is not practical for engineering applications. However, using the TNS, Yang & Domaradzki [112] studied the behaviors

of rotating turbulence with very high Reynolds numbers ($\sim 10^{15}$). Their results were in good agreement with experimental observations.

Using SGS models to simulate rotating turbulence, however, involves many challenges and difficulties. It has been shown that initially isotropic turbulence subjected to the action of the Coriolis force decays slower in time than its non-rotating counterpart for which the rotational effects are absent (Fig. 2.3). Also, at high Reynolds numbers, the inertial range energy spectrum in rotating cases is steeper than the Kolmogorov $k^{-5/3}$ fall off for isotropic turbulence (Fig. 5.4). This behavior presents a significant challenge for traditional SGS models, which are usually optimized for isotropic cases, and then have to be modified to account for rotation. For instance, the SM using a constant $C_s \sim 0.18$ is appropriate for isotropic turbulence, but significantly overestimates kinetic energy decay rates for rotating turbulence. The DynSM offers an improvement over the SM because the Smagorinsky constant becomes a variable and its mean is usually smaller. However, even the DynSM overestimates the energy decay at high rotation rates (Horiuti [47]). Second, the strain rate closure forces kinetic energy to flow only from resolved to subgrid scales. This closure does not fulfil the expectation that SGS models may also facilitate "backscatter," especially for anisotropic turbulence. In addition, traditional SGS models assume that the modeled small scale turbulence is nearly isotropic, but this is not true for rotating turbulence. As mentioned above, different micro-length scales occur in different directions. This property may influence LES modeling (Lu et al. [66]).

A more fundamental problem is that the modeled stress is required to have the same transformation properties between reference frames as the actual SGS stress. The first invariant property of SGS models is Galilean invariance, which has been

studied over 20 years (Speziale [102]). The second consideration is the transformation properties of SGS models in a non-inertial frame of reference undergoing rotation (Speziale [103], Shimomura [93], Kobayashi et al. [54], Horiuti [48]). As far as rotational transformation properties are concerned, MFI-consistent models are more attractive because they satisfy the transformation constraints. We note that most traditional models, such as the SM, the DynSM, the KEM, the SSM, the MixSSM and the DSM, are not consistent with this constraint. Studies have proven that the consistency of the GM is true (Speziale [103], Shimomura [93], Kobayashi et al. [54], Horiuti [48]). Note that the TNS approach is also MFI-consistent because it has no explicit modeling expression of SGS stress. Chapter 3 treats these topics in greater detail because we take the invariant properties of SGS models as a basic assumption to develop new models for rotating turbulence.

# Chapter 3

# Building new models

Most of the models discussed in the last chapter are based on the assumption of small scale isotropy. For instance, the SSM uses a single coefficient $C_L$ to set the magnitudes of all six modeled stress components ($\tau_{ij}$). For rotating turbulence, however, it is not clear if isotropy is achieved even at the smallest scales of motion, and different Taylor micro-scales have been observed in different directions (see section 2.3.2). Further, we study LES modeling from a fundamental aspect, the invariance of SGS models.

## 3.1 The invariance of SGS models

With a view toward developing models that are more suitable for the LES modeling of rotating turbulence, it is helpful to consider the invariance properties of the full equations and of models.

Galilean invariance of LES modeling has been studied for over 20 years (Speziale [102]). The Navier-Stokes equations as well as their filtered forms (2.23) are invariant under the Galilean group of transformations, $\mathbf{x}^* = \mathbf{x} + \mathbf{V}t + \mathbf{B}$. The SGS stress tensor is also invariant, $\tau_{ij} = \tau^*_{ij}$, under the Galilean transformation. As a cautionary remark, SGS models are required to exhibit the same (invariant) feature as the SGS stress

tensor. Fortunately, except for the original scale similarity model ($\tau_{ij} \approx \overline{\overline{u}_i \overline{u}_j} - \overline{u}_i \overline{u}_j$) of Bardina [2], all other recent models satisfy Galilean invariance.

Second, consistency with Material Frame Indifference (MFI) has been considered as one constraint of SGS models under the Euclidean group of transformations, $\mathbf{x}^* = \mathbf{Q}(t) \cdot \mathbf{x}$ (Speziale [103], Shimomura [93], Kobayashi & Shimomura [54], Horiuti [48]). Here, we briefly review this issue. We denote a proper orthogonal rotation matrix ($\mathbf{Q} \cdot \mathbf{Q}^T = \mathbf{I}$) as $Q_{ij}$, and $x_i^*$ ($u_i^*$) is the position (velocity) vector in a rotating frame. The principle of MFI ($Q_{ia} t_{ab} Q_{bj}^T = t_{ij}^*$, where $t_{ij}$ are components of an arbitrary tensor) has been applied as a principle for constitutive relations in the Navier-Stokes equations (Segel [92]). However, the SGS stress tensor $\tau_{ij}$ in an inertial frame is connected to the SGS stress tensor $\tau_{ij}^* = \overline{u_i^* u_j^*} - \overline{u_i^*}\ \overline{u_j^*}$ in a rotating frame according to a frame different expression

$$Q_{ia} \tau_{ab} Q_{bj}^T = \tau_{ij}^* + Z_{ij}^* \ , \tag{3.1}$$

where $Z_{ij}^*$ is given by

$$\begin{aligned} Z_{ij}^* = \quad & \epsilon_{iab} \Omega_a^* \left( \overline{x_b^* u_j^*} - \overline{x_b^*}\ \overline{u_j^*} \right) + \epsilon_{jab} \Omega_a^* \left( \overline{x_b^* u_i^*} - \overline{x_b^*}\ \overline{u_i^*} \right) \\ & + \epsilon_{iab} \epsilon_{jcd} \Omega_a^* \Omega_c^* \left( \overline{x_b^* x_d^*} - \overline{x_b^*}\ \overline{x_d^*} \right) \ , \end{aligned} \tag{3.2}$$

and where $\Omega_i^*$ is the angular velocity of the rotating frame. For the Gaussian filter, the quantity $Z_{ij}^*$ is analytically expanded to be

$$Z_{ij}^* = \frac{\Delta^2}{12} \left( \epsilon_{iab} \Omega_a^* \frac{\partial \overline{u_j^*}}{\partial x_b^*} + \epsilon_{jab} \Omega_a^* \frac{\partial \overline{u_i^*}}{\partial x_b^*} + \Omega_a^* \Omega_a^* \delta_{ij} - \Omega_i^* \Omega_j^* \right) + O(\Delta^4) \ . \tag{3.3}$$

This Taylor expansion shows that the rotational effects on $\tau_{ij}$ and LES models decay as ($\Delta^2$). Furthermore, it can be shown that the tensor $Z_{ij}^*$ is divergence free with

$\partial Z^*_{ia}/\partial x^*_a = 0$, leading to frame indifference of the vector $\partial \tau^*_{ij}/\partial x^*_j$

$$Q_{ia}\frac{\partial \tau_{ab}}{\partial x_b} = \frac{\partial \tau^*_{ia}}{\partial x^*_a} \ . \tag{3.4}$$

Since $\partial \tau_{ij}/\partial x_j$ appears in the LES momentum equation (2.23), and not the tensor $\tau_{ij}$ itself, one may argue that SGS models need only satisfy the MFI-consistency on the vector level (3.4), rather than on both the vector level (3.4) and the tensor level (3.1). However, the stress tensor $\tau_{ij}$ itself is important for the SGS kinetic energy equation, and thus we adopt the point of view that as a rigorous principle, a modeled stress tensor should satisfy, $Q_{ia}\tau^{model}_{ab}Q^T_{bj} = \tau^{*,model}_{ij} + Z^*_{ij} + (Z^{*,model}_{ij} - Z^*_{ij})$ with $Z^{*,model}_{ij} - Z^*_{ij} = 0$, just as the actual stress tensor does in equation (3.1) (Horiuti [47, 48], Shimomura [93], Kobayashi & Shimomura [54]). Note that the ratio of $\tau_{ij}$ (and $\tau^*_{ij}$) to $Z^*_{ij}$ can also be characterized by a Rossby number. For rotating turbulence at small micro-scale Rossby numbers, we do not apply the principle of MFI to the SGS stress (Horiuti [48]), but consider rotational effects for small scale turbulence. Otherwise, SGS modeling error caused by rotational frame transfers, $Z^{*,model}_{ij} - Z^*_{ij}$, will be added into a fluid dynamic system for different rotational frames (inertial frame: $\Omega = 0$).

Speziale [103] has stated that without concerning the effects of rotation, eddy-viscosity models have difficulty predicting energy transfers between resolved and sub-grid scales when $\Omega \to \infty$ ($Ro \to 0$). As the rotation rate of the framing increases, the GM (2.32) has the correct damped-dissipation behavior for rotating turbulence (Speziale [103]). Requiring (3.1), some traditional SGS models, such as the SM and the SSM, are MFI-inconsistent. It has been stated that the GM and the $L^M_{ij} + C^M_{ij}$

are MFI-consistent (Speziale [101], Shimomura [93], sometimes referred to as "form invariant").

## 3.2 MFI-consistent dynamic structure models

Even thought the original DSM has been shown to have excellent agreement with the actual SGS stresses for isotropic turbulence (Pomraning & Rutland [86], Chumakov & Rutland [24]), this model is not MFI-consistent. Thus, for rotating turbulence, we developed two models in the DSM family that are MFI-consistent.

Recall that the stresses corresponding to the gradient model (2.32) are MFI-consistent (Kobayashi & Shimomura [54]). Thus, we propose the Gradient type Consistent Dynamic Structure Model (GCDSM) for rotating flows

$$\tau_{ij} \approx \left( \frac{G_{ij}}{G_{mm}} \right) 2k_{sgs} \ , \text{ where } G_{ij} = \frac{\partial \overline{u}_i}{\partial x_k} \frac{\partial \overline{u}_j}{\partial x_k} \ . \tag{3.5}$$

A second model can be formed using the fact that $L_{ij}^M + C_{ij}^M$ is MFI-consistent (Shimomura [93] and Kobayashi et al. [54]). We propose the Similarity type Consistent Dynamic Structure Model (SCDSM) with the form

$$\tau_{ij} \approx \left( \frac{\Upsilon_{ij}}{\Upsilon_{mm}} \right) 2k_{sgs} \ , \tag{3.6}$$

where the Leonard term plus the cross term is modeled as $\Upsilon_{ij}$,

$$\Upsilon_{ij} = C_L L_{ij}^M + C_C \left[ \left( \overline{\overline{\overline{u}}_i \overline{u}_j} - \overline{\overline{u}}_i \overline{\overline{u}}_j \right) + \left( \overline{\overline{u}_i \overline{\overline{u}}_j} - \overline{\overline{u}}_i \overline{\overline{u}}_j \right) - 2 \left( \overline{\overline{\overline{u}}_i \overline{\overline{u}}_j} - \overline{\overline{\overline{u}}}_i \overline{\overline{\overline{u}}}_j \right) \right] \ . \tag{3.7}$$

When the cross term $C_{ij}^M$ is approximated in the form of the generalized scale similarity model (Horiuti [46]), $C_C$ and $C_L$ are both $O(1)$ dimensionless coefficients. Appendix C gives the derivation of the modeling expression of $C_{ij}^M$. In this study, $C_C$ is set to 1.5, and $C_L$ is set to 1.

## 3.3 Mixed version of MFI-consistent DSM

In simulations of rotating turbulence, we introduce a linear combination of new models and a hyper-viscosity term (Basdevant & Sadourny [8], Ferziger [35])

$$\text{MixGCDSM} \quad : \quad \tau_{ij} \approx \left( \frac{G_{ij}}{G_{mm}} \right) 2k_{sgs} + \nu_4 \nabla^2 \overline{S}_{ij} \tag{3.8}$$

$$\text{MixSCDSM} \quad : \quad \tau_{ij} \approx \left( \frac{\Upsilon_{ij}}{\Upsilon_{mm}} \right) 2k_{sgs} + \nu_4 \nabla^2 \overline{S}_{ij} \tag{3.9}$$

where hyper-viscosity $\nu_4$ can be modeled as $\nu_4 = C_k' \Delta^3 \sqrt{k_{sgs}}$, which is $O(\Delta^4)$, and can be treated as a model of the second term of the Taylor expansion of the SGS stress (2.29). The model coefficient $C_k'$ can be determined by a modification of the dynamic procedure illustrated in section 2.2.2.4. For simplicity, we set a small empirical value for this coefficient, $C_k' = 0.008$.

We adopt the hyper-viscosity term for two major reasons: (i) at the *a-posteriori* test level, we find that there exists a need of including an eddy-viscosity term, because for high-Reynolds number turbulent flows, the GCDSM and the SCDSM do not dissipate enough kinetic energy at small scales and typically are unstable; (ii) traditional eddy-viscosity (Bardina et al. [3], Zang et al. [116], Vreman et al. [106]) is too dissipative at large scales, and does not facilitate capturing some anisotropic features of rotating turbulence, such as the quasi two-dimensional flow at large scales, and reverse energy transfer to large scales. It is important to note that the magnitude of the structure term is significantly higher than that of the hyper-viscosity term, and the hyper-viscosity term does not degrade the *a-priori* results of the original unmixed version.

# Chapter 4

# Correlation and regression

A common method of evaluating SGS models is through *a-priori* tests in which models are compared to filtered DNS results. This serves as a standard testing technique for SGS models that is used as an initial evaluation and comparison of models. Later, tests of the most promising models will be made using LES codes in *a-posteriori* tests.

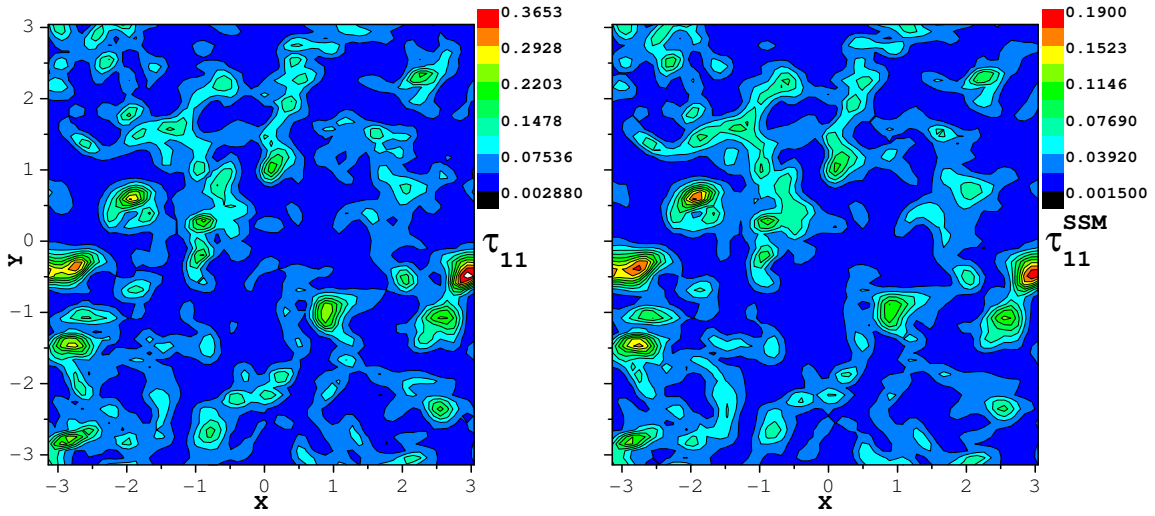


Figure 4.1: Contour plots of SGS stress $\tau_{11}$ (left) and scale similarity modeled stress $\tau_{11}^{SSM}$ (right) at $z = 0$ layer in isotropic turbulent case A. Gaussian filtering with $k_c = 32$ is used for the SSM. $\tau_{11}$ and $\tau_{11}^{SSM}$ have similar structures but different contour levels whose ratio is given by regression coefficient: $\beta(\tau_{11}, \tau_{11}^{SSM}) = 0.52$.

A qualitative *a-priori* evaluation can be made by comparing representative contour plots such as the ones shown in figure 4.1. Here $\tau_{11}$ from the SSM and a filtered DNS simulation of isotropic flow are compared. The model can duplicate much of the general structure of $\tau_{11}$ but the magnitudes of the contour levels are significantly different. This evaluation helps to reveal which models duplicate more details of SGS stresses and which models can capture average behavior but may miss details.

More quantitative *a-priori* evaluations can be made using Probability Density Functions (PDF) of relative errors such as

$$E = \frac{\tau_{ij}^{model} - \tau_{ij}}{\tau_{ij}} \ , \tag{4.1}$$

shown in figure 4.2 (Chumakov & Rutland [23]), and by scatter plots of modeled terms verses filtered DNS terms as shown in figure 4.3. In many situations, the main character of the scatter plots can be described by a linear regression. The linear regression equation, $b = \beta \cdot a + \alpha$, represents the relationship between variables a and b. Generally, $\alpha = 0$ in LES modeling. The slope of the linear correlation line, $\beta$, and the scatter around this correlation line, $\rho$, provide convenient measures of SGS models in *a-priori* tests. Note that $\beta$ is related to the ratio of the contour levels in figure 4.1, to the mean of $PDF(E)$ in figure 4.2 and to the slope of the linear curve fit in figure 4.3. Also, $\rho$ is related to the variance of $PDF(E)$ in figure 4.2 and to the scatter around the linear line in figure 4.3.

Conventionally, $\beta$ is called the regression coefficient and $\rho$ is called the correlation coefficient. The regression coefficient is evaluated by a least squares fit leading to

$$\beta(a,b) = \frac{< ab > - < a >< b >}{< a^2 > - < a >^2} \ , \tag{4.2}$$

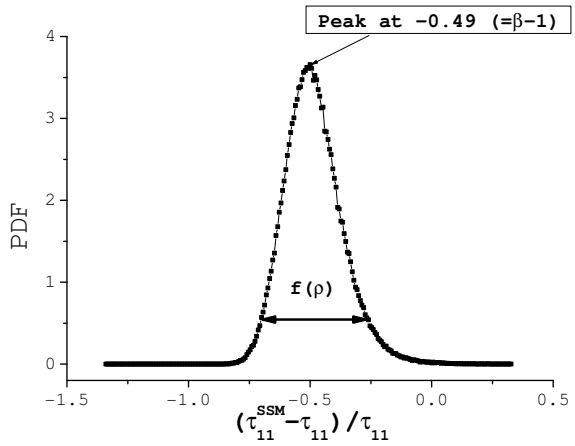


Figure 4.2: PDF of the relative errors of $\tau_{11}$. Same settings as figure 4.1. Peak position can be calculated via $\beta - 1$.

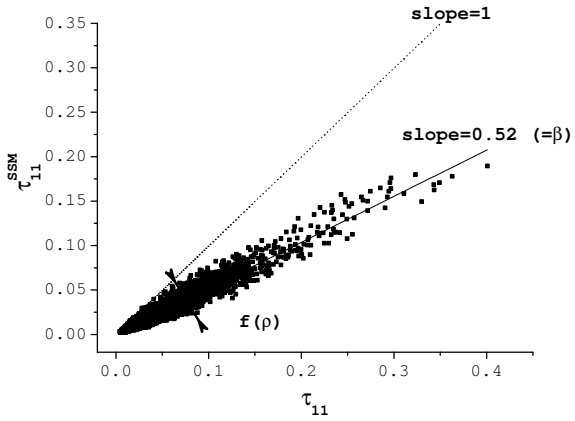


Figure 4.3: Scatter plot of $\tau_{11}$. Same settings as figure 4.1. Slope of the scatter line is predicted by regression coefficient $\beta$ directly.

with optimal value $\beta = 1$. The correlation coefficient is evaluated by

$$\rho(a,b) = \frac{< ab > - < a >< b >}{\sqrt{(< a^2 > - < a >^2)(< b^2 > - < b >^2)}} \ . \tag{4.3}$$

The range of $\rho$ is -1 to 1 with negative values of $\rho$ rarely occurring in LES *a-priori* testing and values close to one indicating a strong correlation.

The two coefficients $\beta$ and $\rho$ are global factors rather than local factors. A decrease from the value $\rho = 1$ in the correlation indicates a loss of ability to capture the correct resolved flow structure, and a departure from the value $\beta = 1$ in the regression indicates a loss of ability to capture the correct magnitude level of resolved flow quantities. Menon et al. [72] showed that even when there was similarity between the resolved structures, the peak values predicted by the SSM could be quite different from the actual values (about 25% lower for their cases). The regression coefficient can be used to describe this difference quantitatively.

The regression and correlation coefficients are the primary tools used in the current *a-priori* tests. Several different aspects of the SGS models are tested. Tests of individual tensor components as the terms $a$ and $b$ in equations (4.3) and (4.2) are indicated by dual subscripts: $\rho_{ij} = \rho(\tau_{ij}, \tau_{ij}^{model})$ and $\beta_{ij} = \beta(\tau_{ij}, \tau_{ij}^{model})$. Tests of the components of the divergence of $\tau_{ij}$, which appears in the momentum equation, are indicated by single subscripts: $\rho_i = \rho(\frac{\partial \tau_{ij}}{\partial x_j}, \frac{\partial \tau_{ij}^{model}}{\partial x_j})$ and $\beta_i = \beta(\frac{\partial \tau_{ij}}{\partial x_j}, \frac{\partial \tau_{ij}^{model}}{\partial x_j})$. Tests of the kinetic energy production term, $P = -\tau_{ij}\frac{\partial \overline{u}_i}{\partial x_j}$, are indicated by no subscripts: $\rho(P) = \rho(-\tau_{ij}\frac{\partial \overline{u}_i}{\partial x_j}, -\tau_{ij}^{model}\frac{\partial \overline{u}_i}{\partial x_j})$ and $\beta(P) = \beta(-\tau_{ij}\frac{\partial \overline{u}_i}{\partial x_j}, -\tau_{ij}^{model}\frac{\partial \overline{u}_i}{\partial x_j})$.

# Chapter 5

# *A-priori* test

Once fully developed turbulent flows are calculated by DNS or measured experimentally, the actual $\tau_{ij}(\vec{x},t)$ and the modeled $\tau_{ij}^{model}(\vec{x},t)$ can be generated, and *a-priori* tests of SGS models can be performed. Such a comparison requires data at high spatial resolution that are sufficient to resolve the SGS range. In 1979, Clark et al. [25] performed the earliest example of such studies accomplished by numerical calculation. Besides numerical simulations, an alternative is the use of experimental data. This approach enables the study of high-Reynolds number flows, but is limited by experimental techniques. For instance, Liu et al. [64, 65] used planar PIV to measure four tensor elements by means of a spatial filtering in two directions.

In this study, numerically simulated isotropic turbulence and numerically simulated rotating turbulence cases were used with the goal of improving performance through the new models, GCDSM (3.5) and SCDSM (3.6).

## 5.1 Case description

Here we introduce the main cases: isotropic turbulence forced at large scales (case A); rotating turbulence forced at small scales (B series); rotating turbulence forced at large scales (C series). In all cases, the domain is a periodic cube of volume

$(2\pi)^3$ and flows are resolved using $128^3$ Fourier modes. All flows were initialized with low energy isotropic noise, and the force was turned on at time zero.

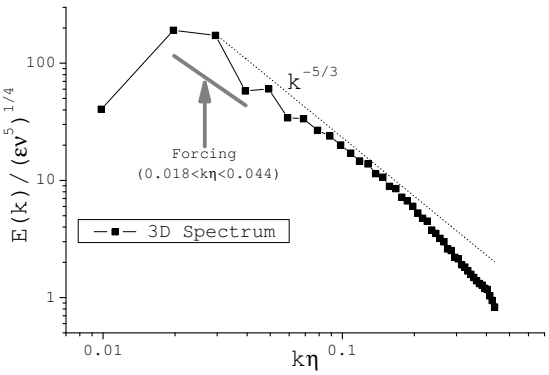


Figure 5.1: Kinetic energy spectrum of statistical steady state of isotropic turbulent case A.

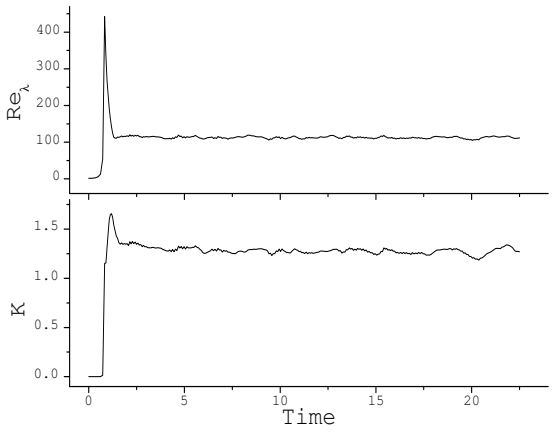


Figure 5.2: Evolutions of kinetic energy and micro Reynolds number of isotropic turbulent case A.

Case A is an isotropic turbulence forced at large scales ($1.9 < k_f < 4.5$) using Overholt-Pope's forcing scheme. A kinematic viscosity of 0.0013 leads to a statistical steady state with Taylor micro-scale Reynolds number $Re_\lambda = 100$. The spectrum of the final state is shown in figure 5.1. The wave number is normalized by the Kolmogorov length scale, $\eta = (\nu^3/\varepsilon)^{1/4} = 0.01$, and for convenience, a $-\frac{5}{3}$ power law is shown as a dotted line. Figure 5.2 shows the evolutions of the kinetic energy and the micro-scale Reynolds number, and indicates that a statistical steady state has been reached. As discussed above, figure 2.8 indicates the isotropy of the flow characterized by the micro-length-scale feature $\lambda_{f,i}/\lambda_{g,jk} = \sqrt{2},\ (j \neq k)$ (Pope [87]).

For rotating turbulence we performed a series of simulations B and C, with case names, parameters and final Rossby numbers given in table 5.1. As mentioned, a

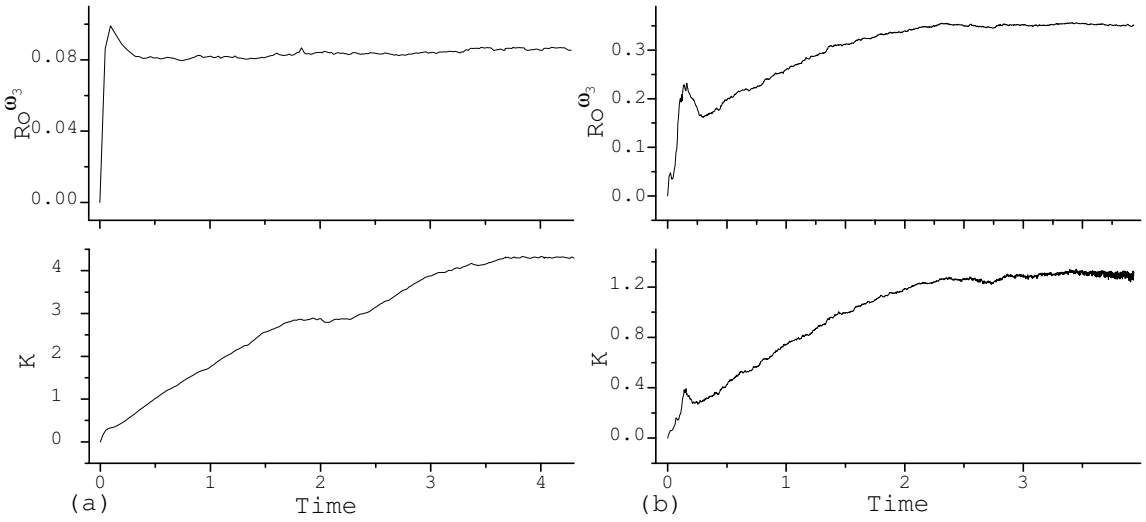


Figure 5.3: Evolutions of kinetic energy and $Ro^{\omega_3}$: (a) small scale forced rotating case B5; (b) large scale forced rotating case C3.

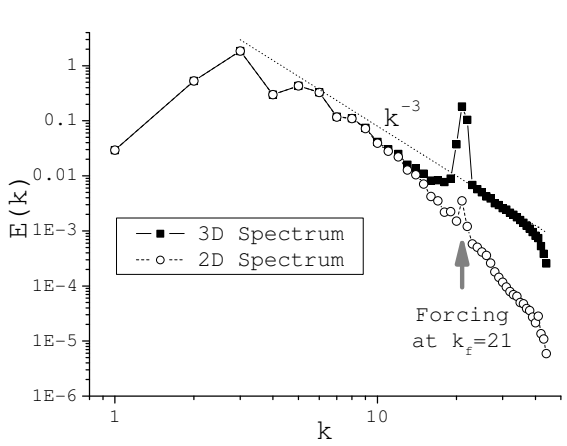


Figure 5.4: Kinetic energy spectrum of statistically steady state of rotating turbulent case B5.

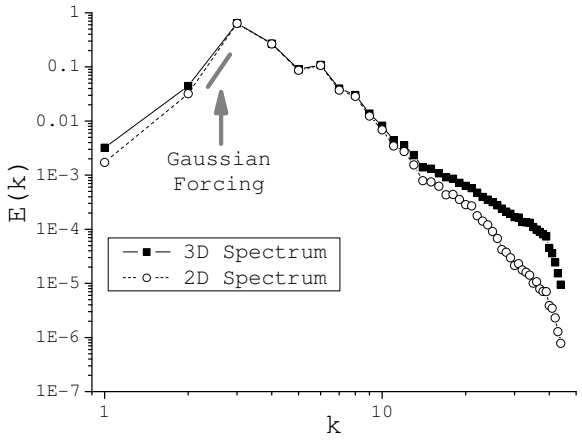


Figure 5.5: Kinetic energy spectrum of statistically steady state of rotating turbulent case C3.

Gaussian white-noise force is used for both series B and C, with the peak wave number of the force as the main difference between the two sets of runs: series B has small scale

Table 5.1: Description of forced rotating runs

| **Case** | $k_f$ | $\Omega$ $[rad/s]$ | viscosity | $Ro^G$ | $Ro^{\omega_3}$ |
|---|---|---|---|---|---|
| B1 | 11 | 10 | hyper only | 0.25 | 0.38 |
| B2 | 11 | 50 | hyper only | 0.049 | 0.094 |
| B3 | 21 | 10 | hyper only | 0.38 | 0.38 |
| B4 | 21 | 50 | hyper only | 0.076 | 0.082 |
| B5 | 21 | 50 | hyper+hypo | 0.076 | 0.086 |
| C1 | 2.5 | 2 | hyper+hypo | 0.46 | 0.50 |
| C2 | 2.5 | 4 | hyper+hypo | 0.23 | 0.31 |
| C3 | 2.5 | 6 | hyper+hypo | 0.15 | 0.35 |
| C4 | 2.5 | 8 | hyper+hypo | 0.12 | 0.24 |
| D | 2.5 | 8 | real-viscosity | 0.12 | 0.13 |

forcing with peak wave number $k_f = 11$ or $k_f = 21$, and series C has large scale forcing with peak wave number $k_f = 2.5$. Runs B1-B4 are time developing without large scale damping, and are terminated before energy accumulates in box-size vortices corresponding to population of modes with $k = 1$. Note that energy is growing in those runs and only scales smaller than the forcing scale are in a statistically steady state. Case B5 and C series run have hypo-viscosity to remove box-size vortices, and would eventually reach a statistically steady state at all scales. For all B and C series runs, the rotation rate was carefully selected to achieve moderately small values of the Rossby numbers $Ro^G$ and $Ro^{\omega_3}$ (see section 2.3.1).

Figures 5.4 and 5.5 show spectra from case B5 and case C3. Both figures show that energy in the large scales is predominantly in two-dimensional modes, while energy at small scales is increasingly three-dimensional. The physical space pictures corresponding to the spectra of figures 5.4 and 5.5 are shown in figure 2.5, with quasi two-dimensional cyclonic vortical columns in both cases. Similar coherent structures and *a-priori* test results were obtained in all cases. We present *a-priori* test results for case B5 to illustrate the model performance, and results for case C3 are presented in section 5.5. In addition, we performed a $256^3$ real-viscosity rotating case D to confirm our conclusions. Case D will be described in detail in section 5.5.2.

## 5.2 Eddy viscosity models

Eddy viscosity models are low-correlation models. It has been well established that the strain rate tensor has a low correlation level ($\rho < 0.4$) with stress components (Clark et al. [25], Bardina et al. [2], Liu et al. [64], and Menon et al. [72]). Similar results are obtained in our DNS cases and summarized below.

Figures 5.6 and 5.7 show correlation coefficients for SGS models in isotropic turbulence and rotating turbulence as a function of the LES filtering cut-off wave number, since there is no clear definition of the Kolmogorov scale for rotating flow. Results for the SSM are provided as a reference for comparison because it is known to be a relatively high-correlation model. All components of the SGS stress tensor and its divergence were examined but only representative components are presented.

For isotropic turbulence, the SM gives a low correlation level ($\sim 0.2$) for stress components ($\tau_{ij}$), a slightly better correlation ($\sim 0.35$) for the vector components of the divergence ($\partial\tau_{ij}/\partial x_j$), and a better correlation ($0.5 \sim 0.8$) for the production

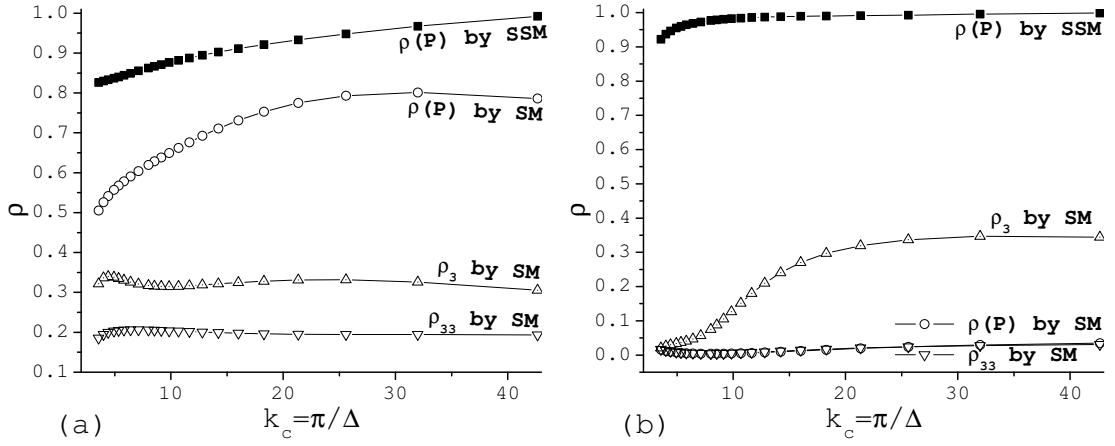


Figure 5.6: Correlation coefficient for the SM:(a) isotropic case A; (b) rotating case B5.

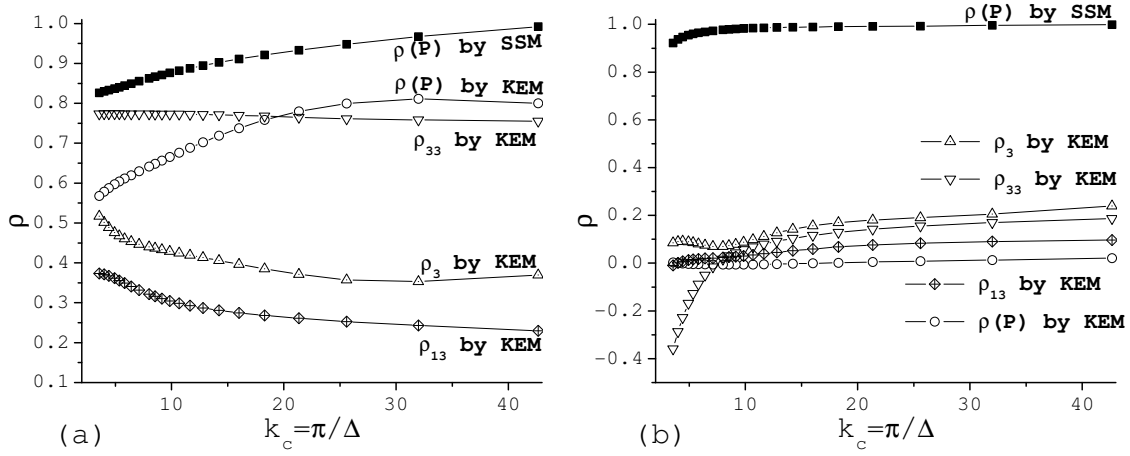


Figure 5.7: Correlation coefficient for the KEM: (a) isotropic case A; (b) rotating case B5.

term. These results are consistent with the findings of Clark et al. [25], Liu et al. [64], Menon et al. [72] and others. For rotating turbulence, the SM gives very low correlation coefficients ($0 \sim 0.03$) for stress components, higher correlations ($0.02 \sim 0.2$) for vector components of the divergence, and very low correlations ($0 \sim 0.03$) for the production term.

For isotropic turbulence, the KEM gives very good correlation coefficients ($\sim$ 0.8) for stress components ($\tau_{ij},\ _{i=j}$), but a low correlation level ($\sim 0.3$) on cross terms ($\tau_{ij},\ _{i\neq j}$). These outcomes are reasonable because the magnitude of the diagonal terms is dominated by the SGS kinetic energy while the cross terms are determined by the strain rate tensor. The correlation level of the components of the divergence is between 0.3 and 0.5, and the correlation level of the energy production term is between 0.5 and 0.8. These results are consistent with the findings of Menon et al. [72]. For rotating turbulence, the KEM gives a low correlation coefficient ($\rho < 0.2$) for any stress component involving the rotation direction ($\tau_{3j},\ _{j=1,2,3}$), for all components of the divergence, and for the energy production term. Significantly, it gives a negative $\rho_{33}$ for very large filter sizes.

## 5.3 MFI-consistent models

Models that are MFI-consistent with the actual SGS stress are expected to do much better in rotating systems. These models have high correlation and regression coefficients and improved ability to capture the anisotropy of rotating turbulent flows.

### 5.3.1 Correlation of SGS models

Models based on the scale-similarity procedure or a Taylor expansion usually give high correlation coefficients in *a-priori* tests. As mentioned in section 3.2, this study develops two new models based on these two procedures. As a consequence, these new models are able to capture the resolved flow structure much better than eddy viscosity models.

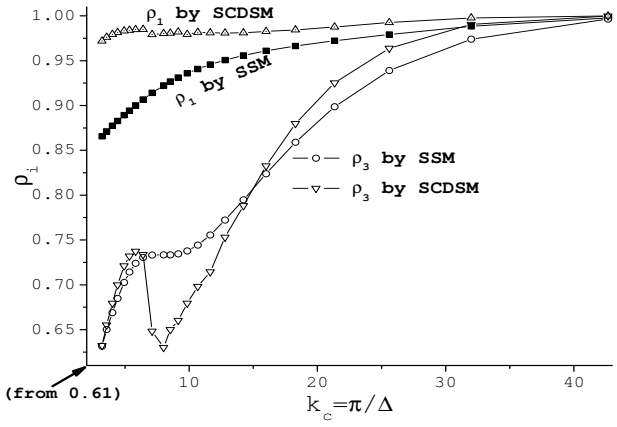


Figure 5.8: Correlation coefficient for rotating case B5.

Focusing on the SCDSM results, figure 5.8 shows the correlation coefficient $\rho_i$ in rotating turbulence case B5. Even though the correlation of the divergence component in the z-direction decreases more rapidly than the other components, all three correlations for the vector components are greater than 0.6 over a wide range of filter sizes. Similar results are obtained for tensor correlation coefficients; only $\rho_{33}$ dip below 0.6 when $k_c < 10$ in some rotating turbulent cases.

### 5.3.2 Influence of anisotropy

Section 3.2 showed that SSM is inconsistent with MFI at the stress tensor level. Here, we use *a-priori* test results to illustrate its failure to capture anisotropy. We chose the SSM as an example because it is a widely used zero-equation SGS stress model. Results of the SCDSM are used to show that MFI-consistent models are better able to capture anisotropy.

According to the definition of the SSM (2.33), all six modeled stress components use the same similarity coefficient, $C_L$. This coefficient has no influence on

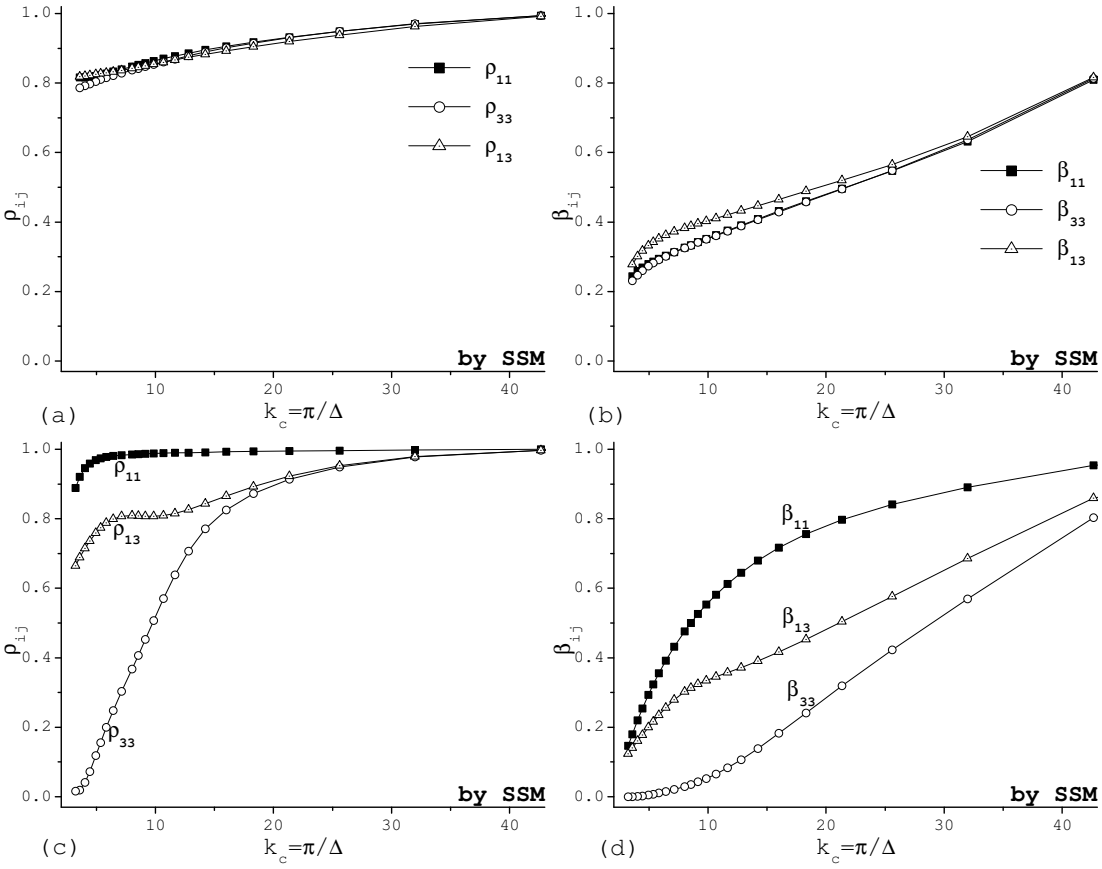


Figure 5.9: Correlation and regression coefficients: (a) $\rho(\tau_{ij}, \tau_{ij}^{SSM})$ and (b) $\beta(\tau_{ij}, \tau_{ij}^{SSM})$ in isotropic case A; (c) $\rho(\tau_{ij}, \tau_{ij}^{SSM})$ and (d) $\beta(\tau_{ij}, \tau_{ij}^{SSM})$ in rotating case B5

correlation but does change regression coefficients. The coefficient $C_L = 1$ is used, so the regressions are equal to one for very small filter sizes.

Figure 5.9 shows the correlation and regression coefficients of stress components in isotropic case A and in rotating turbulent case B5. Regardless of the flow type, the correlation and the regression coefficients decrease when the filter size increases

($k_c$ decreases). These results show that the SSM becomes quite poor as the gird is coarsened.

As shown in figures 5.9(a) and (b), for isotropic turbulence, because of isotropy, the six correlation coefficients of stress components decrease similarly, and the six regression coefficients of stress components decrease similarly.

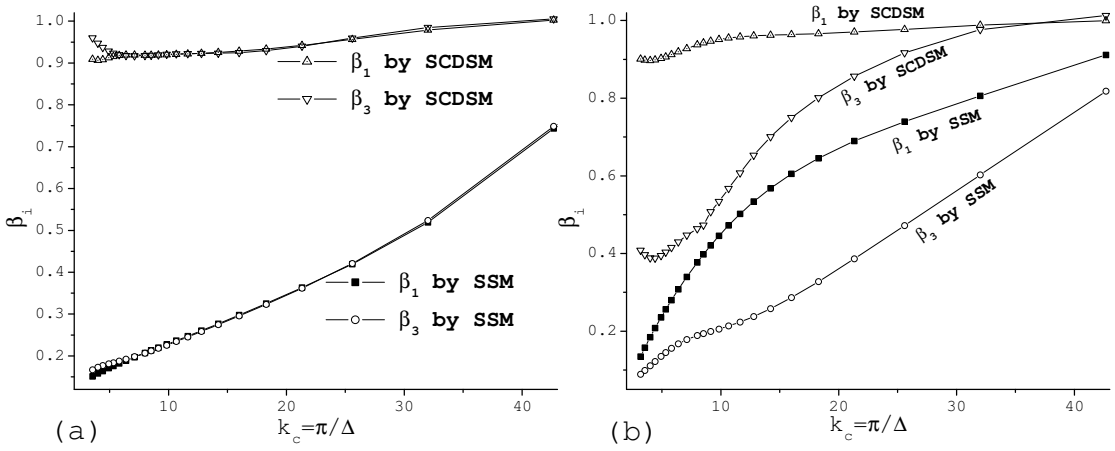


Figure 5.10: Regression coefficient: (a) isotropic case A; (b) rotating case B5.

For rotating turbulence, the SSM correlation and regression coefficients that correspond to the rotating direction components decrease much more rapidly with filter size than the other coefficients, as shown in figures 5.9(c) and (d). This difference between the isotropic turbulence and the anisotropic turbulence lies in the length scales. Section 2.3.2 has shown that rotating turbulence does not have an identical scale in all directions. Generally, $\lambda_{f,3}$ is smaller than $\lambda_{f,1}$ and $\lambda_{f,2}$. When isotropic filters are used, the normalized length scale $\Delta/\lambda_f$ in the z direction is larger, and the turbulence details in the z-direction are more highly filtered. In a sense, a relatively coarser grid has been employed in the z-direction. As a consequence, the correlation

and the regression coefficients associated with the z-direction components are smaller than for the other directions.

In contrast, the MFI-consistent SCDSM shows much better results than the SSM. Figure 5.10 shows the regression coefficients of vector components in case A and case B5 for the two models. For isotropic turbulence, the SCDSM gives nearly perfect regressions in all directions for all filter sizes, while the SSM shows very poor regression coefficients. For rotating turbulence, anisotropy effects make the regressions in the z-direction decrease more rapidly. However, the SCDSM regression coefficients remain greater than 0.8 in all directions for smaller filter sizes ($k_c \geqslant 20$). In contrast the SSM only gives $\beta_3 \approx 0.35$ when $k_c = 20$.

### 5.3.3 Regression of SGS models

For isotropic turbulence, figures 5.9(b) and 5.10(a) show that the regression coefficient of the SSM decreases rapidly to values less than 0.35 when $k_c$ decreases to 20. To improve the regression coefficient, at least two methods have been used. One method uses SGS kinetic energy to determine the similarity coefficient in zero-equation scale similarity models (Cook [26]). This approach, however, has to use kinetic energy spectra in Fourier space, which may be not applicable to most engineering applications. In the method adopted herein, called the Dynamic Structure approach, one-equation models use SGS kinetic energy to predict the magnitude of the modeled SGS stresses, and use normalized tensor terms to determine the SGS stress structure (Pomraning & Rutland [85, 86]). For example in SCDSM, $\tau_{ij} \approx 2k_{sgs}\left(\frac{\Upsilon_{ij}^M}{\Upsilon_{mm}^M}\right)$. The SCDSM gives very high regression coefficients, $\beta > 0.9$, over all filter sizes in all directions (figure 5.10(a)). The other dynamic structure models, GCDSM and DSM,

have similar results. This suggests that such models may be applicable for LES of high Reynolds number isotropic turbulence using relatively coarse grids.

For rotating turbulence, as shown in the previous section (figures 5.9(d) and 5.10(b)), the correlation and the regression coefficients in the z-direction decrease much more rapidly with filter size than the other coefficients. Hence, to show the benefits of the new models, we compare the stress in the z direction ($\tau_{33}$) and the vector component in the z-direction ($\partial\tau_{3j}/\partial x_j$).

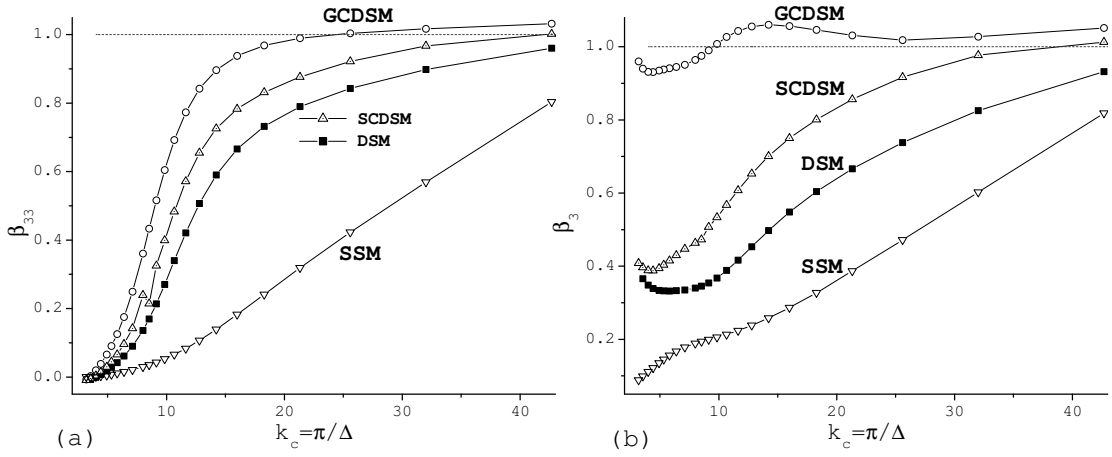


Figure 5.11: Regression coefficient for rotating case B5: (a) $\beta_{33}$ and (b) $\beta_3$.

Figure 5.11 shows z-direction regression coefficients for the new models. When compared to the SSM, three dynamic structure models have significantly higher regression coefficients in isotropic turbulence and noticeably better results in rotating turbulence. This is primarily due to the use of SGS kinetic energy to determine the magnitude of the SGS stresses.

In rotating turbulence, the two MFI-consistent models (GCDSM and SCDSM) show better results than the basic dynamic structure model (DSM). Maintaining

material frame indifference in the model, either inherently or by construction, helps to diminish the problems of anisotropy that occur in rotating systems. Figure 5.11 shows that the GCDSM gives some of the best results. For rotating turbulence, the GCDSM regression coefficient remains near one for all filter sizes. It gives $\beta > 0.8$ when $k_c > 13$ for $\tau_{33}$, $\beta \approx 1$ for other stress terms, and nearly unit regression for vector components even when the grid is very coarse. Note that at small filter sizes, the GCDSM does not approach the actual SGS stresses because the model is based on the first term in a Taylor series. This shortcoming is probably not significant in applications where coarser than DNS grids are used, especially given the excellent results of this model.

All of the results presented here use the Gaussian filter in a discrete manner in physical space. We have explored the cut-off, the top-hat and the triangle filter (Pope [87], Piomelli et al. [83], and Pomraning & Rutland [85]). The results for these filters are essentially the same as for the Gaussian filter. The primary difference was found with the cut-off filter which introduces additional physical space oscillations and can result in lower correlation coefficients. This is consistent with the results of Liu et al. [64].

## 5.4 Energy production at subgrid scales

Kinetic energy transfer between resolved and subgrid scales occurs through the production term (also called energy flux) that appears in the SGS kinetic energy equation. The term is defined as

$$P = -\tau_{ij}\overline{S}_{ij} = -\tau_{ij}\frac{\partial \overline{u}_i}{\partial x_j} \ , \tag{5.1}$$

and is useful for comparing various SGS stress models as shown in figures 5.12, 5.13 and 5.14.

For isotropic case A, figure 5.12(a) shows that two eddy viscosity models (SM and KEM) give correlations values of about 0.75 over a wide filter size range. This is a reasonably good correlation and illustrates why these models can predict global dissipation fairly accurately. For rotating case B5, however, the eddy viscosity models give correlations values of less than 0.05 (figure 5.12(b)). This indicates that in rotating systems these models will have trouble predicting even the total, global energy dissipation. High correlation coefficients (above 0.8) can be obtained with other models in both cases. Figure 5.12 includes correlation results of the GCDSM and the SCDSM. Similarity type models (e.g., the SSM, the DSM and the SCDSM) have very similar correlation results; correlation values of gradient type models (e.g., the GM and the GCDSM) are also in very good agreement.

Examining the regression coefficient (figure 5.13) shows that the Dynamic Structure models (e.g., the GCDSM and the SCDSM) have much better results than the zero-equation high-correlation models (e.g., the SSM and the GM). The SSM and the GM significantly under-estimate the magnitude of energy production at larger filter sizes. This under-estimation of energy transfer is consistent with these models having more problems with stability when modeling high Reynolds number turbulence (Bardina [2, 3]).

Figure 5.14 shows the power spectra of the energy transfer term at a given filter size for rotating case B5. The SM is re-calculated by $\left(\frac{\tau_{kk}}{3}\delta_{ij} - 2\nu_t\overline{S}_{ij}\right)$ to perform this comparison. Most of the models show spectra that monotonically increase from large to small scales, similar to the DNS spectra. The SSM and the GM show slightly

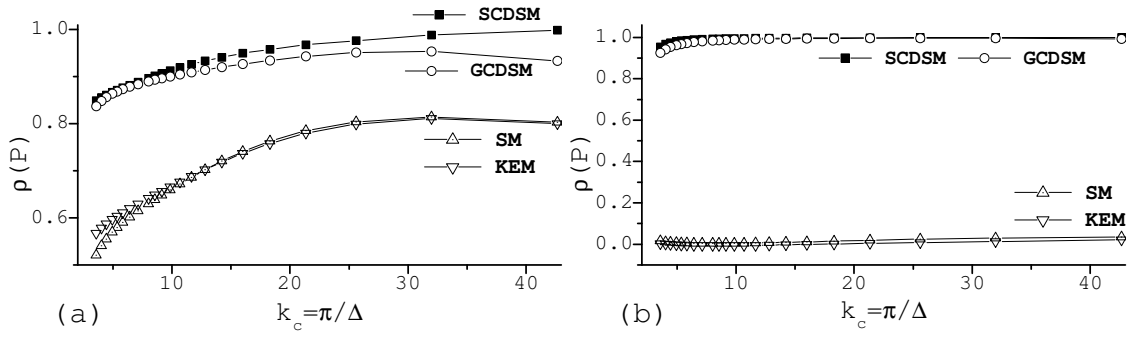


Figure 5.12: Correlation coefficients of production: (a) isotropic case A; (b) rotating case B5.

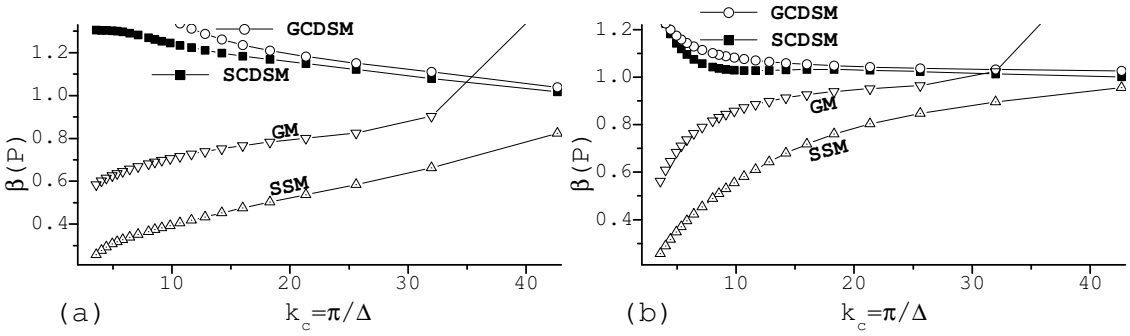


Figure 5.13: Regression coefficients of production: (a) isotropic case A; (b) rotating case B5.

lower values and the Dynamic Structure models show values close to or slightly higher than the DNS results, all consistent with figure 5.13 showing $\beta \approx 1$. However, figure 5.14 reveals significant inaccuracies in both the SM and the KEM. The SM is too dissipative at all scales, and the KEM spectrum has the opposite tendency from the DNS spectrum.

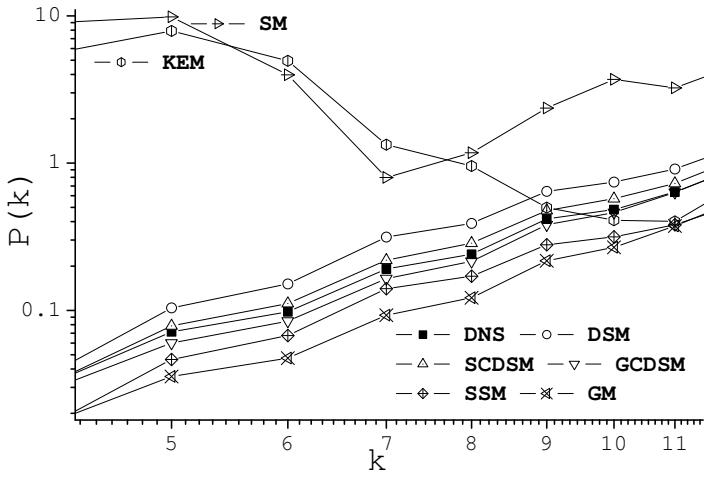


Figure 5.14: Power spectra of production for rotating case B5 (Gaussian filter at $k_c = 11$).

## 5.5 *A-priori* tests of other rotating cases

Although the *a-priori* analysis was carried out on all the DNS data sets, only case B5 was discussed above. Here, we present other examples to demonstrate the consistency of the conclusions.

### 5.5.1 Tests of another $128^3$ hyper-viscosity rotating case

In case B5, we input energy using the Gaussian white-noise forcing scheme at small scales ($k_f = 21$). In case C3, we input energy using the same scheme at large scales ($k_f = 2.5$). The hypo- and hyper-viscosities were used in both computations to produce a reasonable inertial range and stationary results. More importantly, case B5 and case C3 have some differences in the underlying physical processes (figures 5.3, 5.4, 5.5, and 2.5). For example, in case B5, the reverse energy transfer from small to large scales is the only energy source for the flow at large scales. The 3D & 2D

spectrum plots 5.4 and 5.5 show that the flow at large scales is more two-dimensional when forced at small scales than when forced at large scales.

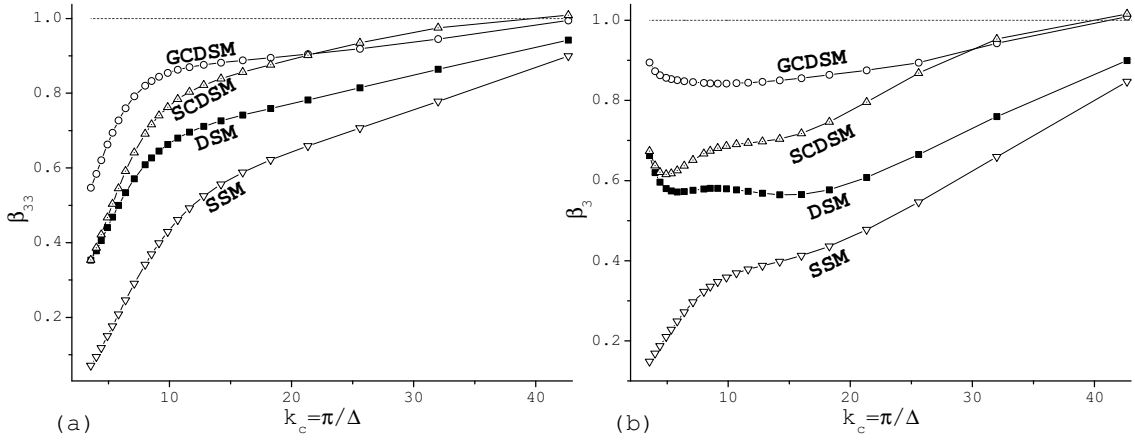


Figure 5.15: Regression coefficients for large scale forced rotating case C3: (a) $\beta_{33}$ and (b) $\beta_3$

However, case B5 and case C3 have the similar regression coefficient results in two ways: (i) there exists an overall tendency that the regression coefficient decreases when the filter size increases, and also the z-direction regression coefficients decrease more rapidly (not plotted here); (ii) as shown in figures 5.15 and 5.11, the two MFI-consistent one-equation models (GCDSM and SCDSM) have higher regression coefficients than the others, and the GCDSM has some of the best results. We have consistent conclusions for energy production term which are not plotted here.

### 5.5.2 A $256^3$ real-viscosity rotating case

We have performed *a-priori* tests of a $256^3$ real-viscosity rotating turbulent case D, which reached a quasi-steady state with $Re_\lambda = 180$. Figure 5.16 shows the 3D &

2D kinetic energy spectra of this case. In order to compare with the results of the $128^3$ large scale forced hyper-viscosity runs (C series), we have chosen the same Gaussian forcing peak wave number $k_f = 2.5$, and have matched Rossby number $Ro^G = 0.12$.

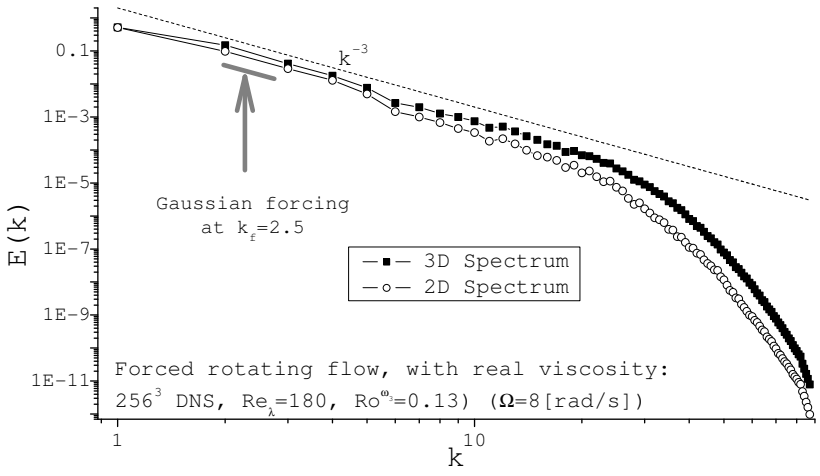


Figure 5.16: Kinetic energy spectrum of a $256^3$ large scale forced real-viscosity rotating turbulent case D.

The $256^3$ case allows us to do correlation-regression studies up to $k_c = 85$. Figure 5.17 compares the regressions for $128^3$ hyper-viscosity rotating case C3 and $256^3$ real-viscosity rotating case D. There is a clear overall tendency for the regression coefficient to decrease as the filter size increases. Figure 5.17 shows that dynamic structure models (DSM, GCDSM and SCDSM) have an advantage over the SSM in more accurately modeling SGS stress; the GCDSM and the SCDSM also show promise of higher regressions than other models.

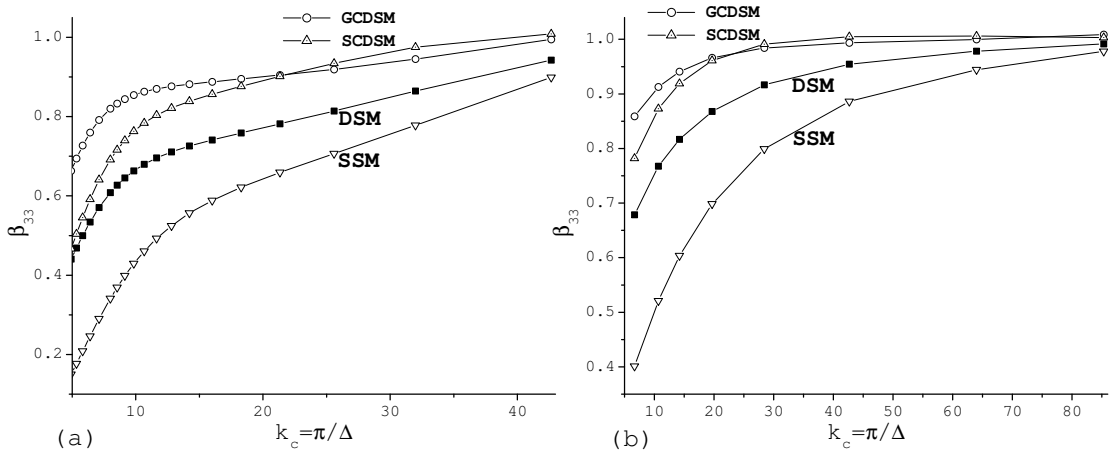


Figure 5.17: Regression coefficients for $\tau_{33}$: (a) in $128^3$ large scale forced hyper-viscosity rotating case C3, and (b) in $256^3$ large scale forced real-viscosity rotating case D.

## 5.6 *A-priori* tests using joint PDF

The structure of SGS stress, $\tau_{ij}$, is also of interest in LES modeling. Recently, Chumakov [22] introduced two parameters, $s^*$ and $q^*$, to characterize the state of SGS stress. If we denote the eigenvalues of SGS stress by $\alpha$, $\beta$, and $\gamma$, in the order $\alpha > \beta > \gamma$, these two parameters are defined as

$$s^* = -cos3\theta \ , \ q^* = \frac{1}{6\pi}(12\phi + 8sin2\phi + sin4\phi) \ , \tag{5.2}$$

with the angles $\theta$ and $\phi$ given by

$$cos\theta = \frac{3\tilde{\alpha}}{\sqrt{6}(\tilde{\alpha}^2 + \tilde{\beta}^2 + \tilde{\gamma}^2)^{1/2}} \ , \ sin\phi = \frac{\alpha + \beta + \gamma}{\sqrt{3}(\alpha^2 + \beta^2 + \gamma^2)^{1/2}} \ , \tag{5.3}$$

where $\tilde{\alpha} = \alpha - \tau_{ii}/3$, $\tilde{\beta} = \beta - \tau_{ii}/3$, and $\tilde{\gamma} = \gamma - \tau_{ii}/3$. $s^*$ describes the anisotropy of SGS stress. If $s^* \approx -1$, SGS stress is highly anisotropic, namely, the two eigenvalues

of $\tau_{ij}$ are much smaller than the third, which corresponds to two smooth and one strongly fluctuating velocity component. $q^* = 0$ indicates $\tau_{ii} = 0$. Some advocate using the pair ($s^*$, $q^*$) instead of just $s^*$ to fully characterize the state of $\tau_{ij}$, since $\tau_{ij}$ is rarely traceless.

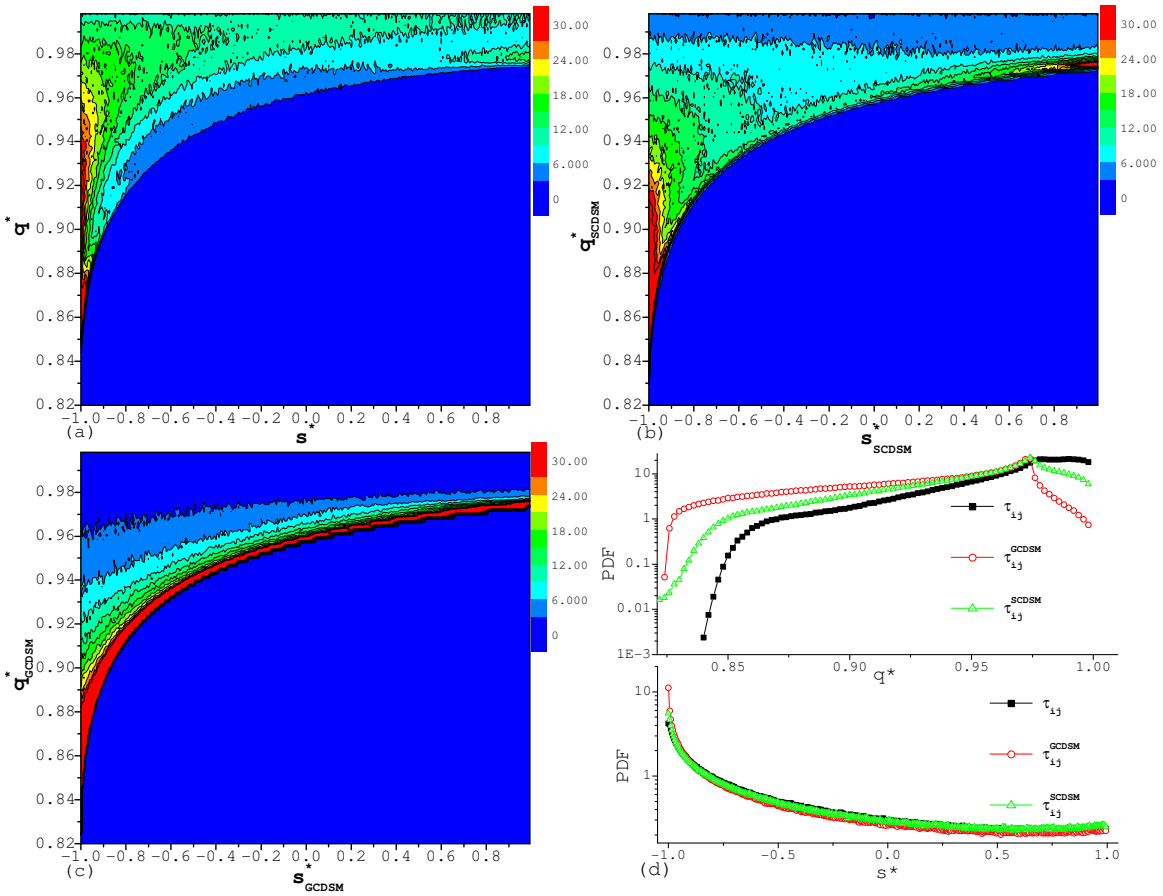


Figure 5.18: Assessment of SGS models using $s^*$ and $q^*$ (rotating case B5). A Gaussian filter function with $k_c = 20$ is used. (a) Contour plot of joint PDF of ($s^*$, $q^*$); (b) contour plot of joint PDF of ($s^*$, $q^*$) obtained from the SCDSM; (c) contour plot of joint PDF of ($s^*$, $q^*$) obtained from the GCDSM; (d) PDF of $s^*$ and $p^*$ computed by the SGS stress and two models: the GCDSM and the SCDSM.

Figures 5.18(a)-5.18(c) show contour plots of joint PDF of ($s^*$, $q^*$) calculated using actual SGS stress and using the two new models (GCDSM and SCDSM). Figure 5.18(d) shows PDF of $s^*$ and $p^*$ using actual SGS stress and using the two new models. These plots reveal that rotating turbulence has high degree of the SGS stress anisotropic. Also, the SCDSM, which is based on the scale-similarity assumption, predicts a distribution of states that is closer to actual. However, the GCDSM, which is based on a truncated Taylor series, does not produce an adequate distribution of states. This conclusion is consistent with findings on isotropic turbulence (Chumakov [22]).

## 5.7 Summary

The evaluation of model performance in this comparative study of various SGS models is summarized in table 5.2. The models are listed with symbols to indicate if they performed poorly, well, or very well on each diagnostic.

As mentioned in section 2.2.2.4, the viscosity term in the mixed approach does not degrade the *a-priori* results. Typically the magnitude of the structure term is significantly higher than that of the viscosity term ($\gtrapprox$ 50 times when measured in the $L_2$-norm). Also in comparison with the scatter distribution for the structure term (such as the similarity term shown in figure 4.3), the viscosity term is much more isotropically distributed. As a consequence, the viscosity term gives much lower correlation. At the *a-priori* level, the mixed versions derived from the SSM, the GM, the DSM, the SCDSM and the GCDSM have delivered results identical to the original unmixed versions.

Table 5.2: Comparison of model performance in the LES of rotating turbulence at the *a-priori* test level

| **Diagnostic** | SM | KEM | SSM | GM | DSM | SCDSM | GCDSM |
|---|---|---|---|---|---|---|---|
| $\rho_{ij}$ | $-$ | $*$ | $+$ | $+$ | $+$ | $+$ | $+$ |
| $\beta_{ij}, (i,j \neq 3)$ | $-$ | $*$ | $+$ | $+$ | $+$ | $++$ | $++$ |
| $\beta_{3j}$ | $-$ | $-$ | $-$ | $-$ | $-$ | $+$ | $++$ |
| $\rho_i$ | $-$ | $-$ | $+$ | $+$ | $+$ | $+$ | $+$ |
| $\beta_i, (i \neq 3)$ | $-$ | $-$ | $+$ | $+$ | $+$ | $++$ | $++$ |
| $\beta_3$ | $-$ | $-$ | $-$ | $+$ | $-$ | $+$ | $++$ |
| $\rho(P)$ | $-$ | $-$ | $+$ | $+$ | $+$ | $+$ | $+$ |
| $\beta(P)$ | $-$ | $-$ | $-$ | $-$ | $+$ | $++$ | $++$ |
| $PDF(s^*,\ q^*)$ | $-$ | $-$ | $-$ | $-$ | $+$ | $+$ | $-$ |

The symbols $-$, $+$ and $++$ refer to bad, good and very good results.

*Good on $\rho_{11}$, $\rho_{22}$, $\beta_{11}$ and $\beta_{22}$, but bad on cross terms, $\rho_{ij,(i\neq j)}$ and $\beta_{ij,(i\neq j)}$.

It is important to note that all rotating cases in the present study have the same Taylor micro-scale features as discussed in section 2.3.2. As discussed in sections 5.3.2 and 5.3.3, a large size filtering, which can be characterized by a normalized filter size (e.g., the ratio of filter size to micro-scale), compresses the small scale turbulence and lowers the correlation and the regression coefficients overall. Because $\lambda_{f,3}$ is smaller than $\lambda_{f,1}$ and $\lambda_{f,2}$, a relatively coarser filtering was employed in the z-direction. As a result, regression coefficients decrease much more rapidly in the z-direction, especially for traditional SGS models which assume that small scale turbulence is nearly

isotropic and do not account for rotational effects (e.g., the SSM and the DSM). MFI-consistency is a theoretical standpoint concerning turbulent constitutive relation for SGS stress in a non-inertial frame of reference undergoing rotation. This comparative study shows that the new MFI-consistent models can achieve considerably improved regression coefficient values in all directions.

In this study, DNS validation cases were performed at moderate Reynolds number for forced isotropic turbulence and moderate Rossby numbers for forced rotating turbulence. Details of the comparison may be valid only for these cases, but some studies are expected to be more generally applicable, such as the regression coefficient analysis, the invariance of SGS models and the influence of anisotropy on LES modeling. Nevertheless, there is still a need for *a-posteriori* testing of rotating turbulence.

# Chapter 6

# *A-posteriori* test

Certain risks exist if a systematic investigation of model performance in actual LES of turbulent flows is not performed. For instance, the SSM performs better than the SM at the *a-priori* level, but the SSM alone does not dissipate enough kinetic energy at small scales and typically leads to inaccurate results (Bardina [2]). Thus, researchers have added a viscosity term resulting in a mixed version (Bardina [2], Zang [116], Vreman et al. [106]), which has been proven a great success for many applications (Zang et al. [116], Vreman et al. [108], Kobayashi & Shimomura [54]). This shows an example that *a-posteriori* tests can play an important role in improving LES modeling.

Note that *a-posteriori* tests differ from engineering applications. *A-posteriori* tests usually use simple geometries, such as 3D rectangular boxes and concern only limited numbers of physical phenomena for a specific research purpose. There exist many physical complexities, such as external forces, rotation effects, wall frictions, chemical reactions, flow shearing, and multiple phases. *A-posteriori* tests usually exclude complexities not relevant to a given research focus.

Rather than focus on numerical methods, we systematically investigate and compare the characteristic behavior of a number of SGS models in an actual LES of rotating turbulent flows. Thus, we still used the pseudo-spectral method, and

the third order Runge-Kutta time marching scheme. We calculated the modeled SGS stress in physical space and transferred it into Fourier space as needed. We conducted two configurations of LES to assess SGS models. The LES results in the first configuration were compared with the filtered DNS results. To strengthen our understanding of the physical elements, we have concentrated on decaying turbulent flows without considering the effects of any external forcing. The simulations in the second configuration were performed at higher Reynolds numbers than in the first configuration. The rotating turbulent flows were forced at both intermediate scales and large scales. We judged the LES results according to the anisotropic level of the rotating turbulence including the cyclone structure, the kinetic energy transfer from small to large scales, and the quasi two-dimensional structure. The second configuration of simulations is a more rigorous assessment, because traditional models fail to capture these features of rotating turbulence.

Note that we used traditional parameter setups for SGS models as described in section 2.2.2. LES equations (2.23) were solved numerically on a mesh of spacing $h = 2\pi/max(nx, ny, nz)$, where $nx$, $ny$ and $nz$ are the point numbers in the x-, y- and z-directions. We treated $\Delta = 2h$ for six-order accuracy (Vreman et al. [108], Chow & Moin [21], Pope [88]). For simplicity, we use some abbreviated expressions below: " the large eddy simulation using the SM" is abbreviated as "the SM", and "the large eddy simulation using the SM at the resolution of $32^3$" is abbreviated as "the $32^3$ SM", etc.

## 6.1 Decaying turbulence

First, we applied models to decaying turbulent flows, including an isotropic turbulent case and two rotating turbulent cases. The initial Taylor micro-scale Reynolds numbers were about 85. Thus, the $128^3$ DNS could resolve all scales, and the DNS results could verify the accuracy of SGS models and identify their problems. We set the Courant-Friedrichs-Lewy (CFL) numbers for decaying flows at $\sim 0.15$.

### 6.1.1 Case description

Three cases with different setups were studied. Table 6.1 presents the initial state letters (I and R), the rotation rates, and the Rossby numbers at the initial times in cases E, F, and G.

State I is an isotropic turbulent state derived from case A. After case A reached its statistically steady state ($Re_\lambda = 100$), which we used in our *a-priori* tests, we turned off the forcing. The isotropic turbulent flow decayed over about two eddy turn-over times and reached state I. Figure 6.1 shows a three-dimensional kinetic energy spectrum of state I ($Re_\lambda = 85$); for convenience, a $-5/3$ power law is shown as a dotted line. State R is a rotating turbulent state. We used the Gaussian forcing to add energy at large scales ($k_f = 2.5$) to an initial very low energy isotropic random noise, and added rotation from the very beginning. Such problems have been studied extensively in the past in both experiments and numerical simulations (Lilly [62], Smith & Waleffe [97]). Then, we stopped the forced run at a statistically steady state to provide the initial state R. Figure 6.2 shows the three-dimensional and the two-dimensional kinetic energy spectra of state R.

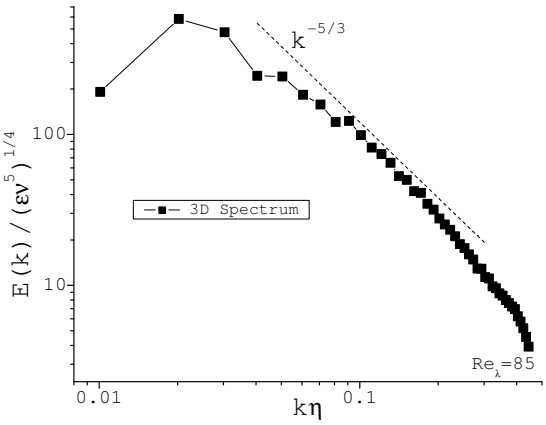


Figure 6.1: 3D kinetic energy spectrum of isotropic turbulent state I.

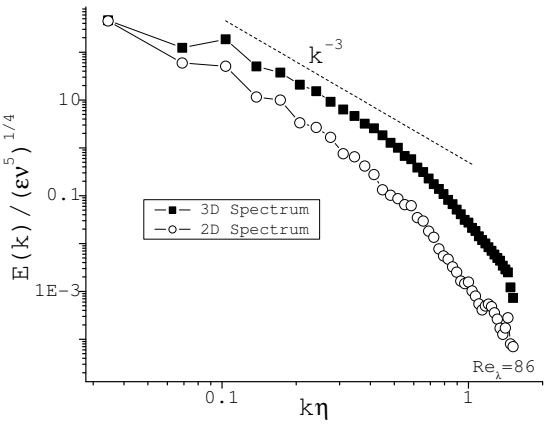


Figure 6.2: 3D & 2D kinetic energy spectra of rotating turbulent state R.

Table 6.1: Description of decaying cases

| **Case** | **Initial state** | $\Omega$ $[rad/s]$ | $Ro^{\omega_3}$ |
|---|---|---|---|
| E | I | 0 | $\infty$ |
| F | R | 1 | 0.41 |
| G | I | 20 | 0.17 |

Case E started from isotropic turbulent state I, and did not include the Coriolis force. Case F started from rotating turbulent state R, and retained the original rotation rate of 1 $[rad/s]$. We will focus the discussion of various SGS models in these two cases. In case G, isotropic turbulent state I was suddenly subjected to a rotation. Figure 2.3 shows the time-evolution of kinetic energy in decaying turbulent flows subject to different rotation rates. For our *a-posteriori* testing, we chose $\Omega =$

20 $[rad/s]$ and the initial $Ro^{\omega_3} = 0.17$ as a moderate Rossby number (Bartello et al. [7]).

At the *a-posteriori* test level, the "grid" level filter shape is never explicitly specified in a large eddy simulation. We assumed the Gaussian filtering at the "grid" level in order to obtain the filtered DNS results. Note that we filtered the $128^3$ DNS data (including initial conditions) with $k_c = 21$ to derive the $64^3$ LES data (including initial conditions) and with $k_c = 11$ to derive the $32^3$ LES data (including initial conditions). We normalized time using initial eddy turn-over time in subsequent discussions.

### 6.1.2 Performance of SM and SSM

In this section, we examine three simulations - the simulation without a model (which simply omits $\tau_{ij}$ in the simulation), the SM and the SSM. Figure 6.3 shows the evolution of the resolved kinetic energy integrated over the entire computational domain

$$K_r = \int \frac{1}{2} \overline{u}_i \overline{u}_i \, d\vec{x} \; . \tag{6.1}$$

The decaying cases start at the initial Reynolds number of about 85, which is exceedingly beyond the capability of $32^3$ simulation (typically $Re_\lambda \sim 30$, Pope [87]). Thus, the differences of $K_r$ between the DNS and the $32^3$ simulation without a model are significant. Specifically, the $32^3$ simulation without a model dissipates kinetic energy insufficiently. Figure 6.4 illustrates that kinetic energy at small scales is hardly dissipated. Together with the fact that a great amount of kinetic energy at large scales transfers into small scales (Lumley [68]), kinetic energy is accumulating at small scales that could eventually lead to an unstable simulation. The increase

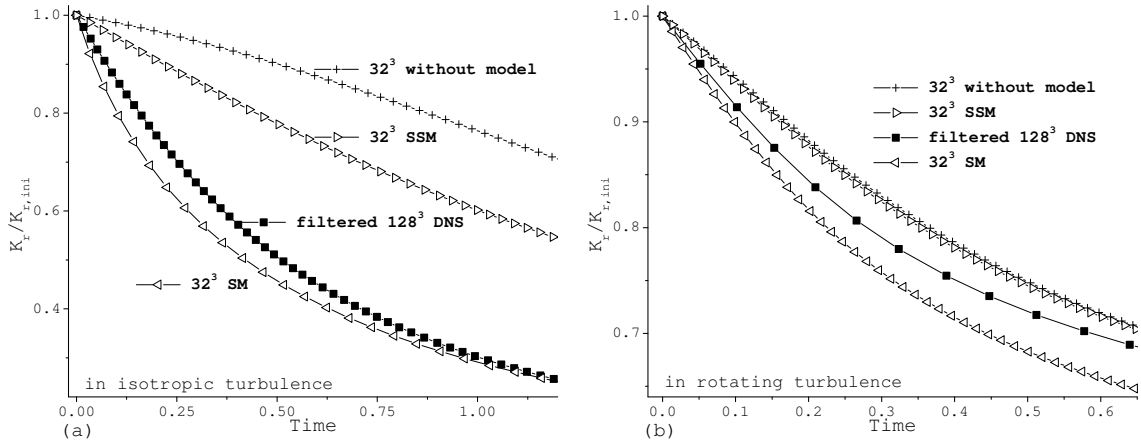


Figure 6.3: Evolution of resolved kinetic energy obtained from the filtered $128^3$ DNS, the $32^3$ simulation without model, the $32^3$ SM and the $32^3$ SSM: (a) in isotropic turbulent case E; (b) in rotating case F.

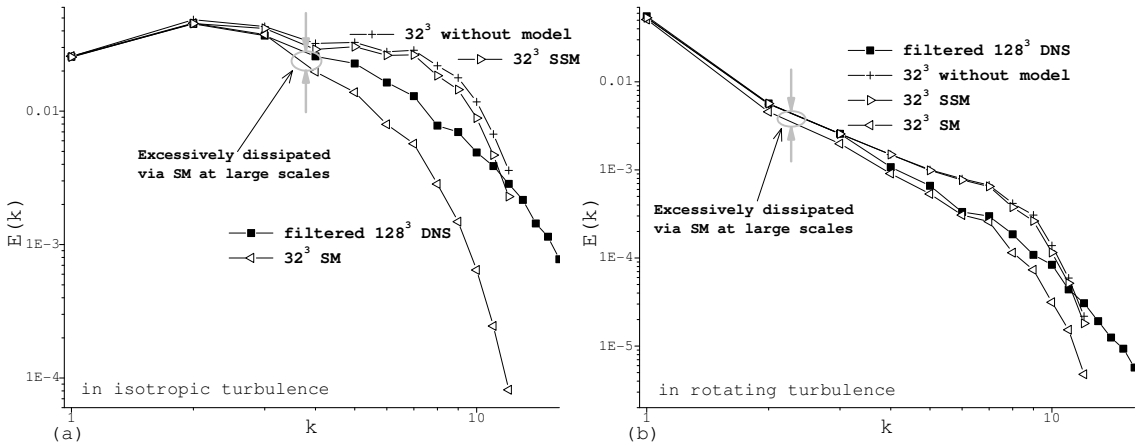


Figure 6.4: 3D kinetic energy spectrum obtained from the filtered $128^3$ DNS, the $32^3$ simulation without a model, the $32^3$ SM and the $32^3$ SSM: (a) in isotropic turbulence case E at $time = 0.4$; (b) in rotating case F at $time = 0.7$.

of grid resolution from $32^3$ (Fig. 6.3) to $64^3$ (Fig. 6.5) facilitates the prediction of the kinetic energy decay. However, for isotropic case E, the $64^3$ simulation without a model still yields a lower kinetic energy decay rate. In order to obtain proper kinetic energy decay rates, turbulence modeling is undoubtedly needed for coarser grids.

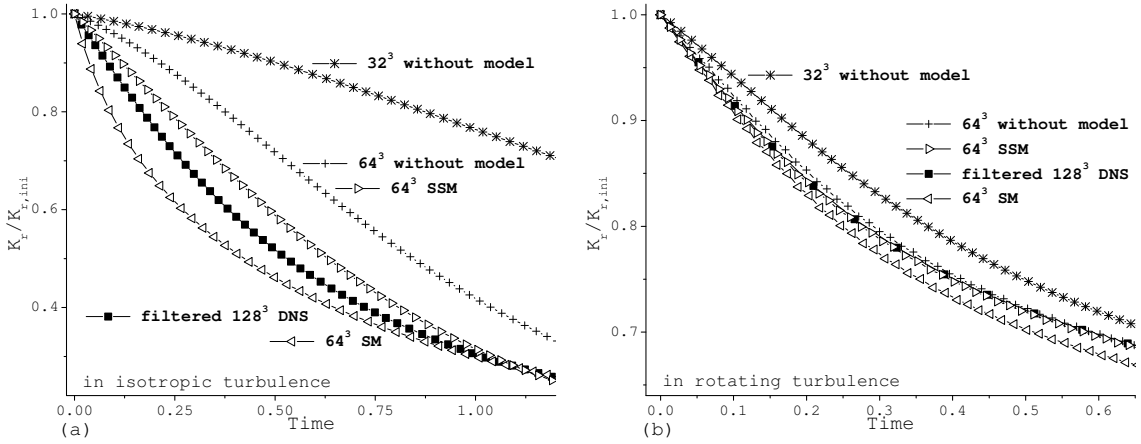


Figure 6.5: Evolution of resolved kinetic energy obtained from the filtered $128^3$ DNS, the $64^3$ simulation without a model, the $64^3$ SM and the $64^3$ SSM (the $32^3$ simulation without a model functions as a comparison reference): (a) in isotropic turbulent case E; (b) in rotating case F.

Studies have explored that the SM yields excessive dissipation for many turbulent flows, such as turbulent channel flows (Piomelli et al. [84]) and turbulent mixing layers (Vreman et al. [108]). This proposition is also true for current decaying cases. Figures 6.3 and 6.5 illustrate that the SM gives higher kinetic energy decay rates in comparison with the filtered DNS results. Figure 6.4 shows that the SM dissipates kinetic energy over all length scales excessively. Since in LES modeling the large scale

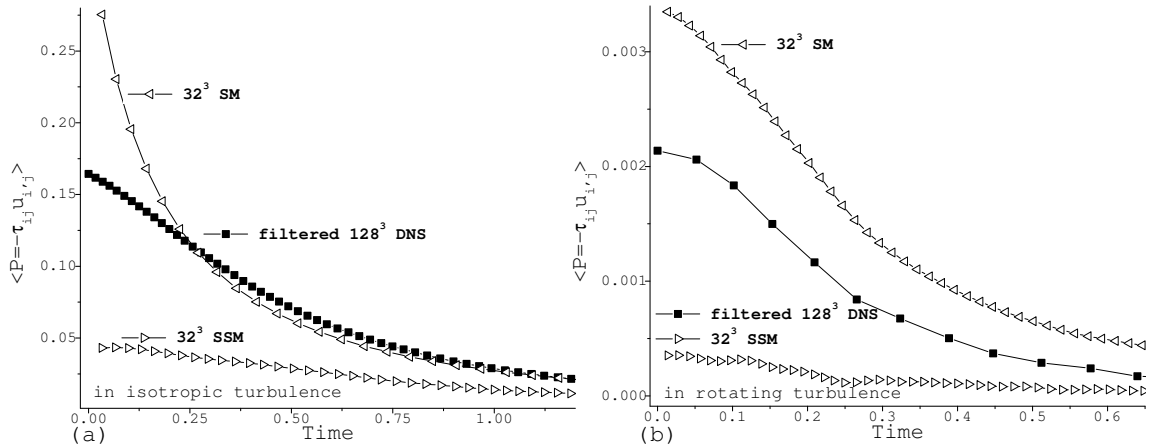


Figure 6.6: Evolution of SGS energy production obtained from the filtered $128^3$ DNS, the $32^3$ SM and the $32^3$ SSM: (a) in isotropic turbulent case E; (b) in rotating case F.

flows are solved explicitly, excessive dissipation at large scales may be considered as an improper behavior.

The decay of the resolved kinetic energy in incompressible flow is described by the following equation

$$\frac{DK_r}{Dt} = \int P(\vec{x})\, d\vec{x} - \int \varepsilon_r(\vec{x})\, d\vec{x}\ , \tag{6.2}$$

where molecular dissipation $\varepsilon_r = \nu \frac{\partial \overline{u}_i}{\partial x_j} \frac{\partial \overline{u}_i}{\partial x_j}$, and SGS energy production (sometimes referred to as "energy flux") $P = \tau_{ij} \frac{\partial \overline{u}_i}{\partial x_j}$. SGS energy production represents the kinetic energy transfer from resolved scales to subgrid scales, and is regarded as the kinetic energy source at subgrid scales. The rotational term will not explicitly appear in this equation, since analytically $(\vec{\Omega} \times \vec{\overline{u}}) \cdot \vec{\overline{u}} = 0$. The molecular dissipation is always positive. However, we have observed that the magnitude (e.g., $L_2$ norm) of the molecular dissipation is much less (10 times) than the magnitude of the SGS

energy production for a long period of time. Because current decaying cases initially hold high Reynolds numbers, which indicates that a major part of kinetic energy transfers first to subgrid scales and then to internal energy. Thus, we will mainly focus on the SGS energy production to compare model performances.

Figure 6.6 shows the SGS energy production evolution obtained from the filtered DNS, the SSM and the SM. The simulation without a model has no SGS energy production, since no SGS model is adopted. The SM clearly yields higher SGS energy production over a long period of time. Consistent with figures 6.3 and 6.5, this indicates that too much kinetic energy is transferred to subgrid scales using the SM.

The GM and the SSM resolve many weaknesses of the SM: for instance, they allow for "backscatter" and yield high correlations ($\rho > 0.6$) with the SGS stress over a wide range of filter sizes (Liu et al. [64]). At the *a-posteriori* level, the performances of these two models are also very similar. Thus, here we strive for simplicity by illustrating only the SSM results. Figure 6.3 shows that, over a long period of time, the SSM yields lower kinetic energy decay rates in both isotropic case E and rotating case F. It is consistent with findings that the SSM dissipates kinetic energy insufficiently and appears to be unstable (Bardina [2, 3]). For rotating case F, the SSM performs as poorly as the simulations without a model. Kinetic energy at small scales is accumulating and cannot be dissipated effectively as shown in figure 6.4. The primary cause of that is that the SSM yielded much lower SGS energy production (Fig. 6.6). So, there is an insufficient transfer of kinetic energy to subgrid scales using the SSM. Additionally, if the grid resolution is increased from $32^3$ (Fig. 6.3) to $64^3$ (Fig. 6.5), the SSM provides much better results at higher resolution. The resolution dependence is a serious disadvantage of the SSM, since it implies the

possibility that a model could give significantly different global results for different resolutions.

### 6.1.3 Performance of DynSM, MixSSM, KEM and DSM

The DynSM, the MixSSM, the KEM and the DSM are developed to solve disadvantages of earlier models (e.g., the SM and the SSM). Many studies have explored that these four models provide better agreement with the filtered DNS results for different turbulent flows, including isotropic turbulence (Kobayashi & Shimomura [54], Pomraning & Rutland [85, 86]), turbulent mixing layer (Vreman [108]), and turbulent channel flow (Piomelli et al. [81, 82]). We investigate them in figure 6.7 with respect to the evolution of resolved kinetic energy. As mentioned in section 2.2.2, the DynSM and the KEM are two eddy-viscosity models. They yield much more accurate results than the SSM. For isotropic case E, however, the DynSM and the KEM still fail to yield sufficient dissipation, and result in lower kinetic energy decay rates. For rotating case F, the DynSM slightly overestimates the kinetic energy decay. This result is consistent with findings at high rotation rates (Horiuti [47]). The KEM performs similarly as the DynSM for rotating case F. For isotropic case E, the MixSSM yields more accurate kinetic energy decay rates than the SSM; and for rotating case F, the MixSSM yields slightly better results than the SSM. The expressions of the DynSM, the KEM and the MixSSM include eddy-viscosity terms (see section 2.2.2), but the DSM is a one-equation non-viscosity model. Pomraning & Rutland [85, 86] found that the DSM yields good results for low Reynolds number isotropic flows. For both high-Reynolds number cases E and F, the DSM is also capable to provide dissipation, and initially yields results similar to those of the other three models.

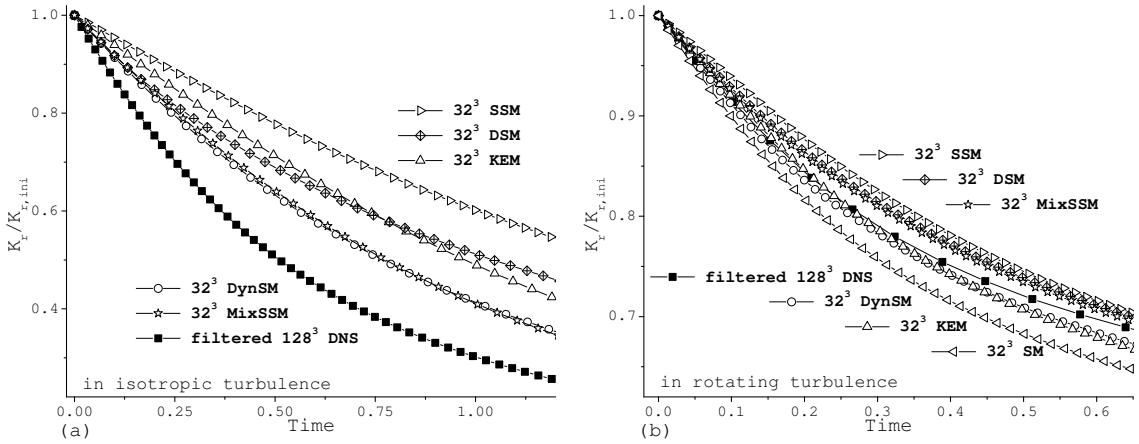


Figure 6.7: Evolution of resolved kinetic energy obtained from the filtered $128^3$ DNS, the $32^3$ DynSM, the $32^3$ MixSSM, the $32^3$ KEM, and the $32^3$ DSM (the $32^3$ SSM and the $32^3$ SM function as comparison references): (a) in isotropic turbulent case E; (b) in rotating case F.

Using a one-equation approach (e.g., the KEM and the DSM) enables us to calculate the ratio of SGS kinetic energy ($K_{sgs} = \int \frac{1}{2}\tau_{ii}\, d\vec{x}$) to total kinetic energy ($K_{sgs} + K_r$), and this calculation describes the dominant level of subgrid scales to resolved scales. Table 6.2 summarizes this ratio for different initial states. The subgrid scale velocity field initially accounts for $\sim 35\%$ of the turbulent kinetic energy at the resolution of $32^3$. The subgrid scale flows are of great intensity for current high-Reynolds number turbulent flows, and thus, the imperfect modeling of SGS stress may cause significant disagreement with the filtered DNS results as shown in figure 6.7.

It is important to examine the SGS energy production (Fig. 6.8) and the kinetic energy spectrum (Fig. 6.9) to understand the model performances further. These

Table 6.2: Ratios of initial SGS kinetic energy to total kinetic energy

| **Initial state** | **Grid resolution** | $\frac{K_{sgs}}{K_{sgs}+K_r} \times 100\%$ |
|---|---|---|
| I | $32^3$ | 34.5 |
| I | $64^3$ | 16.8 |
| R | $32^3$ | 38.5 |
| R | $64^3$ | 16.1 |

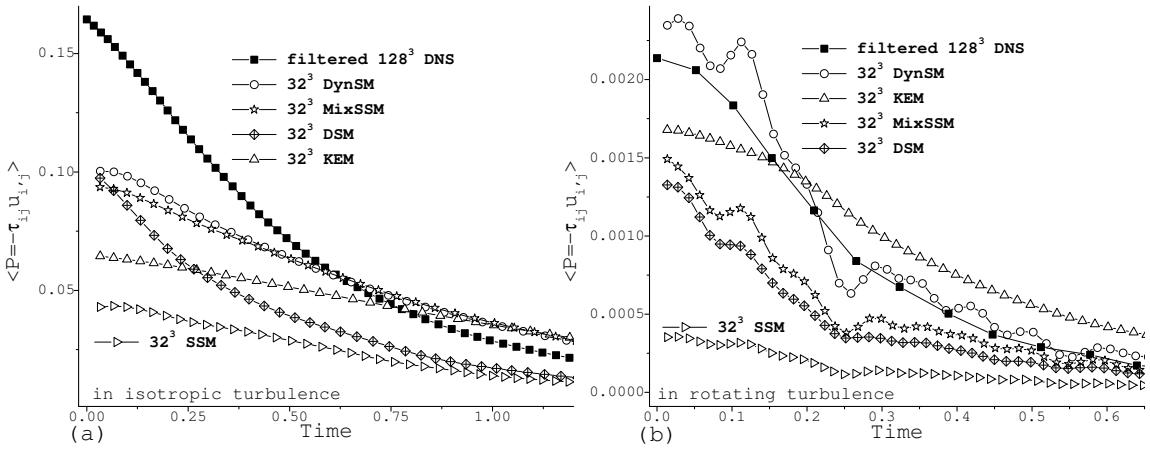


Figure 6.8: Evolution of SGS energy production obtained from the filtered $128^3$ DNS, the $32^3$ DynSM, the $32^3$ MixSSM, the $32^3$ KEM, and the $32^3$ DSM (the $32^3$ SSM functions as a comparison reference): (a) in isotropic case E; (b) in rotating case F.

four models yield more accurate results than the SSM, and the DynSM has the best results for both of the current cases over all. For rotating case F, the results from the DynSM and the KEM are in better agreement with the filtered DNS data concerning SGS energy production (Fig. 6.8(b)) and kinetic energy spectrum (Fig. 6.9(b)). For

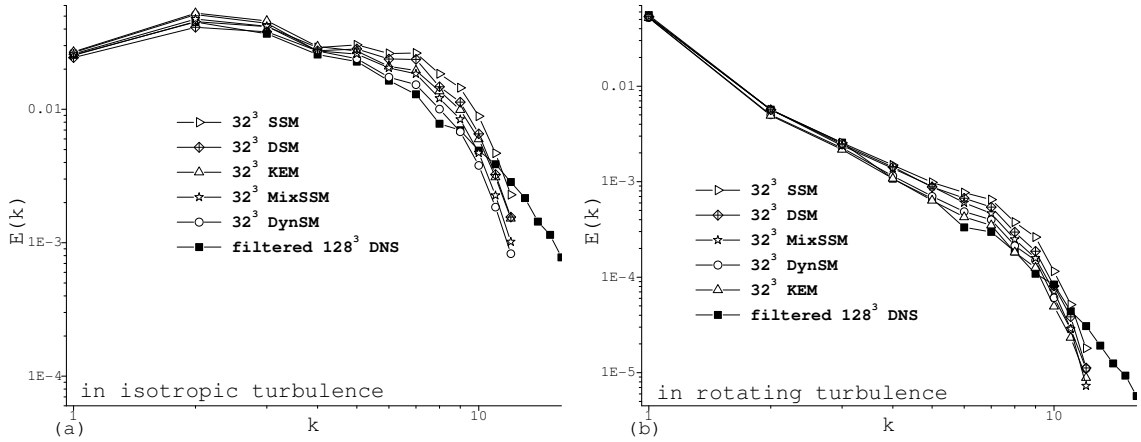


Figure 6.9: 3D kinetic energy spectrum obtained from the filtered $128^3$ DNS, the $32^3$ DynSM, the $32^3$ MixSSM, the $32^3$ KEM, and the $32^3$ DSM (the $32^3$ SSM functions as a comparison reference): (a) in isotropic turbulence case E at $time = 0.4$; (b) in rotating case F at $time = 0.7$.

isotropic case E, the KEM yields lower SGS energy prodocution (Fig. 6.8(a)). The MixSSM delivers similar SGS energy productions as the DynSM for isotropic case E, however, the MixSSM yields lower SGS energy production for rotating case F. For both isotropic case E and rotating case F, the DSM under-predicts the SGS energy productions. In conclusion, these four models deliver lower SGS energy production, which means the under-prediction of kinetic energy transfer from resolved to subgrid scales. To a certain degree, this fact causes lower kinetic energy decay rate as shown in figure 6.7, and insufficient dissipation at small scales as shown in figure 6.9.

### 6.1.4 Assessment of new models

The new models, the MixGCDSM and the MixSCDSM, are examined in figures 6.10 and 6.11 with respect to the temporal variations of the resolved kinetic energy.

Also the figures include the results for the resolution of $32^3$ and $64^3$, and the results from the simulation without a model and the SM as comparison references. We must note that at the *a-posteriori* level, the behaviors of the two new models are very similar, and the curve computed from the MixSCDSM ($-\,\square\,-$) covers the curve computed from the MixGCDSM ($-\,\nabla\,-$) in many of the following plots. Traditional models exhibit some disagreements more or less as shown in figures 6.3, 6.5 and 6.7. However, the resolved kinetic energy results obtained from the new models, clearly, are in excellent agreement with the filtered DNS data. Further, the new models deliver consistent results for the grid resolutions of $32^3$ and $64^3$. This fact satisfies the general expectation that LES predictions of turbulence statistics should depend minimally on the resolution length scale (Pope [88]).

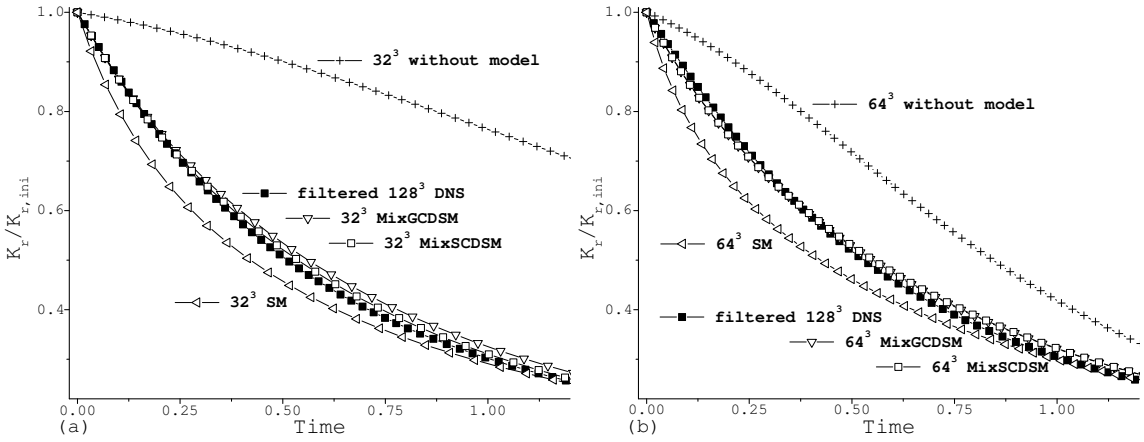


Figure 6.10: Evolution of resolved kinetic energy of isotropic case E: (a) the $32^3$ LES; (b) the $64^3$ LES. Results obtained from the simulation without a model and the SM are comparison references.

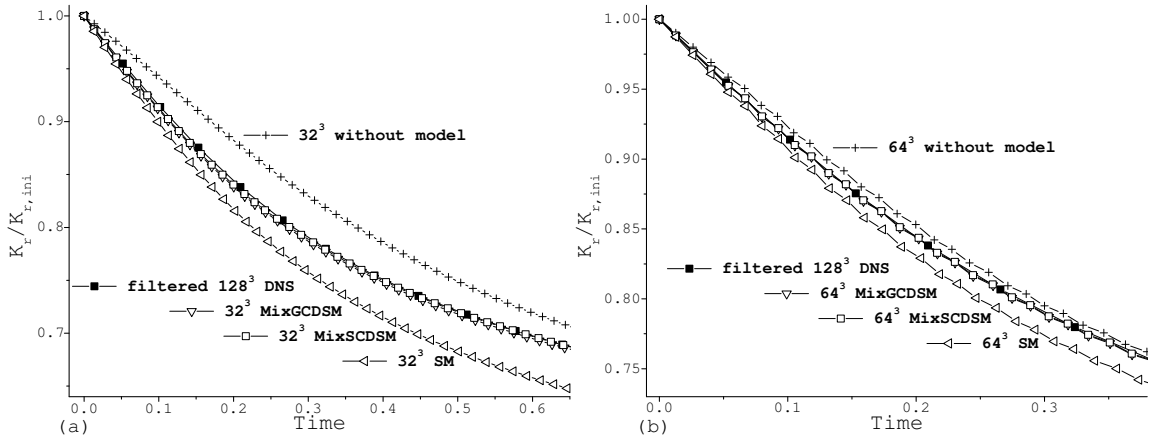


Figure 6.11: Evolution of resolved kinetic energy of rotating case F: (a) the $32^3$ LES; (b) the $64^3$ LES. Results obtained from the simulation without a model and the SM are comparison references.

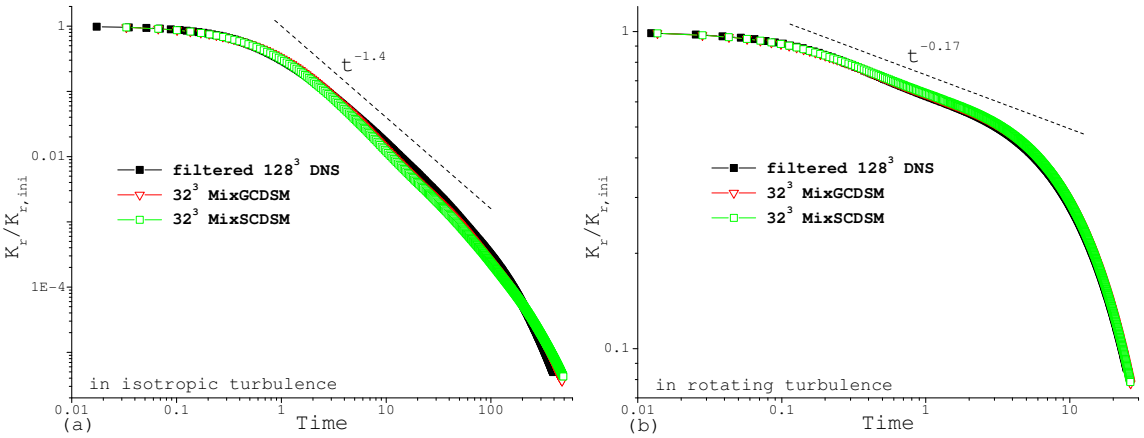


Figure 6.12: The kinetic energy decay rate from LES of two news models (MixGCDSM and MixSCDSM): (a) in isotropic case E; (b) in rotating case F.

Figure 6.12 shows the kinetic energy decay rates over a very long period derived from the filtered DNS data and the new models. The decay rate of isotropic turbulence

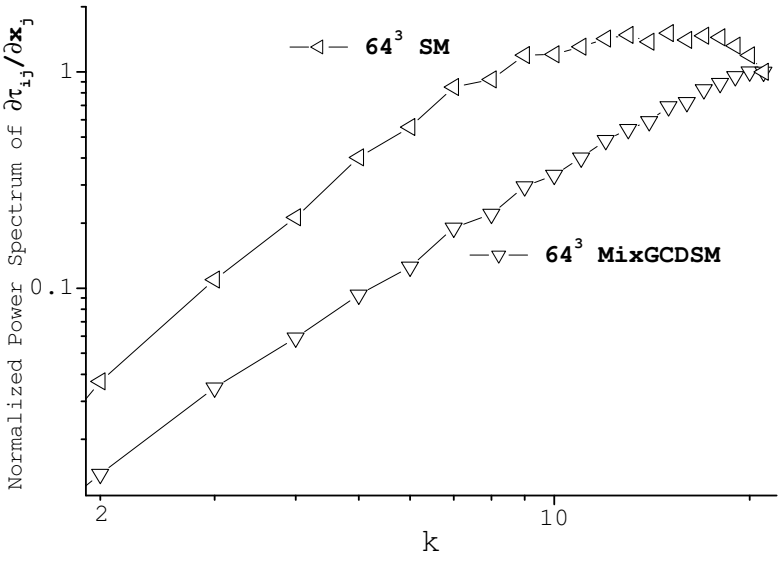


Figure 6.13: Normalized (at $k = 21$) power spectrum of $\partial\tau_{ij}/\partial x_j$ obtained from the $64^3$ SM and the $64^3$ MixGCDSM in the LES of isotropic case E.

is shown to be of the power-law form, and to depend on the initial conditions so that it varies from $-1.0$ to $-2.5$ (George [37]). The MixGCDSM and the MixSCDSM predict the decay rate ($\sim -1.4$) of isotropic case E very well. As mentioned in section 2.3.2, rotating turbulence generally has slower decay rates. The new models also yield an accurate decay rate ($\sim -0.17$) of rotating case F.

Figure 6.13 compares the SM (as a representative of eddy-viscosity model) and the MixGCDSM with respect to a $\partial\tau_{ij}/\partial x_j$ power spectrum, which is normalized by the magnitude at $k = 21$. The influences of the MixGCDSM on large scale flows are typically minor, and the SM yields more dissipation over all scales. The new models are more favorable than models using eddy-viscosity closure in terms of the avoidance of disturbing large scale flows. Figure 6.14 illustrates the kinetic energy

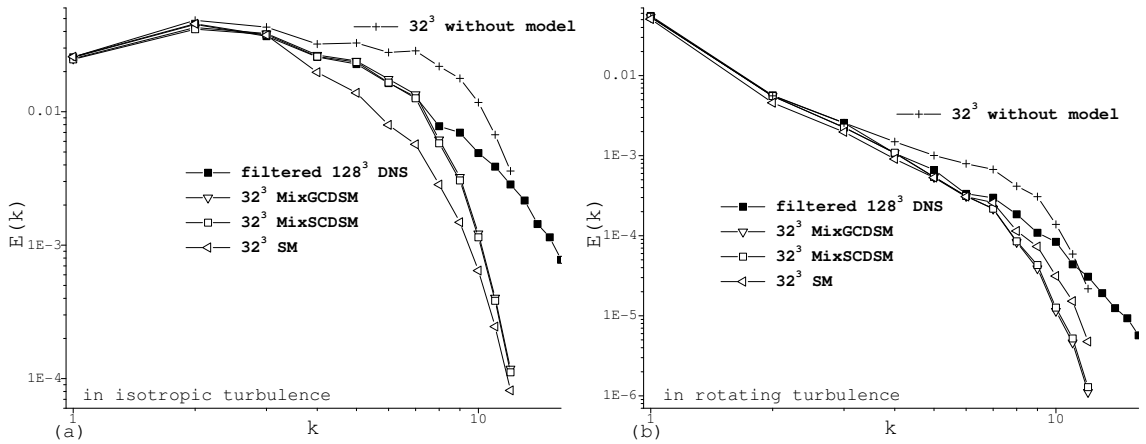


Figure 6.14: 3D kinetic energy spectrum obtained from the filtered $128^3$ DNS, the $32^3$ MixGCDSM, and the $32^3$ MixSCDSM (the $32^3$ without a model and the $32^3$ SM function as comparison references): (a) in isotropic turbulence case E at $time = 0.4$; (b) in rotating case F at $time = 0.7$.

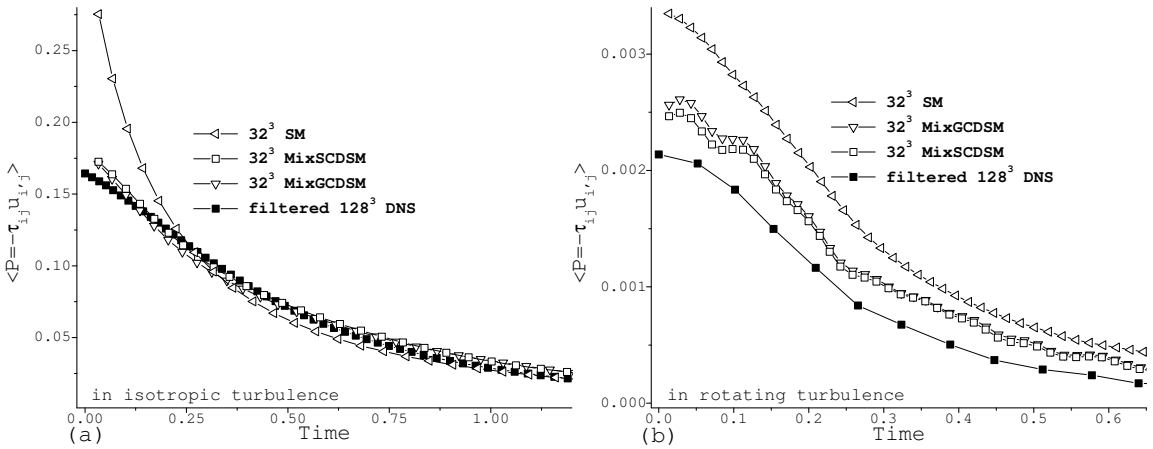


Figure 6.15: Evolution of SGS energy production obtained from the filtered $128^3$ DNS, the $32^3$ MixGCDSM, and the $32^3$ MixSCDSM (the $32^3$ SM functions as a comparison reference): (a) isotropic case E; (b) rotating case F.

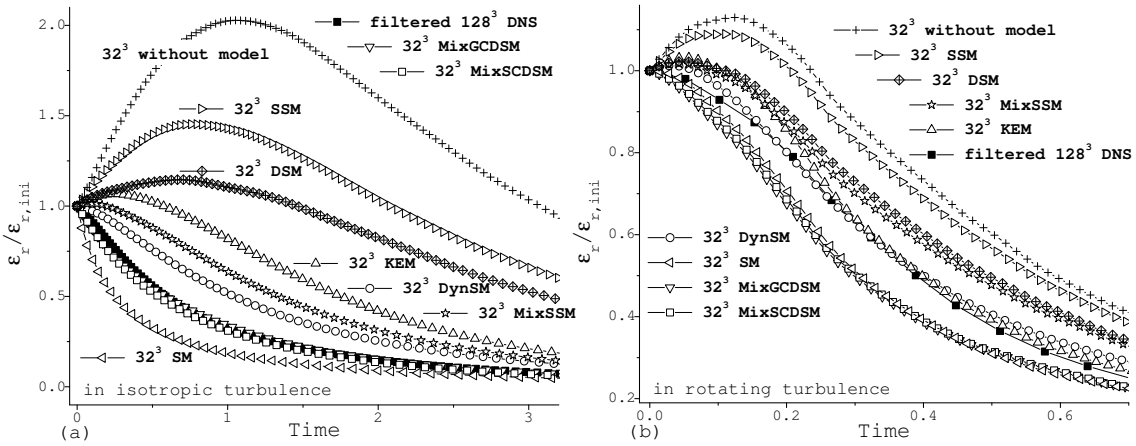


Figure 6.16: Evolution of resolved molecular dissipation: (a) in isotropic case E; (b) in rotating case F.

spectra obtained from the filtered DNS, the simulation without a model, the SM, the MixGCDSM and the MixSCDSM. The new models yields more accurate results at large scales than the SM, which clearly yields too much dissipation for large scale flows. Also, the new models have delivered sufficient dissipation at small scales.

Figure 6.15 shows that the SGS energy production is reasonably well predicted using the new models. As mentioned previously, the SGS energy production is generally larger than the molecular dissipation for our present cases. However, figure 6.16 offers a more complete comparison by examining the evolution of the normalized (by initial value) molecular dissipation integrated over the domain. The presence of too many small scales leads to the over-predicted molecular dissipation for the $32^3$ simulation without a model and for the SSM. In this way the molecular dissipation takes over part of the work that the SGS energy production should have performed. The new models give very accurate molecular dissipation for isotropic case E, and

give slightly lower levels of molecular dissipation for rotating case F. For rotating case F, the new models compensate this trivial weakness by slightly over-predicting SGS energy production as shown in figure 6.15(b). Thus, the new models yield very accurate total kinetic energy dissipation so that they predict kinetic energy decay rates very well as shown in figures 6.11 and 6.12(b).

### 6.1.5 Decay started with an isotropic turbulence

In this section, we assess the model performance using the decaying rotating case G, which starts with an initial condition of isotropic turbulence. Results for this case are similar to conclusions for cases E and F. So only a few results are shown.

Figures 6.17 and 6.18 examine the resolved kinetic energy and the kinetic energy spectrum that are at $time = 1.0$. Over all, the DynSM, the MixGCDSM and the MixSCDSM deliver more accurate results than other models. The MixGCDSM and the MixSCDSM are slightly too dissipative at the beginning. The DynSM is slightly too dissipative at the later period. The SSM, the MixSSM and the DSM yield insufficient dissipation, and this fact is associated with kinetic energy accumulation at small scales as shown in figure 6.18. The KEM and the SM yield too much dissipation, however, the results obtained from the KEM exhibit better agreement with the filtered DNS data than the SM. Also, the kinetic energy spectra illustrate that the SM dissipates kinetic energy excessively over a wide range of length scales.

## 6.2 Forced rotating turbulence

Decaying rotating turbulence, which ignores the effects of forcing, is a typical setup for the assessment of SGS models (Kobayashi & Shimomura [54], Horiuti [47,

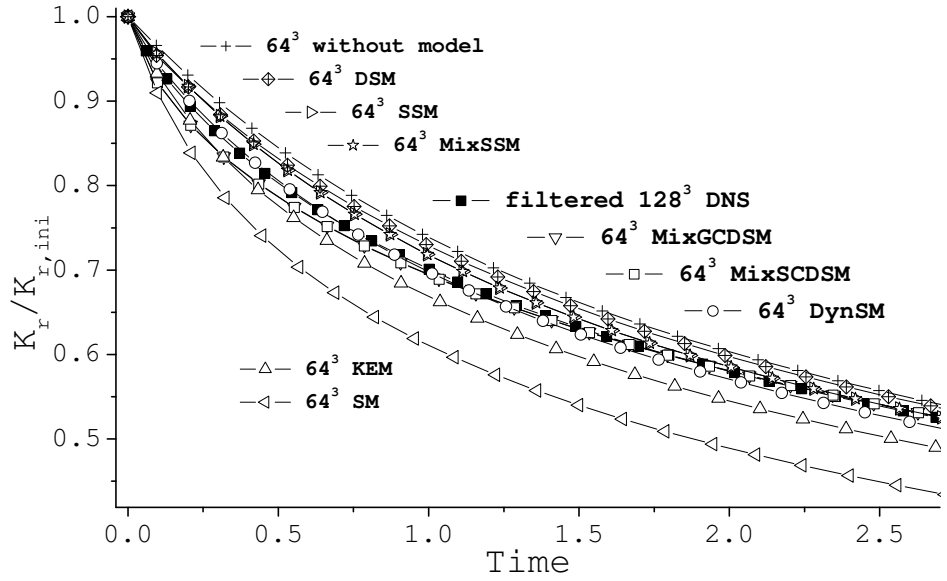


Figure 6.17: Evolution of resolved kinetic energy obtained from various SGS models in decaying case G.

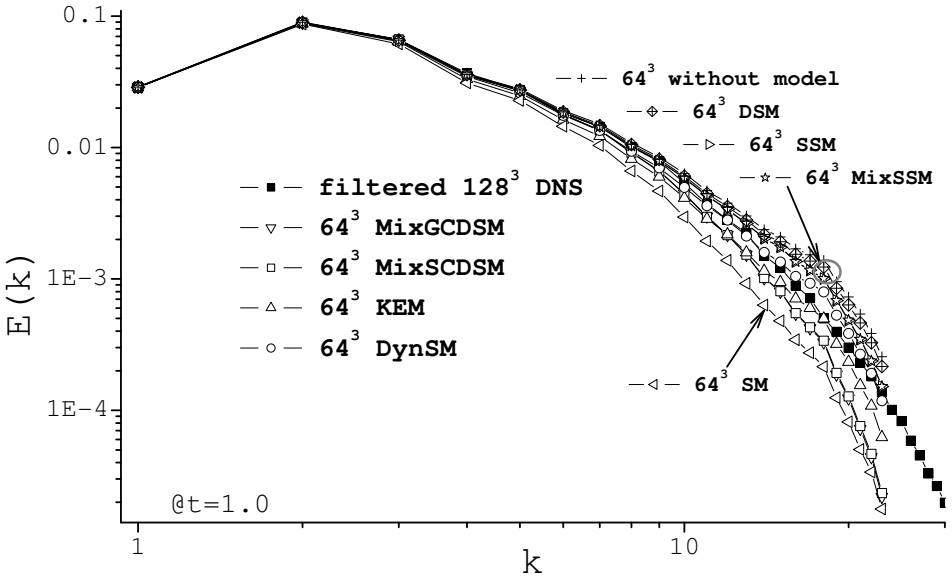


Figure 6.18: 3D kinetic energy spectrum obtained from various SGS models in decaying case G at $time = 1.0$.

48], Yang & Domaradzki [112]). Deardorff [31] and Piomelli & Liu [82] applied models to rotating turbulence in channels, which involved certain kinetic energy sources. Different from previous works, we include the Gaussian forcing in rotating turbulence but exclude boundary layer effects of channel flows. We find that only the new models can capture the anisotropic features of rotating turbulence with forcing. Note that in subsequent discussions, we normalized time using the period of system rotation, $T = 2\pi/\Omega$, which is an external parameter.

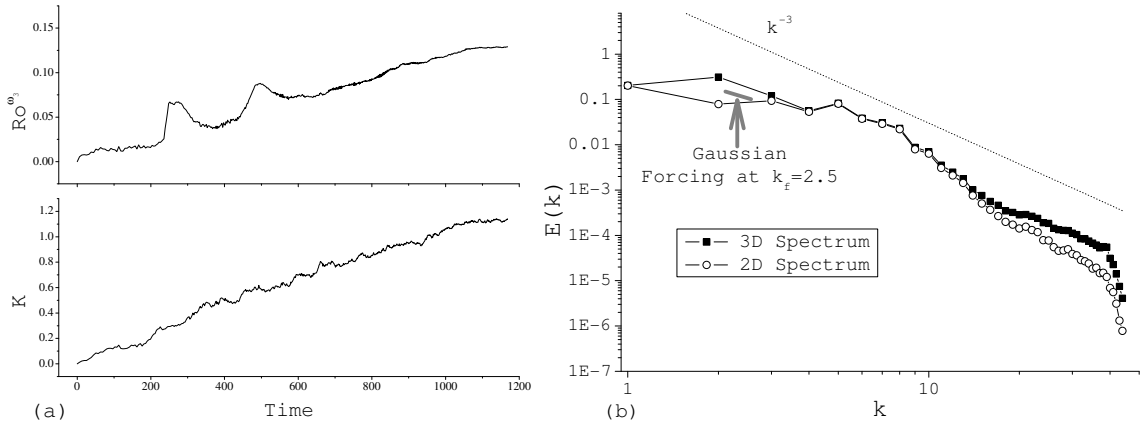


Figure 6.19: $128^3$ simulation of a large scale forced rotating turbulence: (a) evolutions of $Ro^{\omega_3}$ and the total kinetic energy $K$; (b) 3D & 2D kinetic energy spectra in a quasi-steady state.

### 6.2.1 Large scale forcing

We have performed a rotating turbulent case ($\Omega = 24\ [rad/s]$) at the resolution of $128^3$ to serve as the benchmark case. This case has hyper-viscosity for small scales, and large scale ($k_f = 2.5$) flows accept kinetic energy inputs via the Gaussian forcing. Figure 6.19(a) shows the evolution of $Ro^{\omega_3}$ and the total kinetic energy evolution.

Figure 6.19(b) shows the 3D & 2D kinetic energy spectra in a quasi-steady state, in which small scale flows have become statistically steady. A straight line of $k^{-3}$ is placed as a reference, but we do not assert that large scale forced rotating turbulence should have $E(k) \propto k^{-3}$ in the inertial range. Currently, the understanding of kinetic energy spectral behavior of large scale forced rotating turbulence remains incomplete.

The LES simulations have the same kinetic energy input setup as the $128^3$ simulation. We have turned off molecular viscosity, hypo- and hyper-viscosities. Thus, kinetic energy can transfer first to subgrid scales and then to internal energy only with the assistance of SGS models. All simulations have been performed at coarser grids, $32^3$ or $64^3$, and allowed to reach their statistically steady states.

#### 6.2.1.1 Performance of traditional models

We have applied all SGS models (see section 2.2.2) to the LES of large scale forced rotating turbulence. Figure 6.20 shows the 3D & 2D kinetic energy spectra in a statistically steady state obtained from the SM, the SSM, the MixSSM and the DSM at the grid resolution of $64^3$. The resolved kinetic energy evolution of each simulation is also presented. These models are good representatives of current SGS models. However, except the MixSSM, other models fail to deliver the quasi two-dimensional structure at large scales. All models fail to dissipate kinetic energy at small scales. Among these models, the MixSSM has the best performance.

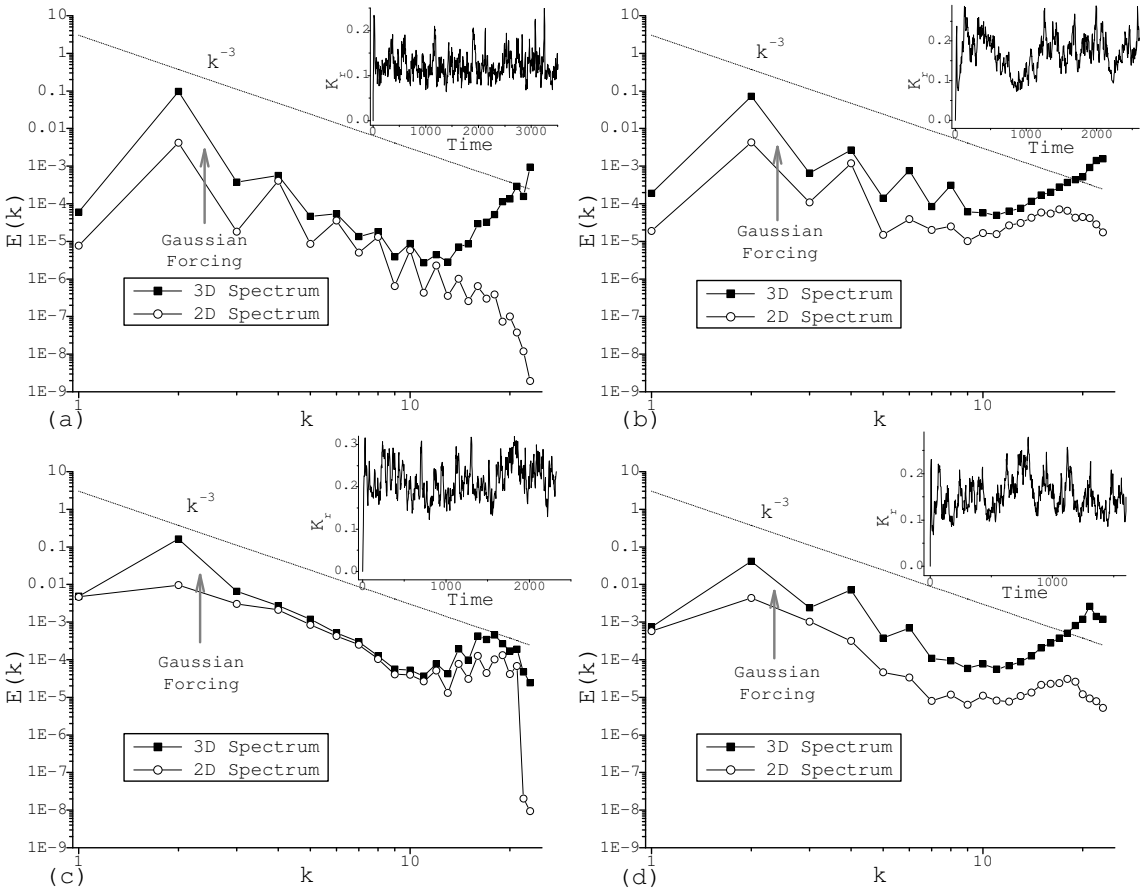


Figure 6.20: 3D & 2D kinetic energy spectra in a statistically steady state in the LES of large scale forced rotating turbulence using: (a) the $64^3$ SM; (b) the $64^3$ SSM; (c) the $64^3$ MixSSM; (d) the $64^3$ DSM. The evolution of $K_r$ is included for each case.

### 6.2.1.2 Assessment of the new models

The performance of the two new models is very similar to each other regarding the *a-posteriori* test of decaying turbulence (section 6.1.4). Another instance of similarity arises regarding the *a-posteriori* test of forced rotating turbulence. Thus, for simplicity, only the results obtained from the MixGCDSM will be presented.

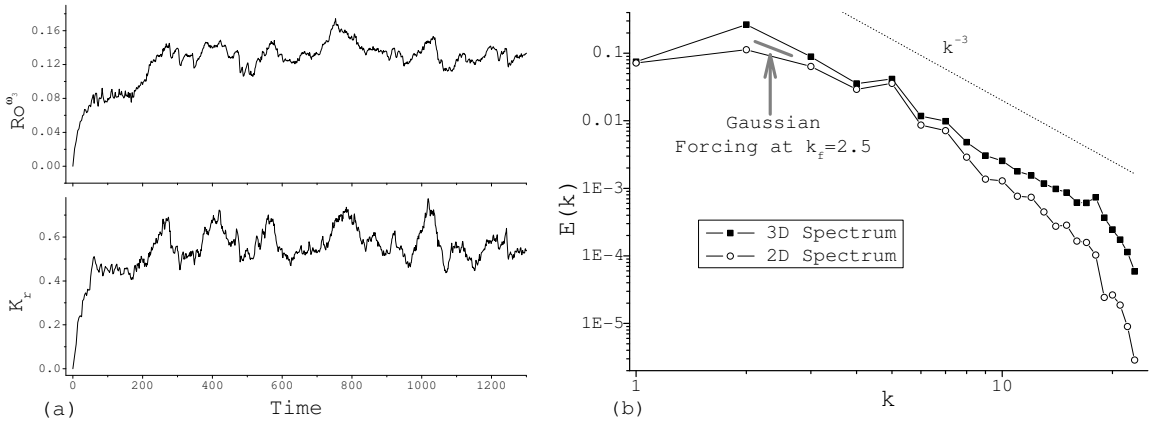


Figure 6.21: $64^3$ LES of large scale forced rotating turbulence using the MixGCDSM: (a) evolutions of $Ro^{\omega_3}$ and the resolved kinetic energy $K_r$; (b) 3D & 2D kinetic energy spectra in a statistically steady state.

Figure 6.21 examines the MixGCDSM with respect to the evolutions of $Ro^{\omega_3}$, the resolved kinetic energy evolution, and the 3D & 2D energy spectra in a statistically steady state. We have matched $Ro^{\omega_3} = 0.12$ with the $128^3$ simulation by specifying $\Omega = 8\ [rad/s]$. The MixGCDSM facilitates the two-dimensionalization process resulting in very close 3D & 2D energy spectra at large scales, $k \lesssim 7$. Thus, we use the averaged (in the z-direction) velocity field as shown in figure 6.22 to understand the physical structures. Note that the z-averaged velocity field will not accord with the resolved kinetic energy contour if the flow is still highly 3D. For instance, the velocity fields as shown in figures 6.22(b) and 6.22(c) occur during a critical period, in which 2D flows at large scales are developing. Figure 6.22(b) shows that the resolved kinetic energy contours did not match the velocity vectors, however, figure 6.22(c) shows that they harmonized well with each other, and that two eddies are merging into a bigger

one around the coordinate $(x,\ y) \approx (0,\ 1)$. Figure 6.22(d) shows a typical physical field in a statistically steady state.

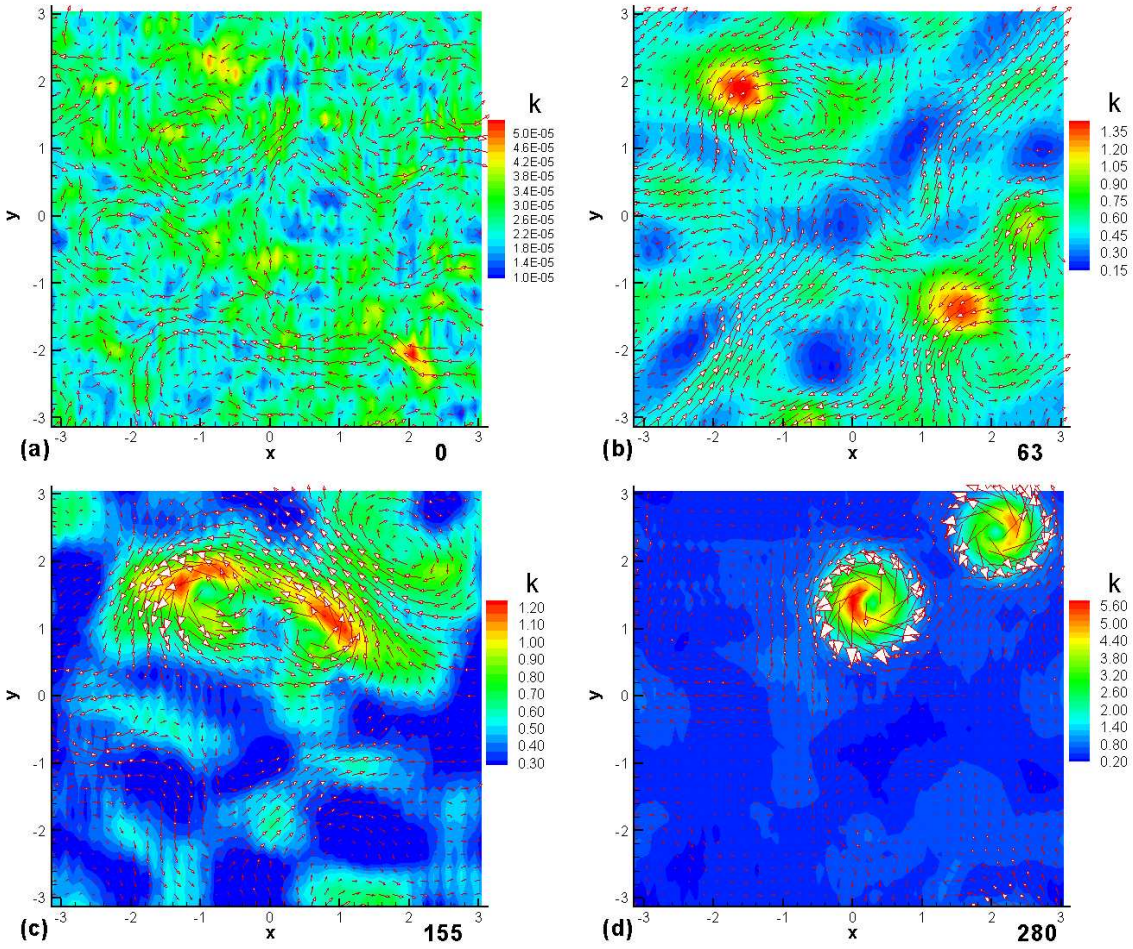


Figure 6.22: Time sequence of averaged (in the z-direction) resolved kinetic energy contours and velocity vectors for the $64^3$ LES of large scale forced rotating turbulence using the MixGCDSM: (a) in an initial state; (b) at $time = 63$; (c) at $time = 155$; (d) at $time = 280$.

The vortex regions are identified using the criterion $\lambda_2 < 0$ (where, $\lambda_2$ is the second large eigenvalue of tensor $S_{im}S_{mj} + \Omega_{im}\Omega_{mj}$, $S_{ij} = (\partial u_i/\partial x_j + \partial u_j/\partial x_i)/2$,

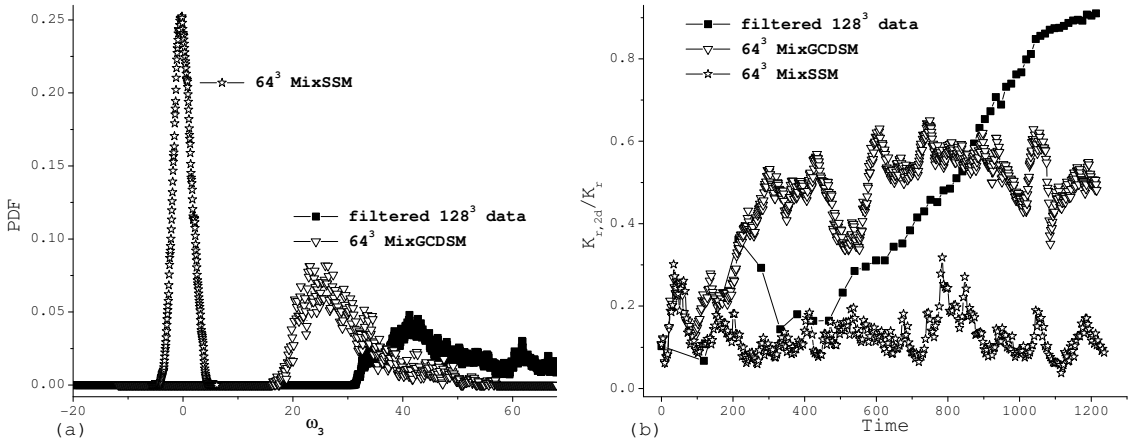


Figure 6.23: Assessment of the MixGCDSM and the MixSSM with respect to: (a) PDF of $\omega_3$, and (b) $K_{r,2d}/K_r$, in large scale forced rotating turbulence.

and $\Omega_{ij} = (\partial u_i/\partial x_j - \partial u_j/\partial x_i)/2)$ for a vortex region in 2D (Jeong & Hussain [50]), and are sampled over points $(x,\ y)$ with $\lambda_2 < (1/6)\min(\lambda_2)$ to get $PDF(\omega_3)$. Figure 6.23(a) compares the MixGCDSM and the MixSSM with respect to $PDF(\omega_3)$. The MixGCDSM successfully captures the symmetry breaking between cyclones and anti-cyclones in favor of cyclones. The physical field in a steady state (Fig. 6.22(d)) also illustrates this feature clearly. None of traditional SGS models, including the MixSSM, are able to capture both the quasi 2D feature and the cyclonic feature. Further, figure 6.23(b) illustrates the temporal variations of the ratio of resolved 2D kinetic energy to resolved (3D) kinetic energy, $K_{r,2d}/K_r$. The MixGCDSM does not yield a ratio $\sim 0.9$ as the $128^3$ simulation, however, the MixGCDSM delivers the two-dimensionality much better than traditional models (Fig. 6.23(b)).

Referring to the integral length scale properties of fully developed rotating turbulence, Cambon et al. [16, 15] have illustrated that $2L_{11}^3$ is no longer equal to $L_{33}^3$,

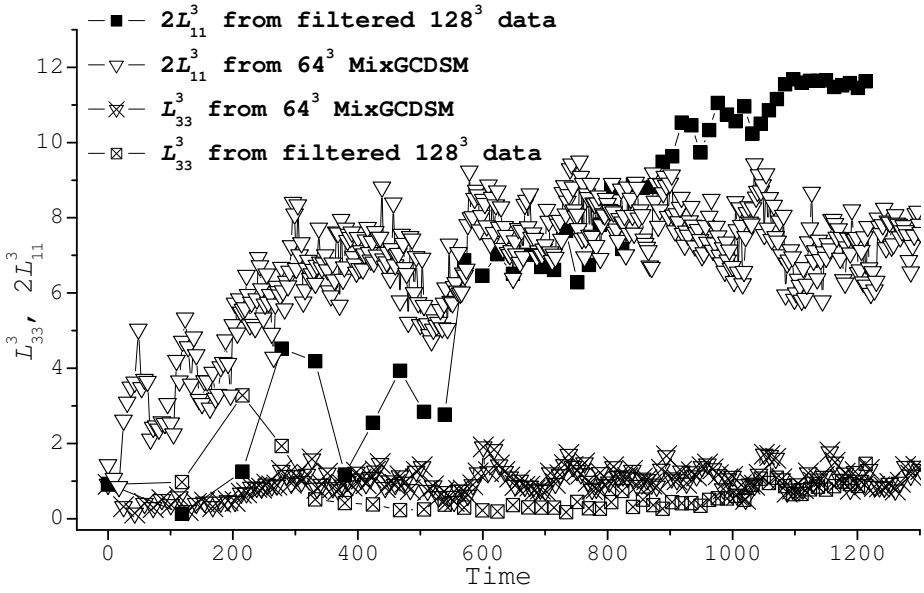


Figure 6.24: Temporal variations of integral length scales obtained from the filtered $128^3$ DNS, the MixGCDSM and the MixSSM, in large scale forced rotating turbulence.

but yields the inequality of $2L_{11}^3 > L_{33}^3$ (section 2.3.2). Figure 6.24 shows that the MixGCDSM also successfully delivers this anisotropic feature, while other models fail.

The one-equation approach enables us to compute an effective dissipation at subgrid scales, $\varepsilon_e = C_c \frac{k_{sgs}^{3/2}}{\Delta}$ (see equation (2.46)), which is the total dissipation for current turbulent flow since no other dissipations are included. Then, we can define an effective micro-scale Reynolds number as

$$Re_e = \left( \frac{20}{3} \frac{K_r^2}{\varepsilon_e \nu_e} \right)^{\frac{1}{2}} , \tag{6.3}$$

where effective molecular viscosity is $\nu_e = \varepsilon_e / \int 2k^2 E(k)\, dk$. In decaying cases E, F and G, the initial Taylor micro-scale Reynolds number ($\sim 85$) is typically higher than this effective micro-scale Reynolds number ($\sim 30$), because kinetic energy transfers

into internal energy only partially through subgrid scales. Effective Reynolds number provides the capability to evaluate the turbulent level of current LES without using molecular viscosity. This $64^3$ LES using the MixGCDSM yields $Re_e \approx 300$, and the following $32^3$ LES using the MixGCDSM yields $Re_e \approx 400$. These simulations are undoubtedly performed at very high Reynolds numbers.

Figure 6.25 examines the MixGCDSM at the resolution of $32^3$. The Rossby number of the statistically steady state is $Ro^{\omega_3} = 0.1$. If compare the kinetic energy spectrum plots 6.21(b) and 6.25(b), the model performs better on a finer resolution. However, the MixGCDSM is still able to capture the cyclonic/anti-cyclonic asymmetry in favor of cyclones on the coarser grid.

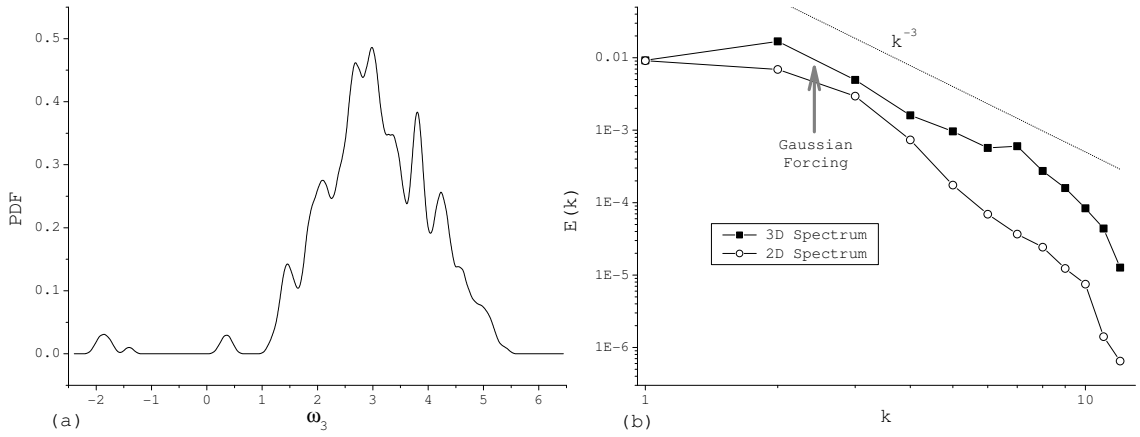


Figure 6.25: Assessment of the $32^3$ LES of large scale forced rotating turbulence using the MixGCDSM: (a) PDF of $\omega_3$, and (b) 3D & 2D kinetic energy spectra of statistically steady state.

In order to compare the differences between MFI-consistent models and inconsistent models, additionally in figure 6.26, we examine the MixDSM at the resolution

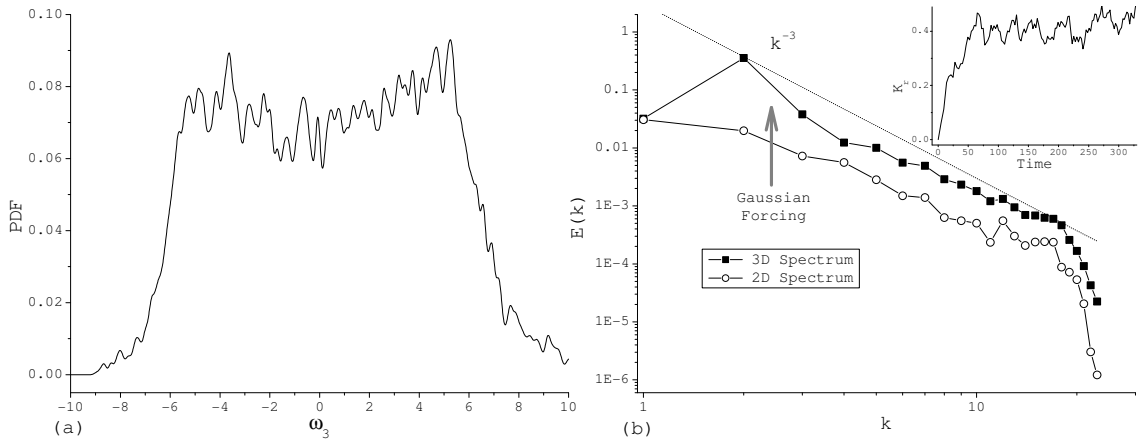


Figure 6.26: Assessment of the $64^3$ LES of large scale forced rotating turbulence using the MixDSM: (a) PDF of $\omega_3$, and (b) 3D & 2D kinetic energy spectra of statistically steady state.

of $64^3$. The MixDSM includes the same hyper-viscosity term as the MixGCDSM (see equation (3.8)), and thus, the MixDSM can better dissipate kinetic energy at small scales than the DSM does. However, the MixDSM also fails to deliver the cyclonic feature (Fig. 6.26(a)) and the quasi 2D feature (Fig. 6.26(b)).

### 6.2.2 Intermediate scale forcing

We have performed a $128^3$ rotating turbulent case ($\Omega = 13\ [rad/s]$) as a benchmark case. It is forced at $k_f = 12$ and includes only hyper-viscosity. Such problems have been studied extensively in numerical simulations (Smith et al. [97, 96]). Figure 6.27 shows the evolution of $Ro^{\omega_3}$, the total kinetic energy evolution, and the 3D & 2D kinetic energy spectra in a quasi-steady state, in which small scale flows and micro-scale properties (e.g., $Ro^{\omega_3}$) have become statistically steady.

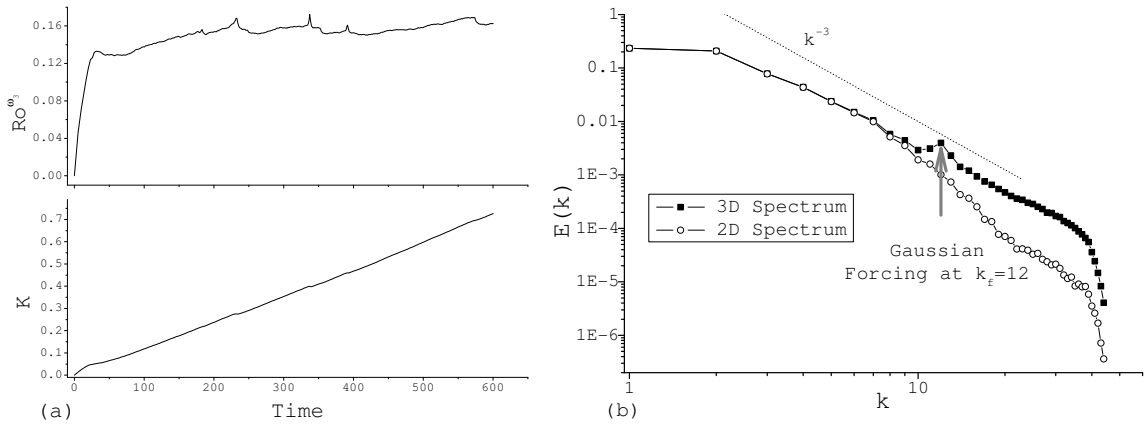


Figure 6.27: $128^3$ simulation of rotating turbulence, which was force at $k_f = 12$: (a) evolutions of $Ro^{\omega_3}$ and the total kinetic energy $K$; (b) 3D & 2D kinetic energy spectra in a quasi-steady state.

#### 6.2.2.1 Performance of SGS models

The LES simulation for this rotating turbulent case had the same kinetic energy input setup as the $128^3$ simulation but are performed at a coarser grid, $64^3$. The molecular viscosity, hypo- and hyper-viscosities have been turned off, thus the kinetic energy can transfer to large scales and into the formation of internal energy only with the assistance of SGS models. All simulations reach statistically steady states.

Figure 6.28 shows the 3D & 2D kinetic spectra that were in a statistically steady state obtained from the SM, the SSM, the MixSSM and the DSM. Clearly the SSM and the DSM are not dissipative enough, and also fail to facilitate the reverse energy transfer to large scales. The SM and the MixSSM include eddy-viscosities in their model expression, and thus they facilitate to dissipate kinetic energy at small scales

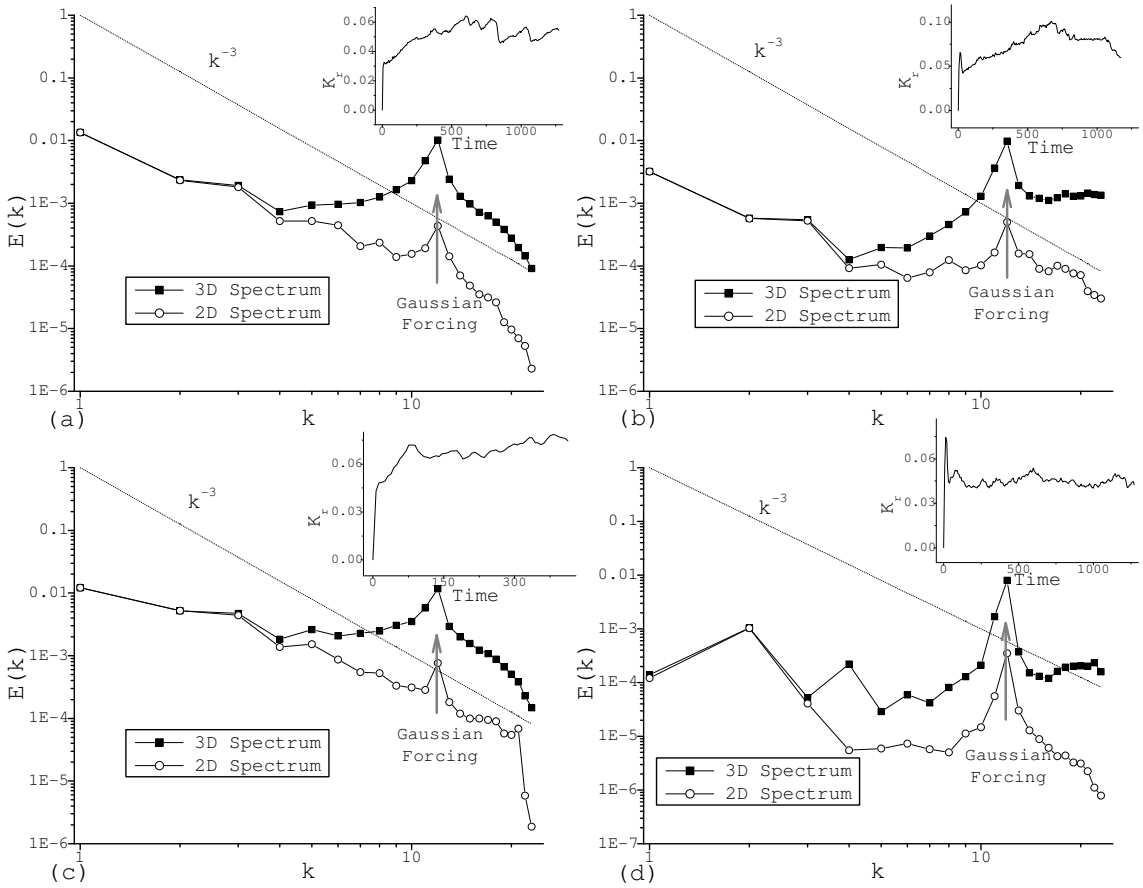


Figure 6.28: 3D & 2D kinetic energy spectra in a statistically steady state in the LES of intermediate scale forced rotating turbulence using: (a) the $64^3$ SM; (b) the $64^3$ SSM; (c) the $64^3$ MixSSM; (d) the $64^3$ DSM. The evolution of $K_r$ is included for each case.

as shown in figure 6.28(a) and figure 6.28(c). To a certain degree, they facilitate the reverse energy transfer to large scales.

In the simulation using the MixGCDSM, we have matched $Ro^{\omega_3} = 0.16$ with the $128^3$ simulation by specifying $\Omega = 8\ [rad/s]$. The effective micro-scale Reynolds number of this simulation is $Re_e \approx 150$. As shown in figure 6.29, the MixGCDSM

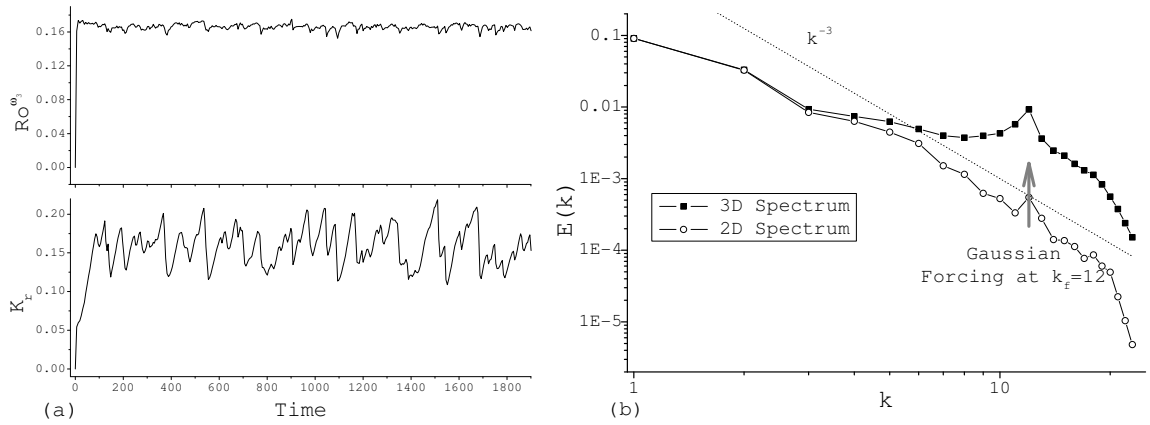


Figure 6.29: $64^3$ LES of intermediate scale forced rotating turbulence using the MixGCDSM: (a) evolutions of $Ro^{\omega_3}$ and the resolved kinetic energy $K_r$; (b) 3D & 2D kinetic energy spectra in a statistically steady state.

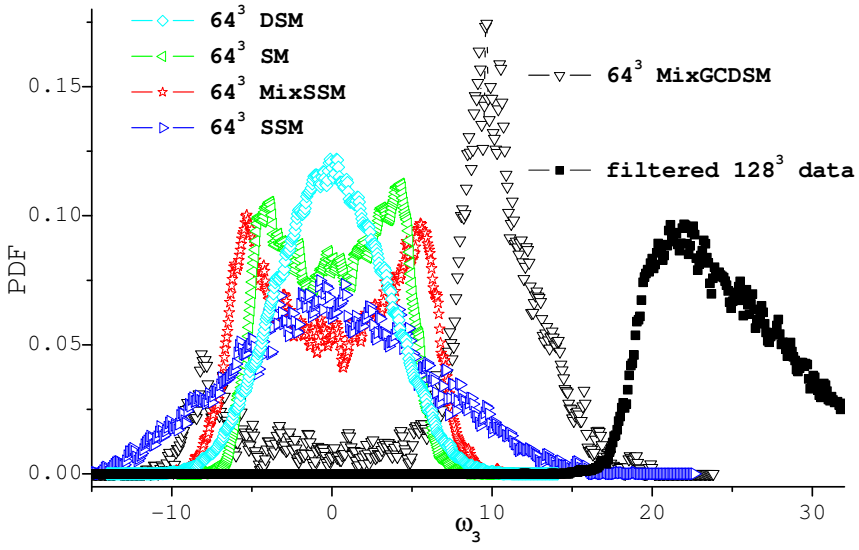


Figure 6.30: PDF of $\omega_3$ in intermediate scale forced rotating turbulence obtained from the $128^3$ simulation, the $64^3$ SM, the $64^3$ SSM, the $64^3$ MixSSM, and the $64^3$ MixGCDSM.

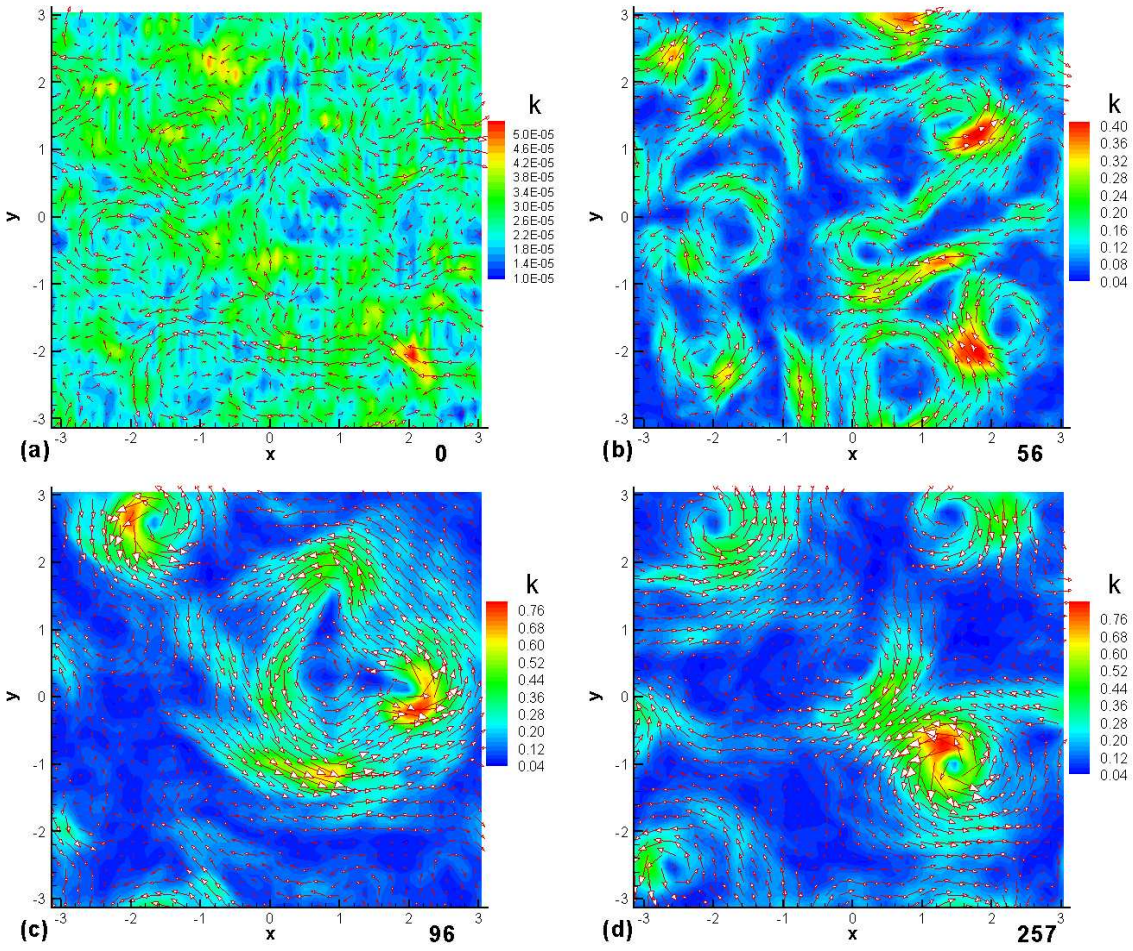


Figure 6.31: Time sequence of averaged (in the z-direction) resolved kinetic energy contours and velocity vectors obtained from the $64^3$ LES of intermediate scale forced rotating turbulence using the MixGCDSM: (a) in an initial state; (b) at $time = 56$; (c) at $time = 96$; (d) at $time = 257$.

delivers better results than traditional models (Fig. 6.28) regarding dissipation at small scales and reverse energy transfer to large scales.

SGS models are compared in figure 6.30 with respect to $PDF(\omega_3)$ obtained from the $128^3$ simulation, the SM, the SSM, the MixSSM, and the MixGCDSM. Figure

6.31 shows the time sequence of the z-averaged resolved kinetic energy contours and velocity vectors obtained from the $64^3$ MixGCDSM. Both figures illustrate that the MixGCDSM successfully delivers the symmetry breaking between cyclones and anti-cyclones in favor of cyclones.

## 6.3 Summary

Tables 6.3 and 6.4 summarize the results for SGS models at the *a-posteriori* test level. The models are listed with symbols to indicate if they performed poorly or well on each diagnostic.

Table 6.3: Comparison of model performance in the LES of decaying turbulence (initially with high Reynolds number) at the *a-posteriori* test level

| **Diagnostic** | SM | KEM | DynSM | SSM | MixSSM | DSM | MixSCDSM | MixGCDSM |
|---|---|---|---|---|---|---|---|---|
| Kinetic energy | − | 0 | 0 | − | − | − | + | + |
| SGS energy production | − | 0 | 0 | − | − | − | + | + |
| Molecular dissipation | 0 | 0 | 0 | − | − | − | + | + |
| Energy spectrum | − | + | + | − | + | − | + | + |

The symbols − and + refer to bad and good results. The symbol 0 refers to bad results in isotropic case, but good results in rotating turbulent case.

As is well known, eddy-viscosity models facilitate to transfer kinetic energy only from resolved scales to subgrid scales, and they are also too dissipative. The SM yields excessive dissipations for both high-Reynolds number isotropic and rotating turbulent flows. The DynSM and the KEM yield very accurate results for high-Reynolds number rotating turbulence, even though, they are slightly over dissipative.

Table 6.4: Comparison of model performance in the LES of forced rotating turbulence at the *a-posteriori* test level

| **Diagnostic** | SM | SSM | MixSSM | DSM | MixDSM | MixSCDSM | MixGCDSM |
|---|---|---|---|---|---|---|---|
| Cyclonic structure | − | − | − | − | 0 | + | + |
| Quasi 2D flow | − | − | − | − | 0 | + | + |

The symbols − and + refer to bad and good results. The symbol 0 refers to bad results in large scale forced rotating turbulence, but good results in intermediate scale forced rotating turbulence.

The mixed approach is a remarkable improvement in LES modeling. First, the additional eddy-viscosity term is usually much smaller than the original structure term. An analytical point of view is that the mixed eddy-viscosity term is modeling of the higher order term in the Taylor expansion of SGS stress, or the modified SGS Reynolds stress term. Also, the eddy-viscosity term is trace free. So, it will not change the trace of the original structure term, and mixed dynamic structure models still satisfies the trace requirement $\tau_{ii}^{model} = \tau_{ii}$. Further, the eddy-viscosity term significantly facilitates the kinetic energy dissipation at small scales and stables the simulations.

It is important to note that the MixGCDSM is a very fast numerical approach. The following table compares the models with respect to the average calculation time per step on Intel's 64-Bit Pentium 4 3.4GHz CPU in the decaying turbulent cases at the resolution of $32^3$

| $T_{SM}$ | : | $T_{KEM}$ | : | $T_{MixGCDSM}$ | : | $T_{SSM}$ | : | $T_{DSM}$ | : | $T_{MixSCDSM}$ | : | $T_{DynSM}$ | : | $T_{MixSSM}$ | $\approx$ |
|---|---|---|---|---|---|---|---|---|---|---|---|---|---|---|---|
| 1.00 | : | 1.15 | : | 1.15 | : | 2.46 | : | 4.83 | : | 5.23 | : | 7.69 | : | 13.0 | , |

where we normalized all values by the calculation time of the SM. A few interesting points, which are helpful to choose models and build computational efficient codes, are revealed. First, the test filtering and the determining of the dynamic coefficient (e.g., $C_D$ and $C_D^{SSM}$) based on Germano identity slow down calculations significantly. There exist increased calculational costs from 1.0 when using the SM to 7.69 when using the DynSM, and 13.0 when using the MixSSM. Further, the solving of additional SGS energy equation does not increase the computer time very much in comparison with the test filtering and determining of the dynamic coefficient. For instance, compared with the SM, the one-equation eddy-viscosity model - the KEM, has only increased calculation time by 15%. At last, we state that the using of pseudo-spectral method allows to calculate gradients very efficiently in Fourier space. It facilitates to reduce the computational cost of using the SM, the KEM, and the MixGCDSM. Finite difference/volume/element methods may not have this advantage.

# Chapter 7

# Conclusion

In LES, the large scale flows are explicitly solved, and the small scale motions are modeled. Traditionally, SGS models are based on the assumption that small scale flows are homogeneous and isotropic, and do not account for any anisotropy including rotational effects. However, rotating turbulence has many well known anisotropic features, such as quasi 2D flow at large scales and cyclonic structures. The performances of traditional models in the LES of rotating turbulence are questioned.

The purposes of this project are to study the performances of various SGS models and to develop models better suited to rotating turbulence. The current work has used *a-priori* and *a-posteriori* tests to accomplish the purposes. At the *a-priori* level, models were examined and compared using correlation and regression coefficients, from traditional eddy viscosity models to new one-equation models introduced herein. At the *a-posteriori* level, we achieved a systematic investigation of the model performance in the actual LES of rotating turbulence including decaying and forced cases.

The modeling of the SGS stress was considered from a theoretical standpoint - the consistency with the constraints of material frame indifference. Under the Euclidean group of transformations, the SGS stress tensor in an inertial frame is connected to the SGS stress tensor in a rotating frame according to a fame different

expression. The stress tensor is of course important, because it appears in the SGS kinetic energy equation. The modeled stress tensor is assumed be MFI-consistent with the actual stress tensor, otherwise, modeling errors will be certainly added into the fluid dynamic system.

Most traditional SGS models, including eddy viscosity models and the SSM have no explicit method to account for anisotropy of length scales and MFI-consistence, and thus they perform poorly in rotating turbulence. We examined additional models (the KEM and the DSM) that showed somewhat better results, but still do not satisfy the consistency with MFI at the stress tensor level, and therefore failed to capture the anisotropy effects due to rotation.

To account properly for MFI, we introduced two new one-equation models which are variants of the dynamic structure model, namely the GCDSM and the SCDSM. By construction these new models satisfy the consistency with MFI and the trace requirement $\tau_{ii}^{model} = 2k_{sgs}$. Accordingly these new models greatly improve the regression coefficients for modeling components in all directions.

Eddy viscosity models fail to give good correlation coefficients in both isotropic and rotating turbulence, and these coefficients are lower for rotating turbulence. Also, eddy viscosity models are purely dissipative, and analysis of the SGS energy production shows that the SM and the KEM are too dissipative at all scales in rotating turbulence. This is not surprising since eddy viscosity models are originally conceived for isotropic turbulence, and it is well known that strong rotating inhibits the forward cascade of energy leading to lower levels of the energy dissipation rate. In the *a-posteriori* tests of decaying turbulence, the SM was confirmed to dissipate excessively over all scales.

At the *a-posteriori* test level, we added a hyper-viscosity term to the GCDSM and the SCDSM, and formed their mixed versions: the MixGCDSM and the MixSCDSM. The mixed approaches are more helpful to dissipate kinetic energy at small scales than the original models. Also, compared with the traditional approach of using an eddy-viscosity term, the effects of a hyper-viscosity term at large scales are significantly smaller. This fact is a desired feature of LES modeling.

In decaying turbulence testing, the MixGCDSM and the MixSCDSM are promising, and yield more accurate results than other models in many aspects, such as resolved kinetic energy, SGS energy production, molecular dissipation, and energy spectrum. These results also are consistent at different resolutions. In forced rotating turbulence testing, the MixGCDSM and the MixSCDSM have shown their capabilities to deliver major anisotropic features of rotating turbulence.

# LIST OF REFERENCES

# LIST OF REFERENCES

[1] N. Andersson, L. Eriksson, and L. Davidson. Les prediction of flow and acoustic field of a coaxial jet. *AIAA-2005-2884, 11th AIAA/CEAS Aeroacoustics Conference, Monterey, California*, May 2005.

[2] J. Bardina, J. H. Ferziger, and W. C. Reynolds. Improved subgrid scale models for large eddy simulation. *AIAA Paper 80-1357*, 1980.

[3] J. Bardina, J. H. Ferziger, and W. C. Reynolds. Improved turbulence models based on large eddy simulation of homogeneous incompressible, turbulent flows. *Technical Report No. TF-19, Thermosciences Division, Dept. of Mechanical Engineering, Stanford University, Stanford, California*, 1983.

[4] J. Bardina, J. H. Ferziger, and R. S. Rogallo. Effect of rotation on isotropic turbulence: computation and modeling. *J. Fluid Mech.*, 154:321–336, 1985.

[5] C. N. Baroud, B. B. Plapp, Z.-S. She, and H. L. Swinney. Anomalous self-similarity in a turbulent rapidly rotating fluid. *Phys. Rev. Lett.*, 88(11):114501–114505, March 2002.

[6] C. N. Baroud, B. B. Plapp, H. L. Swinney, and Z.-S. She. Scaling in three-dimensional and quasi-two-dimensional rotating turbulent flows. *Phys. Fluids*, 15(8):2091–2104, August 2003.

[7] P. Bartello, O. Metais, and M. Lesieur. Coherent structures in rotating three-dimensional turbulence. *J. Fluid Mech.*, 273:1–29, 1994.

[8] C. Basdevant and R. Sadourny. Modélisation des échelles virtuelles dans la simulation numérique des éecoulements turbulents bidimensionels. *J. Méc. Théor. Appl., Numéro Spéc.*, pages 243–269, 1983.

[9] F. Bellet, F. S. Godeferd, J. F. Scott, and C. Cambon. Wave turbulence in rapidly rotating flows. *J. Fluid Mech.*, 562:83–121, 2006.

[10] V. Borue and S. A. Orszag. Self-similar decay of three-dimensional homogeneous turbulence with hyperviscosity. *Physical Review E*, 51(2):R856–R859, February 1995.

[11] V. Borue and S. A. Orszag. Numerical study of three-dimensional Kolmogorov flow at high Reynolds numbers. *J. Fluid Mech.*, 306:293–323, 1996.

[12] J. Boussinesq. Théorie de l'écoulement tourbillant. *Acad. Sci. Inst. Fr., Paris*, 23:46–50, 1877.

[13] G. L. Brown and A. Roshko. On density effects and large structure in turbulent mixing layers. *J. Fluid Mech.*, 64:775–816, 1974.

[14] C. Cambon, J.-P. Benoit, L. Shao, and L. Jacquin. Stability analysis and large-eddy simulation of rotating turbulence with organized eddies. *J. Fluid Mech.*, 278:175–200, 1994.

[15] C. Cambon, N. N. Mansour, and F. S. Godeferd. Energy transfer in rotating turbulence. *J. Fluid Mech.*, 337:303–332, 1997.

[16] C. Cambon, N. N. Mansour, and K. D. Squires. Anisotropic structure of homogeneous turbulence subjected to uniform rotation. *Proceeding of the Summer Program*, pages 397–420, 1994.

[17] C. Canuto, M. Y. Hussaini, A. Quarteroni, and T. A. Zang. *Spectral methods in fluid dynamics*. Sprnger-Verlag, Berlin Heidelberg, 1988.

[18] D. Carati, S. Ghosal, and P. Moin. On the representation of backscatter in dynamic localization models. *Phys. Fluids*, 7:606–616, March 1995.

[19] F.H. Champagnea, C.A. Friehea, J.C. LaRuea, and J.C. Wynagaard. Flux measurements, flux estimation techniques, and fine-scale turbulence measurements in the unstable surface layer over land. *J. Atmos. Sci*, 34(3):515–530, March 1977.

[20] J. R. Chasnov. Similarity states of passive scalar transport in isotropic turbulence. *Phys. Fluids*, 6(2):1036–1051, February 1994.

[21] F. K. Chow and P. Moin. A further study of numerical errors in large-eddy simulations. *J. Comput. Phys.*, 184:366–380, 2003.

[22] S. G. Chumakov. Statistics of subgrid-scale stress states in homogeneous isotropic turbulence. *J. Fluid Mech.*, 562:405–414, 2006.

[23] S. G. Chumakov and C. J. Rutland. Dynamic structure models for scalar flux and dissipation in large eddy simulation. *AIAA Journal*, 42(6):1132–1139, June 2004.

[24] S. G. Chumakov and C. J. Rutland. Dynamic structure subgrid-scale models for large eddy simulation. *International Journal for Numerical Methods in Fluids*, 47:911–923, 2005.

[25] R. A. Clark, J. H. Ferziger, and W. C. Reynolds. Evaluation of subgrid-scale models using an accurately simulated turbulent flow. *J. Fluid Mech.*, 91(1):1–16, 1979.

[26] A. W. Cook. Determination of the constant coefficient in scale similarity models of turbulence. *Phys. Fluids*, 9(5):1485–1487, May 1997.

[27] L. Davidson. Large eddy simulation: a dynamic one-equation subgrid model for three-dimensional recirculating flow. *11th Int. Symp. on Turb. Shear Flow*, 3:26.1–26.6, 1997.

[28] L. Davidson. LES of recirculating flow without any homogeneous direction: a dynamic one-equation subgrid model. *2nd Int. Symposium on Turbulence Heat and Mass Transfer*, pages 481–490, 1997.

[29] L. Davidson and P. V. Nielsen. A study of low-Reynolds number effects in backward-facing step flow using large eddy simulations. *6th Int. Conf. on Air Distribution in Rooms*, 1:125–132, 1998.

[30] J. W. Deardorff. A numerical study of three-dimensional turbulent channel flow at large reynolds numbers. *J. Fluid Mech.*, 41:453–480, 1970.

[31] J. W. Deardorff. The use of subgrid transport equations in a three-dimensional model of atmospheric turbulence. *J. Fluid Eng.*, 95:429–438, 1973.

[32] J. A. Domaradzki and K. Horiuti. Similarity modeling on an expanded mesh applied to rotating turbulence. *Phys. Fluids*, 13(11):3510–3512, November 2001.

[33] J. A. Domaradzki and X. Yang. Large eddy simulations of decaying rotating turbulence. Warsaw, Poland, 15-21 August 2004. XXI ICTAM.

[34] M. Gad el hak. Fluid mechanics from the beginning to the third millennium. *Int. J. Engng Ed.*, 14(3):177–185, 1998.

[35] J. H. Ferziger. Large eddy simulation - a short course. Stanford University, November 2000.

[36] R. Friedrich and F. T. M. Nieuwstadt. LES of pipe flow. *ERCOFTAC Bulletin*, 22:19–25, 1994.

[37] W. K. George. The decay of homogeneous isotropic turbulence. *Phys. Fluids A*, 4(7):1492–1509, July 1992.

[38] M. Germano. A proposal for a redefinition of the turbulent stresses in the filtered Navier-Stokes equations. *Phys. Fluids*, 29(7):2323–2324, July 1986.

[39] M. Germano, U. Piomelli, and W. H. Cabot. A dynamic subgrid-scale eddy viscosity model. *Phys. Fluids A*, 3(7):1760–1765, July 1991.

[40] S. Ghosal, T. S. Lund, P. Moin, and K. Akselvoll. A dynamic localization model for large-eddy simulation of turbulent flows. *J. Fluid Mech.*, 286:229–255, 1995.

[41] S. Ghosal and M. M. Rogers. A numerical study of self-similarity in a turbulent plane wake using large-eddy simulation. *Phys. Fluids*, 9:1729–1739, June 1997.

[42] D. Gottlieb and S. A. Orszag. *Numerical analysis of spectral methods: theory and applications*. SIAM, 1977.

[43] H. P. Greenspan. *The theory of rotating fluids*. (Cambridge University Press, Cambridge), 1968.

[44] E. J. Hopfinger, F. K. Browand, and Y. Gagne. Turbulence and waves in a rotating tank. *J. Fluid Mech.*, 125:505–534, 1982.

[45] K. Horiuti. A proper velocity scale for modeling subgrid-scale eddy viscosities in large eddy simulation. *Phys. Fluids A*, 5(1):146–157, January 1993.

[46] K. Horiuti. A new dynamic two-parameter mixed model for large-eddy simulation. *Phys. Fluids*, 9(11):3443–3464, November 1997.

[47] K. Horiuti. *Modern simulation strategies for turbulent flow*, chapter "Rotational transformation and geometrical correlation of SGS models", pages 123–140. edited by B. J. Geurts (R. T. Edwards, Philadelphia), 2001.

[48] K. Horiuti. Transformation properties of dynamic subgrid-sale models in a frame of reference undergoing rotation. *Journal of Turbulence*, 7(16):1–27, 2006.

[49] L. Jacquin, O. Leuchter, C. Cambon, and J. Mathieu. Homogeneous turbulence in the presence of rotation. *J. Fluid Mech.*, 220:1–52, 1990.

[50] J. Jeong and F. Hussain. On the identification of a vortex. *J. Fluid Mech.*, 285:69–94, 1995.

[51] R. Jhavar and C. J. Rutland. Using large eddy simulations to study mixing effects in early injection diesel engine combustion. *SAE Tech. Papers*, (2006-01-0871), 2006.

[52] Y. Kandea and T. Ishihara. High-resolution direct numerical simulation of turbulence. *Journal of Turbulence*, 7(20), 2006.

[53] W.-W. Kim and S. Menon. A new dynamic one-equation subgrid-scale model for large eddy simulations. *AIAA-1995-356, Aerospace Sciences Meeting and Exhibit, 33rd, Reno, NV*, Jan 1995.

[54] H. Kobayashi and Y. Shimomura. The performance of dynamic subgrid-scale models in the large eddy simulation of rotating homogeneous turbulence. *Phys. Fluids*, 13(8):2350–2360, August 2001.

[55] S. Krajnović and L. Davidson. Large-eddy simulation of the flow around a surface-mounted cube using a dynamic one-equation subgrid model. *1st Symp. on Turbulence and Shear Flow Phenomena*, pages 741–746, 1999.

[56] S. Krajnović, D. Müller, and L. Davidson. Comparison of two one-equation subgrid models in recirculating flows. *Direct and Large-eddy Simulation*, III:63–74, 1999.

[57] H.-O. Kreiss and J. Oliger. Comparison of accurate methods for the integration of hyperbolic equations. *Tellus*, 24:199–215, 1972.

[58] C. Lanczos. Trigonometric interpolation of empirical and analytical function. *J. Math. Phys.*, 17:123–199, 1938.

[59] C. Lanczos. *Applied Analysis*. Prentice-Hall, 1956.

[60] A. Leonard. Energy cascade in large-eddy simulation of turbulent fluid flows. *Adv. Geophys.*, 18:237, 1974.

[61] D. K. Lilly. The representation of small-scale turbulence in numerical simulation experiments. *Proc. IBM Scientific Computing Symp. on Environmental Sciences (Yorktown Heights, N.Y.)*, page 167, 1967.

[62] D. K. Lilly. Stratified turbulence and the mesoscale variability of the atmosphere. *Journal of Atmospheric Sciences*, 40:749–761, 1983.

[63] D. K. Lilly. A proposed modification of the Germano subgrid-scale closure method. *Phys. Fluids*, 4(3):633–635, March 1992.

[64] S. Liu, C. Meneveau, and J. Katz. On the properties of similarity subgrid-scale models as deduced from measurements in a turbulent jet. *J. Fluid Mech.*, 275:83–119, 1994.

[65] S. Liu, C. Meneveau, and J. Katz. Experimental study of similarity subgrid-scale models of turbulence in the far-field of a jet. *Applied Scientific Research*, 54:177–190, 1995.

[66] H. Lu, C. J. Rutland, and L. M. Smith. A-priori tests of one-equation LES modeling of rotating turbulence. *Journal of Turbulence*, 8(37):1–27, 2007.

[67] J. L. Lumley. Toward a turbulent constitutive relation. *J. Fluid Mech.*, 41(2):413–434, 1970.

[68] J. L. Lumley. Some comments on turbulence. *Phys. Fluids A*, 4(2):203–211, February 1992.

[69] T. S. Lund, S. Ghosal, and P. Moin. *In engineering applications to large eddy simulation*, chapter "Numerical experiments with highly-variable eddy-viscosity models", pages 7–11. edited by U. Piomelli, S. Ragab (ASME, New York), 1993.

[70] N. N. Mansour, C. Cambon, and C. G. Speziale. *Theoretical and computational study of rotating isotropic turbulence*, chapter "Studies in turbulence". edited by T. B. Gatski and S. Sarkar and C. G. Speziale (Springer-Verlag, New York), 1992.

[71] O. J. McMillan, J. H. Ferziger, and R. S. Rogallo. Tests of new subgrid scale models in strained turbulence. *AIAA Paper 80-1339*, 1980.

[72] S. Menon, P.-K. Yeung, and W.-W. Kim. Effect of subgrid models on the computed interscale energy transfer in isotropic turbulence. *Computers & Fluids*, 25(2):165–180, 1996.

[73] P. Moin and K. Mahesh. Direct numerical simulation: a tool in turbulence research. *Annu. Rev. Fluid Mech.*, 30:539–578, 1998.

[74] Y. Morinishi, K. Nakabayashi, and S. Q. Ren. Dynamic of anisotropy on decaying homogeneous turbulence subjected to system rotation. *Phys. Fluids*, 13(10):2912–2922, October 2001.

[75] Y. Morinishi, K. Nakabayashi, and S. Q. Ren. A new DNS algorithm for rotating homogeneous decaying turbulence. *International Journal of Heat and Fluid Flow*, 22:30–38, 2001.

[76] C. Morize and F. Moisy. Energy decay of rotating turbulence with confinement effects. *Phys. Fluids*, 18(065107):1–9, 2005.

[77] C. Morize, F. Moisy, and M. Rabaud. Decaying grid-generated turbulence in a rotating tank. *Phys. Fluids*, 17(095105):1–11, 2005.

[78] S. A. Orszag. Numerical simulation of three-dimensional homegeneous isotropic turbulence. *Physical Review Letters*, 28(2):76–79, January 1972.

[79] M. R. Overholt and S. B. Pope. A detrministic forcing scheme for direct numerical simulations of turbulence. *Computers & Fluids*, 27(1):11–28, 1998.

[80] J. Pedlosky. *Geophysical fluid dynamics*. Springer-Verlag, New York, 1986.

[81] U. Piomelli. High reynolds number calculations using the dynamic subgrid-scale stress model. *Phys. Fluids*, 5:1484–1490, June 1993.

[82] U. Piomelli and J. Liu. Large-eddy simulation of rotating channel flows using a localized dynamic model. *Phys. Fluids*, 7(4):839–848, April 1995.

[83] U. Piomelli, P. Moin, and J. H. Ferziger. Model consistency in large eddy simulation of turbulent channel flows. *Phys. Fluids*, 31(7):1884–1891, July 1988.

[84] U. Piomelli, T. A. Zang, C. G. Speziale, and M. Y. Hussaini. On the large-eddy simulation of transitional wall-bounded flows. *Phys. Fluids A*, 2(3):257–265, February 1990.

[85] E. Pomraning. *Development of large eddy simulation turbulence models*. PhD thesis, University of Wisconsin - Madison, 2000.

[86] E. Pomraning and C. J. Rutland. Dynamic one-equation nonviscosity large-eddy simulation model. *AIAA Journal*, 40(4):689–701, April 2002.

[87] S. B. Pope. *Turbulent flows*. Cambridge University Press, Cambridge, 2000.

[88] S. B. Pope. Ten questions concerning the large-eddy simulation of turbulent flows. *New Journal of Physics*, 6(35), March 2004.

[89] J. P. Richter. *The notebooks of Leonardo da Vinci*. (Dover, New York), 1970.

[90] R. S. Rogallo. Numerical experiments in homogeneous turbulence. *NASA Technical Memorandum 81315*, 1981.

[91] R. S. Rogallo and P. Moin. Numerical simulation of turbulent flows. *Ann. Rev. Fluid Mech.*, 16:99–137, 1984.

[92] L. A. Segel. *Mathematics applied to continuum mechanics*. Macmillian, New York, 1977.

[93] Y. Shimomura. A family of dynamic subgrid-scale models consistent with asymptotic material frame indifference. *Journal of the Physical Society of Japan*, 68(8):2483–2486, August 1999.

[94] J. Smagorinsky. General circulation experiments with the primitive equations: I. the basic experiment. *Monthly Weather Review*, 91(3):99–164, 1963.

[95] L. M. Smith, J. R. Chasnov, and F. Waleffe. Crossover from two- to three-dimensional turbulence. *Physical Review Letters*, 77(12):2467–2470, September 1996.

[96] L. M. Smith and Y. Lee. On near resonances and symmetry breaking in forced rotating flows at moderate rossby number. *J. Fluid Mech.*, 535:111–142, 2005.

[97] L. M. Smith and F. Waleffe. Transfer of energy to two-dimensional large scales in forced, rotating three-dimensional turbulence. *Phys. Fluids*, 11(6):1608–1622, June 1999.

[98] L. M. Smith and F. Waleffe. Generation of slow large scales in forced rotating stratified turbulence. *J. Fluid Mech.*, 451:145–168, 2002.

[99] A. Sohankar, L. Davidson, and C. Norberg. A dynamic one-equation subgrid model for simulation of flow around a square cylinder. *Engineering Turbulence Modelling and Experiments-4*, pages 227–236, 1999.

[100] A. Sohankar, L. Davidson, and C. Norberg. Large eddy simulation of flow past a square cylinder: comparison of different subgrid scale models. *Journal of Fluids Engineering*, 122:39–47, March 2000.

[101] C. G. Speziale. Closure models for rotating two-dimensional turbulence. *Geophys. Astrophys. Fluid Dynamics*, 23:69–84, 1983.

[102] C. G. Speziale. Galilean invariance of subgrid-scale stress models in the large-eddy simulation of turbulence. *J. Fluid Mech.*, 156:55–62, 1985.

[103] C. G. Speziale. Subgrid scale stress models for the large-eddy simulation of rotating turbulent flows. *Geophys. Astrophys. Fluid Dynamics*, 33:199–222, 1985.

[104] K. D. Squires, J. R. Chasnov, N. N. Mansour, and C. Cambon. Investigation of the asymptotic state of rotating turbulence using large-eddy simulation. *Stanford Univ., Annual Research Briefs*, pages 157–170, December 1993.

[105] G. I. Taylor. Statistical theory of turbulence. *Proceedings of the Royal Society of London. Series A, Mathematical and Physical Sciences*, 151(873):421–444, 1935.

[106] B. Vreman, B. Geurts, and H. Kuerten. On the formulation of the dynamic mixed subgrid-scale model. *Phys. Fluids*, 6(12):4057–4059, December 1994.

[107] B. Vreman, B. Geurts, and H. Kuerten. Large-eddy simulation of the temporal mixing layer using the Clark model. *Theor. Comput. Fluid Dyn.*, 8:309–324, 1996.

[108] B. Vreman, B. Geurts, and H. Kuerten. Large-eddy simulation of the turbulent mixing layer. *J. Fluid Mech.*, 339:357–390, 1997.

[109] F. Waleffe. The nature of triad interactions in homogeneous turbulence. *Phys. Fluids A*, 4(2):350–363, February 1992.

[110] F. Waleffe. Inertial transfers in the helical decomposition. *Phys. Fluids A*, 5(3):677–685, March 1993.

[111] S. Yanase, C. Flores, O. Métais, and J. J. Riley. Rotating free-shear flows. i. linear stability analysis. *Phys. Fluid A*, 5:2725–2737, November 1993.

[112] X. Yang and J. A. Domaradzki. Large eddy simulations of decaying rotating turbulence. *Phys. Fluids*, 16(11):4088–4104, November 2004.

[113] P. K. Yeung and Y. Zhou. Numerical study of rotating turbulence with external forcing. *Phys. Fluids*, 10(11):2895–2909, November 1998.

[114] A. Yoshizawa and K. Horiuti. A statistically-derived subgrid-scale kinetic energy model for the large-eddy simulation of turbulent flows. *Journal of the Physical Society of Japan*, 54(8):2834–2839, August 1985.

[115] D. You and P. Moin. Large-eddy simulation of flow separation over an airfoil with synthetic jet control. *Anuual Research Briefs, Center for Turbulence Research*, pages 337–346, 2006.

[116] Y. Zang, R. L. Street, and J. R. Koseff. A dynamic mixed subgrid-scale model and its application to turbulent recirculating flows. *Phys. Fluids A*, 5(12):3186–3196, December 1993.

[117] Y. Zhou. A phenomenological treatment of rotating turbulence. *Phys. Fluids*, 7(8):2092–2094, August 1995.

[118] O. Zikanov, D. N. Slinn, and M. R. Dhanak. Large-eddy simulations of the wind-induced turbulent ekman layer. *J. Fluid Mech.*, 495:343–368, November 2003.

# APPENDIX
# The third order Runge-Kutta (RK3) with integrating factors

## Integrating Factors

Consider the PDE

$$\hat{u}_t = \hat{f}_k(\hat{u}) - \nu k^2 \hat{u} \ , \tag{A.1}$$

where $\hat{u}(\mathbf{k}, t)$ is the Fourier transform of $u(\mathbf{x}, t)$ and $\hat{f}_k(\hat{u})$ is the Fourier transform of a term nonlinear in $u(\mathbf{x}, t)$. The linear term $-\nu k^2 \hat{u}$ is in this case the Fourier transform of $\nu \nabla^2 u(\mathbf{x}, t)$. The method described below, however, can be generalized to any linear term. Equation (A.1) may be re-written as

$$(\hat{u} \ \exp(\nu k^2 t))_t = \hat{f}_k \ \exp(\nu k^2 t) \ , \tag{A.2}$$

where $\exp(\nu k^2 t)$ is an integrating factor.

Let's illustrate the integrating factor method for the explicit Euler scheme for $y_t = g(y)$

$$\frac{y^{n+1} - y^n}{\delta t} = g(y^n) = g^n(y) \ , \tag{A.3}$$

where the superscript denotes the time step. Applying this scheme to (A.2) we have

$$\frac{\hat{u}^{n+1} \ \exp(\nu k^2 (t + \delta t)) - \hat{u}^n \ \exp(\nu k^2 t)}{\delta t} = \hat{f}_k^n \ \exp(\nu k^2 t) \ . \tag{A.4}$$

Re-arranging (A.4), we write

$$\hat{u}^{n+1} = \left[ \hat{u}^n + \delta t \hat{f}_k^n \right] \ \exp(-\nu k^2 \delta t) \ . \tag{A.5}$$

Thus the nonlinear term is calculated as usual, and multiplication by the factor

$$\exp(-\nu k^2 \delta t) \ . \tag{A.6}$$

accounts for the linear term in the original equation (A.1).

### RK3 with Integrating Factors

Let's review RK3 for $dy/dt = f(y)$ and time step $h = \delta t$. We first calculate $\tilde{y}$ at $t + h/3$

$$\tilde{y} = y^n + (h/3)k_1 \ , \ k_1 = f(y^n) \ . \tag{A.7}$$

Then calculate $\hat{y}$ at $t + 2h/3$ using $f(\tilde{y})$

$$\hat{y} = y^n + (2h/3)k_2 \ , \ k_2 = f(\tilde{y}) = f(y^n + (h/3)k_1) \ . \tag{A.8}$$

Then calculate $y^{n+1}$ at $t + h$ using $(1/4)f(y^n)$ and $(3/4)f(\hat{y})$

$$y^{n+1} = y^n + (h/4)k_1 + (3h/4)k_3 \ , \ k_3 = f(\hat{y}) = f(y^n + (2h/3)k_2) \ , \tag{A.9}$$

with $k_1$ and $k_2$ as defined in (A.7) and (A.8), respectively.

Now consider the equation

$$y_t + \nu k^2 y = f(y) \ , \tag{A.10}$$

or re-written using the integrating factor $\exp(\nu k^2 t)$ as

$$(y \ \exp(\nu k^2 t))_t = f(y) \ \exp(\nu k^2 t) \ . \tag{A.11}$$

For RK3, one multiplies by $\exp(-\nu k^2 h)$, where $h$ is the multiple of $\delta t$ appropriate for each RK3 "step." We first calculate $\tilde{y}$ at $t + h/3$

$$\frac{\tilde{y} \ \exp(\nu k^2 (t + h/3)) - y^n \ \exp(\nu k^2 t)}{h/3} = f(y^n) \ \exp(\nu k^2 t) \ . \tag{A.12}$$

Solve for $\tilde{y}$ and find

$$\tilde{y} = [y^n + (h/3)f(y^n)] \exp(-\nu k^2 h/3) \ . \tag{A.13}$$

Next calculate $\hat{y}$ at $2h/3$ using $f(\tilde{y})$

$$\frac{\hat{y} \exp(\nu k^2(t + 2h/3)) - y^n \exp(\nu k^2 t)}{2h/3} = f(\tilde{y}) \exp(\nu k^2(t + h/3)) \ . \tag{A.14}$$

Solve for $\hat{y}$ and find

$$\hat{y} = y^n \exp(-\nu k^2 2h/3) + \frac{2h}{3} f(\tilde{y}) \exp(-\nu k^2 h/3) \ . \tag{A.15}$$

Finally calculate $y^{n+1}$ at $t + h$ using $(1/4)f(y^n)$ and $(3/4)f(\hat{y})$

$$\frac{y^{n+1} \exp(\nu k^2(t + h)) - y^n \exp(\nu k^2 t)}{h} = \frac{1}{4} f(y^n) \exp(\nu k^2 t) + \frac{3}{4} f(\hat{y}) \exp(\nu k^2 (t + \frac{2h}{3})) \ . \tag{A.16}$$

Solve for $y^{n+1}$ and find

$$y^{n+1} = y^n \exp(-\nu k^2 h) + \frac{h}{4} f(y^n) \exp(-\nu k^2 h) + \frac{3h}{4} f(\hat{y}) \exp(-\nu k^2 h/3) \ . \tag{A.17}$$

# APPENDIX
# Derivation of exact $\tau_{ij}$ and $k_{sgs}$ equations

The conservation law of momentum for un-filtered and filtered fields are of terms

$$\frac{\partial u_i}{\partial t} + \frac{\partial u_i u_m}{\partial x_m} = -\frac{\partial P}{\partial x_i} - 2\epsilon_{imn}\Omega_m u_n + \nu\frac{\partial^2 u_i}{\partial x_m \partial x_m} + f_i \ , \tag{B.1}$$

$$\frac{\partial \overline{u}_i}{\partial t} + \frac{\partial \overline{u}_i \overline{u}_m}{\partial x_m} = -\frac{\partial \overline{P}}{\partial x_i} - 2\epsilon_{imn}\Omega_m \overline{u}_n + \nu\frac{\partial^2 \overline{u}_i}{\partial x_m \partial x_m} - \frac{\partial \tau_{im}}{\partial x_m} + \overline{f}_i \ , \tag{B.2}$$

where the SGS stress tensor is $\tau_{ij} = \overline{u_i u_j} - \overline{u}_i \overline{u}_j$. Now we take (B.1) time with $u_j$ to obtain

$$u_j\frac{\partial u_i}{\partial t} + u_j\frac{\partial u_i u_m}{\partial x_m} = -u_j\frac{\partial P}{\partial x_i} - 2\epsilon_{imn}\Omega_m u_n u_j + \nu u_j\frac{\partial^2 u_i}{\partial x_m \partial x_m} + f_i u_j \ . \tag{B.3}$$

Change subscription of i and j to get

$$u_i\frac{\partial u_j}{\partial t} + u_i\frac{\partial u_j u_m}{\partial x_m} = -u_i\frac{\partial P}{\partial x_j} - 2\epsilon_{jmn}\Omega_m u_n u_i + \nu u_i\frac{\partial^2 u_j}{\partial x_m \partial x_m} + f_j u_i \ . \tag{B.4}$$

Add equation (B.3) and (B.4) together

$$\begin{aligned}\frac{\partial u_i u_j}{\partial t} + \frac{\partial u_i u_j u_m}{\partial x_m} &= -\left(u_i\frac{\partial P}{\partial x_j} + u_j\frac{\partial P}{\partial x_i}\right) - (2\epsilon_{imn}\Omega_m u_n u_j + 2\epsilon_{jmn}\Omega_m u_n u_i) \\ &+ \nu\frac{\partial^2 u_i u_j}{\partial x_m \partial x_m} - 2\nu\frac{\partial u_i}{\partial x_m}\frac{\partial u_j}{\partial x_m} + (f_i u_j + f_j u_i) \ .\end{aligned} \tag{B.5}$$

Similarly for the filtered momentum equation (B.2) we can get

$$\begin{aligned}\frac{\partial \overline{u}_i \overline{u}_j}{\partial t} + \frac{\partial \overline{u}_i \overline{u}_j \overline{u}_m}{\partial x_m} &= -\left(\overline{u}_i\frac{\partial \overline{P}}{\partial x_j} + \overline{u}_j\frac{\partial \overline{P}}{\partial x_i}\right) - (2\epsilon_{imn}\Omega_m \overline{u}_n \overline{u}_j + 2\epsilon_{jmn}\Omega_m \overline{u}_n \overline{u}_i) \\ &- \left(\overline{u}_j\frac{\partial \tau_{im}}{\partial x_m} + \overline{u}_i\frac{\partial \tau_{jm}}{\partial x_m}\right) \\ &+ \nu\frac{\partial^2 \overline{u}_i \overline{u}_j}{\partial x_m \partial x_m} - 2\nu\frac{\partial \overline{u}_i}{\partial x_m}\frac{\partial \overline{u}_j}{\partial x_m} + \left(\overline{f}_i \overline{u}_j + \overline{f}_j \overline{u}_i\right) \ .\end{aligned} \tag{B.6}$$

Now we subtract equation (B.6) from the filtered equation (B.5) to have the exact SGS stress tensor equation

$$\begin{aligned}
\frac{\partial \tau_{ij}}{\partial t} + \frac{\partial \tau_{ij}\overline{u}_m}{\partial x_m} &= -\left[\left(\overline{u_i \frac{\partial P}{\partial x_j}} - \overline{u}_i \frac{\partial \overline{P}}{\partial x_j}\right) + \left(\overline{u_j \frac{\partial P}{\partial x_i}} - \overline{u}_j \frac{\partial \overline{P}}{\partial x_i}\right)\right] \\
&- (2\epsilon_{imn}\Omega_m \tau_{nj} + 2\epsilon_{jmn}\Omega_m \tau_{ni}) \\
&- \frac{\partial \left(\overline{u_i u_j u_m} - \overline{u_i u_j}\ \overline{u}_m\right)}{\partial x_m} + \left(\overline{u}_j \frac{\partial \tau_{im}}{\partial x_m} + \overline{u}_i \frac{\partial \tau_{jm}}{\partial x_m}\right) \\
&+ \nu \frac{\partial^2 \tau_{ij}}{\partial x_m \partial x_m} - 2\nu \left(\overline{\frac{\partial u_i}{\partial x_m}\frac{\partial u_j}{\partial x_m}} - \frac{\partial \overline{u}_i}{\partial x_m}\frac{\partial \overline{u}_j}{\partial x_m}\right) \\
&+ \left[\left(\overline{f_i u_j} - \overline{f}_i \overline{u}_j\right) + \left(\overline{f_j u_i} - \overline{f}_j \overline{u}_i\right)\right] \ . \qquad \text{(B.7)}
\end{aligned}$$

Take the trace of equation (B.7), $k_{sgs}$ equation is of the form

$$\begin{aligned}
\frac{\partial k_{sgs}}{\partial t} + \overline{u}_j \frac{\partial k_{sgs}}{\partial x_j} &= -\left(\overline{u_i \frac{\partial P}{\partial x_i}} - \overline{u}_i \frac{\partial \overline{P}}{\partial x_i}\right) \\
&- \frac{\partial}{\partial x_j}\left(\frac{1}{2}\tau_{u_i u_i u_j} - \overline{u}_i \tau_{ij}\right) + \nu \frac{\partial^2 k_{sgs}}{\partial x_j \partial x_j} - \varepsilon \\
&- \tau_{ij}\overline{S}_{ij} + \left(\overline{f_i u_i} - \overline{f}_i \overline{u}_i\right) \ , \qquad \text{(B.8)}
\end{aligned}$$

where

$$\varepsilon = \nu \left(\overline{\frac{\partial u_i}{\partial x_j}\frac{\partial u_i}{\partial x_j}} - \frac{\partial \overline{u}_i}{\partial x_j}\frac{\partial \overline{u}_i}{\partial x_j}\right) \ , \qquad \text{(B.9)}$$

$$\tau_{u_i u_i u_j} = \overline{u_i u_i u_j} - \overline{u_i u_i}\ \overline{u}_j \ . \qquad \text{(B.10)}$$

# APPENDIX
# Derivation of the modeling of the modified cross term

Denote three different length scale filter functions as: $\begin{vmatrix} \overline{f} & \Delta_1 \\ \widehat{f} & \Delta_2 \\ \widetilde{f} & \Delta_3 \end{vmatrix}$. The exact SGS stresses are of the form

$$\tau_{ij} = \overline{u_i u_j} - \overline{u}_i \overline{u}_j \ . \tag{C.1}$$

Velocity can be decomposed by filtered and SGS velocities

$$u_i = \widehat{u}_i + u_i' \ . \tag{C.2}$$

Hence stresses are expressed as

$$\begin{aligned} \tau_{ij} &= \left(\overline{\widehat{u}_i \widehat{u}_j} - \overline{\widehat{u}}_i \overline{\widehat{u}}_j\right) + \left(\overline{\widehat{u}_i u_j'} + \overline{u_i' \widehat{u}_j} - \overline{\widehat{u}}_i \overline{u_j'} - \overline{u_i'}\, \overline{\widehat{u}}_j\right) + \left(\overline{u_i' u_j'} - \overline{u_i'}\, \overline{u_j'}\right) \\ &= L_{ij}^M + C_{ij}^M + R_{ij}^M \ , \end{aligned} \tag{C.3}$$

where

$$L_{ij}^M = \overline{\widehat{u}_i \widehat{u}_j} - \overline{\widehat{u}}_i \overline{\widehat{u}}_j \ , \tag{C.4}$$

$$C_{ij}^M = \overline{\widehat{u}_i u_j'} + \overline{u_i' \widehat{u}_j} - \overline{\widehat{u}}_i \overline{u_j'} - \overline{u_i'}\, \overline{\widehat{u}}_j \ , \tag{C.5}$$

$$R_{ij}^M = \overline{u_i' u_j'} - \overline{u_i'}\, \overline{u_j'} \ . \tag{C.6}$$

For the cross term $C_{ij}^M$, we assume

$$u_i \approx \sqrt{C_C}\widetilde{u}_i \ , \tag{C.7}$$

$$u_i' \approx \sqrt{C_C}\widetilde{u_i'} = \widetilde{u}_i - \widetilde{\widehat{u}}_i \ . \tag{C.8}$$

We can have

$$\begin{aligned} C_{ij}^{M} &= C_C \left[ \left( \overline{\widehat{\widetilde{u}}_i \widetilde{u}_j} - \overline{\widehat{\widetilde{u}}}_i \overline{\widetilde{u}}_j \right) + \left( \overline{\widetilde{u}_i \widehat{\widetilde{u}}_j} - \overline{\widetilde{u}}_i \overline{\widehat{\widetilde{u}}}_j \right) \right. \\ &- \left. \left( \overline{\widehat{\widetilde{u}}_i \widehat{\widetilde{u}}_j} - \overline{\widehat{\widetilde{u}}}_i \overline{\widehat{\widetilde{u}}}_j \right) - \left( \overline{\widehat{\widetilde{u}}_i \widehat{\widetilde{u}}_j} - \overline{\widehat{\widetilde{u}}}_i \overline{\widehat{\widetilde{u}}}_j \right) \right] . \end{aligned} \tag{C.9}$$

It can be proved analytically and numerically that $\overline{\widehat{\widetilde{f}}} = \widehat{\overline{f}}$ for homogeneous filter function. Hence the cross term is of the form

$$C_{ij}^{M} = C_C \left[ \left( \overline{\widehat{\widetilde{u}}_i \widetilde{u}_j} - \overline{\widehat{\widetilde{u}}}_i \overline{\widetilde{u}}_j \right) + \left( \overline{\widetilde{u}_i \widehat{\widetilde{u}}_j} - \overline{\widetilde{u}}_i \overline{\widehat{\widetilde{u}}}_j \right) - 2 \left( \overline{\widehat{\widetilde{u}}_i \widehat{\widetilde{u}}_j} - \overline{\widehat{\widetilde{u}}}_i \overline{\widehat{\widetilde{u}}}_j \right) \right] . \tag{C.10}$$

If $\Delta_1 = \Delta_2 = \Delta_3$, then

$$C_{ij}^{M} = C_C \left[ \left( \overline{\overline{\overline{u}}_i \overline{u}_j} - \overline{\overline{\overline{u}}}_i \overline{\overline{u}}_j \right) + \left( \overline{\overline{u}_i \overline{\overline{u}}_j} - \overline{\overline{u}}_i \overline{\overline{\overline{u}}}_j \right) - 2 \left( \overline{\overline{\overline{u}}_i \overline{\overline{u}}_j} - \overline{\overline{\overline{u}}}_i \overline{\overline{\overline{u}}}_j \right) \right] . \tag{C.11}$$